MIO

Magnetosphere-Ionosphere Observatory

Solar and Space Physics (Heliophysics) Decadal Survey

Mission Concept Study Final Report

Study Lead/POC:

Joe Borovsky
Space Science Institute

Study Engineering Support Institution(s):

The Johns Hopkins Applied Physics Laboratory
Los Alamos National Laboratory
NASA Goddard Space Flight Center
University of New Hampshire
University of Michigan
University of Calgary

Data Release, Distribution & Cost Interpretation Statements

This document is intended to support the 2024–2033 Solar and Space Physics (Heliophysics) Decadal Survey. This study was funded by the NASA Heliophysics Mission Concept Studies (HMCS) Program via award 80NSSC22K0113.

The data contained in this document may not be modified in any way.

Cost estimates described or summarized in this document were generated as part of a preliminary concept study, are model-based, assume an APL in-house build, and do not constitute a commitment on the part of APL.

Cost reserves for development and operations were included as prescribed by the NASA ground rules for the Heliophysics Mission Concept Studies program. Unadjusted estimate totals and cost reserve allocations would be revised as needed in future more-detailed studies as appropriate for the specific cost-risks for a given mission concept.

Acknowledgements

The Space Sciences Institute would like to thank all of the MIO team members, The Johns Hopkins Applied Physics Laboratory, Los Alamos National Laboratory, NASA Goddard Space Flight Center, University of New Hampshire, University of Michigan, University of Calgary, Solar and Space Physics (Heliophysics) Decadal Survey 2024–2033, and the NASA Heliophysics Division for supporting this study.

Role	Name	Affiliation
Science Team		
Leadership	Joe Borovsky, Principal Investigator	SSI
	Simon Wing, APL PI	APL
	Andy Santo, Project Management	APL
	Mike Holloway, Accelerator Lead	LANL
	Brian Gilchrist, Plasma Contactor Lead	U. Mich
	Matthew Argall, EDI & FGM Lead	UNH
	George Hospodarsky, EFW Lead	U. Iowa
	Larry Kepko, Daughter Mag & ESA Lead	GSFC
	Emma Spanswick, TREx Imager Lead	U. Calgary
Science	Bruce Carlsten	LANL
	Gian Luca Delzanno	LANL
	Eric Donovan	U. Calgary
	Christine Gabrielse	Aerospace Corp.
	Brian Gilchrist	U. Michigan
	Mike Henderson	LANL
	Bob Marshall	U. Colorado
	Jessica Matthews	U. Alaska
	Emilio Nanni	SLAC
	Vadim Roytershteyn	SSI
	Mike Ruohoniemi	Virginia Tech
	Ennio Sanchez	SRI International
	Josh Semeter	Boston U.
	Maria Usanova	U. Colorado
	Roger Varney	SRI International
	Shasha Zou	U. Michigan

Engineering Team					
Study Design Lead/MSE	Brian Bauer	APL	Thermal	Bruce Williams	APL
Systems	Grace Colonell	APL	RF Communications	Phil Huang	APL
	Larry Frank	APL	Avionics	Cristian Campo	APL
	Rob Gold	APL		Dan Rodriguez	APL
	Max Harrow	APL	FSW/Autonomy	Luis Rodriguez	APL
Mission Design	Kevin Bockelmann	APL	Propulsion	Stuart Bushman	APL
	Brent Duffy	APL		Seth Kijewski	APL
	Corinne Lippe	APL	I&T	Joe Pulkowski	APL
Cost	Kathy Kha	APL	Ground	Adam Byerly	APL
Schedule	Andy Soukup	APL		Patrick McCauley	APL
GC	Sarah Hefter	APL	Ops	Nick Pinkine	APL
	Josh Richman	APL		Dave Sepan	APL
Power	Dan Gallagher	APL	Radiation	Justin Likar	APL
Mechanical	Lisa Wu	APL		Matt Halstead	APL
Designer	Spencer Brock	APL	Harness	Jackie Perry	APL

Contents

Executive Summary 1

1. Science Investigation 2

1.1. Solar Terrestrial Probes Science Objectives 2

1.2. Mission Concept Science Objectives 2

1.3. Science Traceability 6

2. High Level Mission Concept 7

2.1. Mission Architecture 7

2.2. Orbit Environment 8

2.3. Concept Maturity 9

2.4. Technology Maturity 9

2.5. Key Trades 9

3. Technical Overview 10

3.1. Payload Description 10

3.2. Flight System Description 12

3.3. Mission Design 19

3.4. Concept of Operations 20

3.5. Ground-Based Observatories 22

3.6. Risk List 23

4. Development Schedule and Schedule Constraints 25

4.1. Science, Technology Development Plan(s) 27

4.2. Development Schedule and Constraints 27

5. Mission Life-Cycle Cost 28

5.1. Introduction 28

5.2. Mission Ground Rules and Assumptions 28

5.3. Cost Benchmarking 29

5.4. Methodology and Basis of Estimate 29

5.5. Confidence and Cost Reserves 33

5.6. De-Scope Options 34

A. Appendices 37

B. Acronym List 106

C. References 110

Executive Summary

MIO is designed to fix a cause-and-effect problem: In the nightside magnetosphere-ionosphere system we don't know what is connected to what.

The Magnetosphere-Ionosphere Observatory (MIO) mission concept is to operate a powerful 1-MeV electron accelerator on a main spacecraft in the equatorial nightside magnetosphere with the electron beam directed into the atmospheric loss cone to deposit ionizing electrons in the atmosphere sufficient to optically illuminate the magnetic footpoint of the spacecraft while 4 nearby daughter spacecraft make equatorial magnetospheric measurements. A network of ground-based imagers across Alaska and Canada will locate the optical beamspot thereby unambiguously establishing the magnetic connection between equatorial magnetospheric measurements and ionospheric phenomena. Critical gradient measurements will be made to discern magnetospheric field-aligned-current generator mechanisms. This enables the magnetospheric drivers of various aurora, ionospheric phenomena, and field-aligned currents to be determined.

The four specific science goals of MIO are to: (1) Determine to what regions in the magnetosphere the various auroral forms and the various ionospheric phenomena map. (2) Determine to where in the ionosphere magnetospheric regions, boundaries, and events map. (3) Determine what in the magnetosphere produces the various auroral forms and ionospheric phenomena. (4) Determine in what ways the magnetosphere drives field-aligned currents. The overarching objective of MIO is to unambiguously connect equatorial magnetospheric measurements to ionospheric phenomena. MIO will be a system-science facility that will support ground-based scientific campaigns and spacecraft-conjunction campaigns with the ionospheric, atmospheric, and magnetospheric communities.

MIO is a Heliophysics Mission Concept Study (HMCS) created for the next Solar and Space Physics Decadal Survey. This report provides a point design that represents a concept maturity level of 4 (CML-4), which demonstrates that MIO is technically feasible, fully addresses the science objectives and minimizes risk and cost of implementation. In summary, MIO consists of a small constellation of spacecraft in a 24-hour, low-inclination, eccentric orbit that maintains a magnetic footprint over Northern Canada and Alaska. The main spacecraft houses the electron accelerator, plasma contactor, plasma-wave instrument, electron-drift instrument, and magnetometer, while the four smaller spacecraft host electrostatic analyzers and magnetometers. The accelerator operations are focused around two years of winter and summer months. The accelerator will fire three, 0.5 second pulses (like a morse code S) at 5 minute intervals or when triggered by other sources. The 4 small spacecraft are in 200 x 400 km relative orbit about the main, allowing the constellation to measure radial and in-track gradients and to detect boundaries. Cross-links between the main spacecraft and the rest of the constellation allow for autonomous triggering of the accelerator. All other payloads will collect data at all times during nominal operations. At the end of life, all spacecraft will be disposed of by raising the orbit perigee above the GEO graveyard.

The full life cycle cost (Phases A-F; with 50% unencumbered reserves, including the launch vehicle) is $1.33 B (FY22$). The cost estimate is based on APLs extensive experience in deep space mission and includes a combination of actuals and historical data. This cost demonstrates that the MIO mission is feasible and compelling as a STP-class mission in the coming decade. A descope option (denoted MIOcore) drops the 4 daughter spacecraft and downgrades the fourth science goal: the descoped budget estimate is $999 M.

1. Science Investigation

1.1. Solar Terrestrial Probes Science Objectives

Relevant to the Solar Terrestrial Probes program objective "Understand the fundamental physical processes of the complex space … which includes the flow of energy", the MIO mission concept addresses the fundamental physical processes of current driving in any astrophysical system and of coupling in a magnetospheric system. **MIO addresses unsolved scientific questions about the physics of energy flow and cause and effect within the interconnected magnetosphere-ionosphere system.** MIO focuses on the "weakest link" in our understanding of the coupled system, which is the fact that **we don't know what couples to what!** The MIO mission will conclusively fix that key knowledge gap throughout the complex nightside magnetosphere-ionosphere system.

1.2. Mission Concept Science Objectives

The MIO mission is designed to conclusively fix a major gap in our knowledge of system-level dynamics: the gap that in the multiply-connected magnetosphere-ionosphere system **we don't know what is connected to what**. Specifically, we don't know what fundamental magnetospheric processes drive the diverse ionospheric and auroral phenomena and we don't know what form of energy is extracted from the nightside magnetosphere and transferred to the ionosphere and atmosphere. This knowledge gap underlies the decades-old question of how the magnetosphere drives aurora and underlies the more-modern problems of how the magnetosphere drives other ionospheric phenomena such as SAPS/SAID, STEVE, and ionospheric density irregularities. MIO will decisively fix this gap by unambiguously connecting the magnetosphere and its physical processes to the ionosphere and its diverse phenomena. MIO uses a powerful beam from a relativistic-electron accelerator in the magnetosphere to establish the magnetic connection between magnetospheric spacecraft measurements and locations in the ionosphere and atmosphere (cf. Figure 1). By making the unambiguous M-I connection MIO will be able to finally elucidate the main

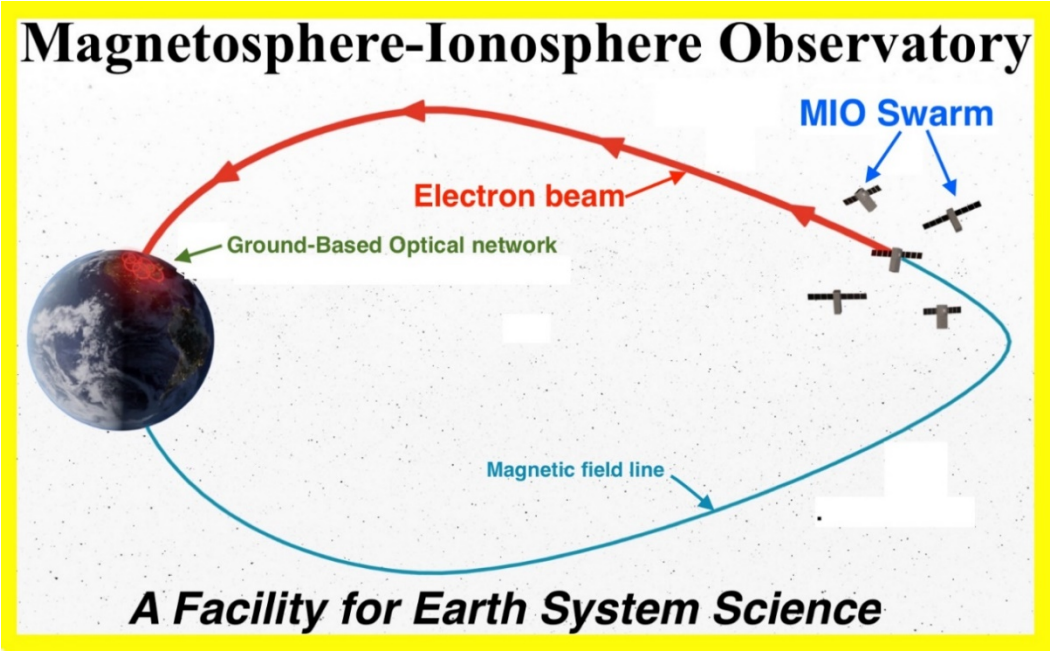

Figure 1-1 A depiction of the MIO mission configuration, which includes a main spacecraft operating a relativistic-electron accelerator, 4 nearby daughter spacecraft making gradient measurements, and a ground-based optical network covering Canada and Alaska.

drivers of major space-weather phenomena (e.g. scintillation from ionospheric density irregularities) and establish a fundamental link to elucidate how energy flows between the magnetosphere and the ionosphere. MIO is the result of substantial technology development and will provide the magnetospheric, ionospheric, and atmospheric communities with a unique scientific facility.

The MIO mission concept (Figures 1-1 and 1-2) is to operate a powerful relativistic-electron accelerator (beam energy 1 MeV, beam power 1 kW) on a main spacecraft in the equatorial nightside magnetosphere with the beam directed into the atmospheric loss cone to deposit ionizing electrons in the atmosphere sufficient to optically illuminate the magnetic footpoint of the main spacecraft, while 4 nearby daughter spacecraft make magnetospheric measurements. The optical beamspot in the atmosphere is located using a network of ground-based imagers that covers Canada and Alaska. MIO thereby unambiguously establishes the connection between magnetospheric measurements and ionospheric phenomena. Critical magnetospheric measurements will be made to discern magnetospheric regions, boundaries, and generator mechanisms. This enables the magnetospheric drivers of various aurora, ionospheric phenomena, and field-aligned currents to be determined.

On the non-spinning main spacecraft it is essential to accurately know the direction of the local magnetic field to be able to point the accelerator beam into the atmospheric loss cone. Non-spinning spacecraft can suffer from magnetometer offsets preventing the magnetometer from accurately determining the magnetic-field direction. The electron drift instrumnt (EDI) instrument on the main spacecraft overcomes this problem by accurately determining the direction of the local magnetic field, enabling magnetometer offsets to be corrected. Also on the main spacecraft it is essential to operate a plasma contactor to prevent uncontrolled spacecraft charging during accelerator-beam operations (cf. Appendix A.1.1). To be successful MIO must make measurements in the magnetosphere to identify magnetospheric regions (e.g. electron plasma sheet, ion plasma sheet, remnant layer, plasmasphere, lobes), magnetospheric boundaries (e.g. plasmapause, inner edge of electron plasma sheet, plasma sheet boundary layer), and magnetospheric phenomena (e.g. velocity shears, plasma waves, ULF waves, substorm particle injections). These measurements are made with ESAs, magnetometers, EDI, and Waves instrumentation. For auroral physics, measuring the magnetospheric electric field is essential: EDI makes that measurement. In the full MIO concept the ESAs are on the four daughter spacecraft: in the descope option (MIOcore) two ESAs are mounted on the main spacecraft and there are no daughters. To make clear identifications of the magnetospheric generator mechanisms driving field-aligned currents (including auroral field-aligned currents) the four daughter spacecraft measure critical gradients in the magnetosphere: gradients in n, T_i, T_e, P_i, P_e, $\underline{\mathbf{v}}$, and $\mathbf{\underline{B}}$ so that the various terms in the current-generator equation (cf. eq. (1) of Borovsky et al. [2020a])

$$(1/L_{||})\,(j_{||}/B) = (2/B^3)\,((\nabla P_i + \nabla P_e) \times \nabla B)_{||} + (2\rho/B^3)\,((d\underline{v}/dt) \times \nabla B)_{||} - (1/B^2)\,((d\underline{v}/dt) \times \nabla \rho)_{||} + (\rho/B^3)\,\underline{\omega} \bullet d\underline{B}/dt + (\omega_{||}/eB^3)\,(\nabla k_B T \times \nabla \rho)_{||} + (\rho/B^2)\,d\omega_{||}/dt$$

can be evaluated. Here $j_{||}$ is the field-aligned current density, $\underline{\omega} = \nabla \times \underline{v}$ is the vorticity, and the $||$ subscript means parallel to the local magnetic field. Each term in the equation involves one gradient crossed into another gradient: hence the 4 daughter spacecraft are designed to simultaneously measure radial gradients and azimuthal (in track) gradients in the magnetosphere. In the descope option, the various gradients can be identified but not well quantified. Another current-generation mechanism involves Hall currents: to detect and quantify Hall currents the ion and electron cross-

field velocities must be separately measured. To do this the ESAs measure the ion velocity and the EDI measures the electron velocity.

Community use is possible via (1) conjunctions with low-altitude spacecraft, (2) collaboration with global ionospheric radars, (3) conjunctions with ISR radars and ionospheric heaters, and (4) ground-based ionospheric and atmospheric instrumentation fielded along the footpoint path (cf. Figure 2). Via scientific campaigns with the magnetospheric, ionospheric, and atmospheric communities MIO will serve as a meta-instrument for Earth System Science [*Borovsky and Valdivia,* 2018].

Figure 1-2: An estimate of the 24-hr magnetic-footpoint track (gray) of the MIO swarm in its 4.3x9 RE 24-hr orbit at a magnetospheric-activity level of Kp =2. The large red circles are the fields of view of the present-day TREx camera network (which will be expanded) and the smaller red circles are the operating ranges of the PFISR and HAARP ionospheric facilities. The tickmarks on the gray track are 1

The overarching science goal of the MIO mission is to **Determine the magnetospheric processes that drive multiple types of aurora, multiple ionospheric phenomena, and field-aligned currents and to determine the multiple unknown connections in the magnetosphere-ionosphere system**.

The overarching objective of MIO is to **Unambiguously connect magnetospheric measurements to ionospheric phenomena**. This is accomplished with the mission objective to **Regularly connect magnetospheric measurements to an observed beamspot in the ionosphere-atmosphere.** Specific objectives are to make the connected measurements to:

1. Determine to what regions in the magnetosphere the various auroral forms and the various ionospheric phenomena map.
2. Determine to where in the ionosphere magnetospheric regions, boundaries, and events map.
3. Determine what in the magnetosphere produces the various auroral forms and ionospheric phenomena.
4. Determine in what ways the magnetosphere drives field-aligned currents.

The MIO mission will determine what forms of energy are converted in the magnetosphere to drive ionospheric phenomena, enabling us to better understand the impact on the magnetosphere of its driving of the ionosphere. Tests of the diverse theories of auroral generators can finally be made. And the MIO mission will test M-I-coupling ideas about where the magnetosphere is driving ionospheric convection versus where the ionosphere is driving magnetospheric convection. Suspected connections between the ionosphere and the magnetosphere can be definitely confirmed or refuted.

The MIO mission will achieve all four of the above specific mission objectives. A descope option (MIOcore) without the 4 daughter spacecraft will fully achieve the first three objectives and will partially achieve Objective 4.

In the next decades of magnetosphere-ionosphere system science we (1) want to understand the behavior of the driven system, (2) want to understand the physical processes acting throughout

the system, and (3) want to know what solar wind is coming and predict what will happen. The MIO mission will directly help with (1) and (2).

More detailed information about the MIO mission concept can be found in Appendix A and in *Borovsky et al.* [2020a,b]. The Topics of Appendix A appear in the following table.

Appendix	Title
A.1	**MIO Beam Operations**
A.1.1	Safety of MIO Operations
A.1.2	Pitch-Angle Scattering of the MIO Beam Electrons by Ambient Magnetospheric Plasma Waves
A.1.3	Beam-Stability Calculations
A.1.4	Evolution of the MIO Linac Pulsed Beam: Filling-in Distance, Beam Angular Spread, and Beam Radius
A.1.5	Optical Beamspot Detection
A.1.6	Clouds and Camera-Viewing Statistics
A.2	**Accelerator Maturation**
A.2.1	Strategy for Increasing Accelerator TRL
A.2.2	Accelerator Trades
A.2.3	Missions that MIO Can Leverage for Design Maturation
A.3	**Mission Design**
A.3.1	Mission Design Table
A.3.2	The Loss-Cone Shift and Its Impact on Orbit Selection
A.3.3	Launch/Insertion
A.3.4	Mother Orbit Maintenance
A.3.5	Daughter Formation Design and Maintenance
A.3.6	Disposal
A.4	**Space Environmental Effects Overview**
A.5	**Payload Summary Tables**
A.5.1	Accelerator Summary Table
A.5.2	Plasma Contactor Summary Table
A.5.3	Electron Drift Instrument Summary Table
A.5.4	Flux-Gate Magnetometer Summary Table
A.5.5	Waves Summary Table
A.5.6	Magnetometer (Daughter) Summary Table
A.5.7	Electrostatic Analyzer (ESA) Summary Table
A.6	**Flight System Summary Tables**
A.6.1	Mothership
A.6.2	Daughtership
A.6.3	Launch
A.7	**Integration and Test**
A.8	**Mission Operations Summary Table**

.

1.3. Science Traceability

MIO is a 5-spacecraft mission with a main spacecraft carrying an electron accelerator and scientific instrumentation plus 4 instrumented daughter spacecraft: MIOcore is a descope option without the 4 daughter spacecraft.

Question	Science Requirement	Electron Beam	Magnetospheric Measurements	Instruments	Functional Requirement
1. [T] To where in the magnetosphere do various auroral forms and various ionospheric phenomena map?	• Locate the accelerator electron-beam spot in the atmosphere. • Determine the plasma properties in the magnetosphere.	• [T] 1-kW 1-MeV beam • [T] TREx imagers • [T] Plasma Contactor • [T] Mag • [T] EDI	• [T] Density 0.1-100 cm^{-3}, 10% accuracy • [T] T_i,T_e 100 eV - 10 keV: 10% accuracy • [T] v_i 10 - 1000 km/s: 10% accuracy • [T] B 5 - 200 nT, 1% accuracy • [T] Waves: presence of chorus, EMIC	• [T] ESA • [T] Mag • [T] Waves	• [T] 4.3x9 R_E orbit with apogee over Canada. • [T] Dark and clear skies over TREx imagers • [O] MIO or [T] MIOcore • [T] Accelerator aimed within 0.5° of B-field line
2. [T] To where in the ionosphere do magnetospheric regions, boundaries, and events map?	• Locate the accelerator electron-beam spot in the atmosphere. • Determine the plasma properties in the magnetosphere.	• [T] 1-kW 1-MeV beam • [T] TREx imagers • [T] Plasma Contactor • [T] Mag • [T] EDI	• [T] Density 0.1-100 cm^{-3}, 10% accuracy • [T] T_i,T_e 100 eV - 10 keV: 10% accuracy • [T] v_i 10 - 1000 km/s: 10% accuracy • [T] B 5 - 200 nT, 1% accuracy • [T] Waves: presence of chorus, EMIC	• [T] ESA • [T] Mag • [T] Waves	• [T] 4.3x9 R_E orbit with apogee over Canada. • [T] Dark and clear skies over TREx imagers • [O] MIO or [T] MIOcore • [T] Accelerator aimed within 0.5° of B-field line
3. [T] What in the magnetosphere produces the various auroral forms and various ionospheric phenomena?	• Locate the accelerator electron-beam spot in the atmosphere. • Determine the plasma properties in the magnetosphere.	• [T] 1-kW 1-MeV beam • [T] TREx imagers • [T] Plasma Contactor • [T] Mag • [T] EDI	• [T] Density 0.1-100 cm^{-3}, 10% accuracy • [T] T_i,T_e 100 eV - 10 keV: 10% accuracy • [T] v_i 10 - 1000 km/s: 10% accuracy • [T] B 5 - 200 nT, 1% accuracy • [T] Waves: presence of chorus, EMIC	• [T] ESA • [T] Mag • [T] EDI • [T] Waves	• [T] 4.3x9 R_E orbit with apogee over Canada. • [T] Dark and clear skies over TREx imagers • [O] MIO or [T] MIOcore • [T] Accelerator aimed within 0.5° of B-field line
4. [O] In what ways does the magnetosphere drive field-aligned currents?	• Evaluate in the magnetosphere the gradient terms of the current-generation equation and measure the Hall current at all local times.	none	• [T] Density 0.1-100 cm^{-3}, 10% accuracy • [T] T_i,T_e 100 eV - 10 keV: 10% accuracy • [T] v_i 10 - 1000 km/s: 10% accuracy • [O] v_e 10 - 1000 km/s: 10% accuracy • [T] B 5 - 200 nT, 1% accuracy	• [O] ESA • [T] EDI • [O] Mag	• [T] 4.3x9 R_E orbit • [O] MIO with daughters carrying ESAs and Mags • [O] Daughters 200-400 km away from mother in R, I directions

2. High Level Mission Concept

In support of the Solar and Space Physics (Heliophysics) 2022 Decadal Survey, the PI led an experienced team of engineers and scientists at The Johns Hopkins University Applied Physics Laboratory (APL) that have developed a mission concept that implements the science objectives discussed in Section 1. The mission concept presented here is the result of trade studies that optimized the mission with regard to factors such as science objectives, concept study requirements, space environment and engineering constraints, and risk. Section 2 of this concept study report presents an overview of the MIO concept; detailed information on the flight system is given in Section 3. Appendices to the MIO concept study report provide additional details on accelerator operations and ground observations, concept maturation, mission design, environmental impacts, spacecraft design, payload, and ground system. The appendices also describe how critical technical challenges discussed in the prior Heliophysics Decadal Survey have been overcome.

2.1. Mission Architecture

The concept study was developed using APL's concurrent engineering laboratory, which fosters real-time interaction between scientists, instrument developers, and flight system engineers. This interaction allows the team to focus quickly on trades and critical factors in the design to arrive at a concept representing a mission point design at Concept Maturity Level (CML) 4, understand trades and development to be conducted in subsequent mission phases, and identification of mission-level risks and mitigations. The result of this process is a well-defined, feasible mission that accomplishes science goals at reasonable cost and with low schedule risk. We therefore recommend MIO as the best concept for exploring the interaction between the Earth's Magnetosphere and Ionosphere. Mission and spacecraft design features of the MIO mission concept include:

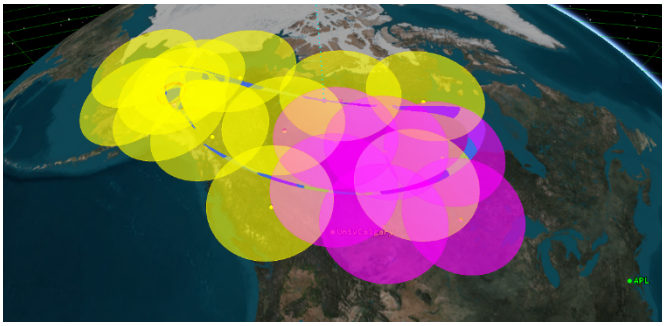

Figure 2-1 MIO Magnetic Ground Track with TREx network in Pink, THEMIS sites in Yellow, and PFISR & HAARP in Red.

- A mother spacecraft with four daughters in a 4.3 x 9 Re, 24-hour orbit with inclination < 5° (2° was chosen for the study in order to avoid conflict with the GEO belt). Daughters are equally spaced around the mother in a 200 x 400 km relative orbit.
    - Launch C3 ≤ 0 km^2/s^2 for a launch from the Cape that include inclination change and apogee insertion. The mother will then perform the 886 m/s perigee raise maneuver before releasing the daughters.
    - All spacecraft will perform a 242 m/s disposal maneuver to raise the orbit perigee above the GEO graveyard.
- Nominal Operations: Payloads onboard Mother and Daughters on and collecting data. Mother is oriented so that arrays are on the sun and the EFW booms/EDI are normal to the local magnetic field line.
- Accelerator Operations: Accelerator is firing three, 0.5 second pulses spaced 0.5 seconds apart (like a Morse code S) spaced every 5 minutes. TREx, THEMIS, PFSIR, or HAARP ground sensors observe the pulses as they interact with the Earth's upper atmosphere. Additional

pulses may be triggered via boundary crossing detection onboard the spacecraft or by ground operator command.
    - Daughters are relaying mag and ESA data to the mother every 12 seconds for boundary detection.
    - Accelerator operations only take place when it is night at the magnetic ground point and interference (moon, aurora, clouds) is minimal.
- Mother is a 1660 kg wet mass, 3-Axis spacecraft with 779 kg dry mass, 183 kg payload, 6.2 m^2 solar arrays and 1334 m/s pressurized monopropellant propulsion.
- Daughters are 87 kg wet mass, 5 RPM spinning spacecraft with 70 kg dry mass, 5.3 kg payloads, and 330 m/s blowdown monopropellant propulsion.
    - The daughters are very similar to the spacecraft of the Goddard MagCon mission.
- S-band uplink, downlink, and crosslinks to provide 2,250 Gbits of total mission science data return and allow mother to autonomously detect boundary crossings.
- Mission Operations Center/Science Operation Center ground systems to perform all functions needs to operate the mission, coordinate operations with the ground sensors, return data through the NEN, distribute science and engineering data to the science teams, and analyze and archive mission data.
- Small, dedicated antenna at the University of Calgary for operator-commanded pulsing and enabling/disabling accelerator operations if terrestrial weather changes.

2.2. Orbit Environment

The operating orbit for this mission (4.3 x 9 Re) results in the spacecraft dropping into the middle of the outer radiation belt each orbit. As a result, internal charging and radiation dosage are larger drivers for this mission than most. The MIO mission, like Van Allen Probes, needs to be designed to handle the internal charging "bleed off" as the flux varies by almost three orders of magnitude between perigee and apogee. The MIO system should be designed to survive transient "Peak" flux / fluence exposures of up to 10 hours each orbit with the remaining 14 hours under "Quiet" flux exposure. Radiation doses at EEE device locations (~100 mil Eq. Al) will be ~ 89 krad(Si)/yr with surface doses as high as 1 Grad/yr. For the 2-year mission, the resulting TID requirement is 355 krad(Si) @ 100 mil Eq. Al. Appendix A.4 provides more detail into the operating environment and recommendations for mitigating environmental effects.

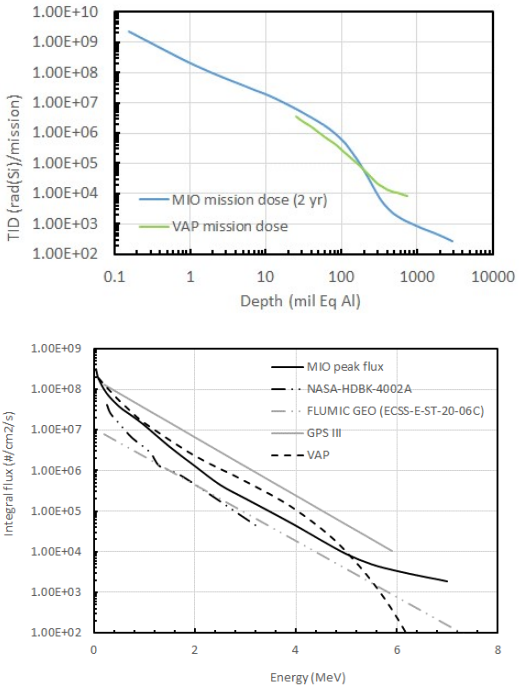

Figure 2-2: TID and Integral Flux for the MIO orbit with comparisons to similar missions. TID is comparable to VAP until shielding exceeds 200 mil Eq. Al. where MIO's relative dose trends down by an order of magnitude.

Predicted mission dose levels can be satisfied by a combination of shielding and prudent EEEE part selection for both the flight systems and payloads. Spacecraft charging will be a challenge when the accelerator and Plasma Contactor System (PCS) are operating as well as during nominal data collection. A combination of design and verification approaches based on the Van Allen Probes and tailored Clipper processes are recommended to mitigate the radiation and charging challenges. Solar arrays should include features such as grounded ITO, grout, current limiting diodes, etc. Accelerator verification (TRL maturation) should include TID

/ TNID effects (on EEEE parts) and consider external and internal charging effects caused by both the accelerator firing as well as the operating environment. System level / end-to-end charging verification (ground test) of operating accelerator and PCS is highly recommended. Cheminax (0026S1664) was baselined for the harness with additional shielding for external harnessing. For harnesses inside the bus, 50 mil Eq. Al shielding along with 7 mil Eq Al MLI is sufficient to reduce accumulated fields below common discharge thresholds (< 1.0e7 V/m); however, single layer black Kapton or Neptape is recommended.

2.3. Concept Maturity

The study was conducted at CML 4. (point design to subsystem-level mass, power, performance, cost, risk) The outcome of the study was the evaluation of the trade space and the development of a point design that achieves the mission goals. Where the information needed for CML 5 (initial concept implementation) was available, the information is included in the trade space, point design, and this study report.

2.4. Technology Maturity

The team included Technology Readiness Levels (TRLs) for spacecraft subsystem elements and instruments in the development of the MIO concept. All components of the spacecraft included in the design are at TRL 6 or higher. Where possible, the instruments included in the payload for the study are based on previously flown instruments that would allow the mission to be flown now without technology development. The only exception is the accelerator, which is currently TRL 4 and needs work to advance the technology readiness prior to PDR. Instrument and subsystem TRL assessments are included in the detailed flight systems discussion in Section 3.

2.5. Key Trades

The study team assessed options for all major design decisions and selected the best approach for the mission concept. Trades were performed based on a combination of mission performance requirements and engineering judgement of the technical benefit, cost, schedule, and risk trade-offs.

Table 2-1: A list of trade studies (1-9, green shading) and studies (10-16, red shading) performed for this MIO Heliospheric Mission Concept Study.

	Study	Location in Report
1	Orbit perigee, apogee, and inclination	Appendix A.3.2
2	Denser network of ground-based imagers	A.1.5
3	3 versus 4 daughters for gradients	3.2
4	Accelerator beam voltage versus current	A.2.2
5	Launch and deployment (direct inject, EP spin-out, launch to apogee, bi-elliptic transfer)	3.2.1, A.3.3, A.6.1, A.6.1.1
6	Communications architecture (primary daughter-mother interface)	A.6.1.8
7	Mothership power architecture (28 vs 100 V bus)	3.2.1, A.6.1.3
8	Accelerator operations	3.4.2, 3.4.3
9	Disposal strategy	A.3.6
10	Fail-safe accelerator operations plan	A.1.1
11	Developing an algorithm for non-dipole aiming of accelerator	Avoided with orbit choice A.3.2
12	Developing automated schemes for deciding on beam firings	3.4.2, 3.4.3
13	Assess impact of imager cloud cover	A.1.6
14	Update beam-stability calculations	A.1.3
15	Assess impact of plasma-wave scattering	A.1.2
16	Program of accelerator TRL maturation	A.2.1

3. Technical Overview

3.1. Payload Description

The MIO payload design comprises five instruments accommodated on the mother spacecraft and two on each daughter. Most instruments are based on a high-heritage representative sensor from a previous mission such as Cluster, MAVEN, and Van Allen Probes. Table 3-1 gives the MIO payload mass and power table.

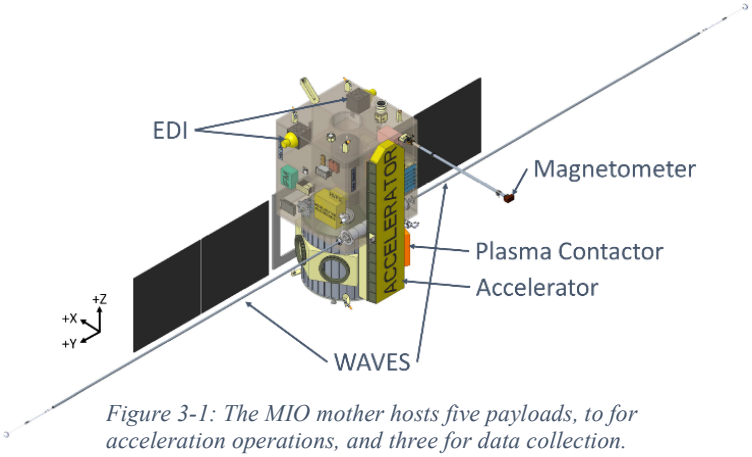

Figure 3-1: The MIO mother hosts five payloads, to for acceleration operations, and three for data collection.

Table 3-1: Payload resource summary table

	Mass				Average Power		
	#	CBE (kg)	% Cont.	MEV (kg)	CBE (W)	% Cont.	MEV (W)
Electron Accelerator	1	139.4	15%	160.3	225*	10%	248*
Plasma Contactor	1	23.0	15%	26.5	248*	10%	273*
Electron Drift Instrument (EDI)	1	12.2	15%	14.0	10.2	15%	11.7
Fluxgate Magnetometer (FGM)	1	3	15%	3.4	2.5	15%	2.9
Electric Field Waves (EFW)	1	3.6	15%	4.1	2.7	15%	3.1
Total Payload Mass (Mother)		181.1	15%	208.3	488.4	10%	538.7
Magnetometer	1	1.1	15%	1.3	2.9	15%	3.3
Electrostatic Analyzer (ESA)	1	4.1	15%	4.8	3.6	15%	4.2
Total Payload Mass (Daughter)		5.2	15%	6.1	6.5	15%	7.5

* Average power during accelerator operations (50% duty cycle max).

3.1.1. Electron Accelerator

A team of Los Alamos and SLAC accelerator scientists and engineers (led by Bruce Carlsten) has developed a novel accelerator technology that enables the MIO mission [*Lewellen et al.*, 2019]. This technology The Los Alamos/SLAC accelerator concept is composed of three units: the accelerator, control electronics, and high-voltage power supply (HVPS).

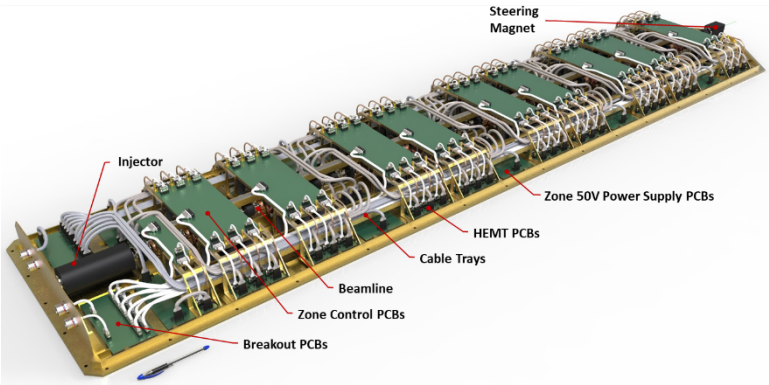

Figure 3-2: The accelerator has an electron beam injector with 9 amplification zones, four focus modules, and a beam steering magnet (pen shown for scale).

The accelerator, further described in Appendix A.2, is based on driving 5.1-GHz (C-band) radio-frequency (RF) cavities with high-electron mobility transistor (HEMT) high-power, solid-state amplifiers. These gallium nitride (GaN) HEMT amplifiers are capable of generating up to 500 W (peak) of RF power at C-band with about 50% efficiency, and operate at voltages as low as 50-V DC. These HEMTs can operate up to 10% duty cycle, for an average power of up to 50 W. The control electronics box houses the control processor/FPGA, digital and state of health electronics, and low-voltage power supplies. The HVPS is available is available as a COTS unit with flight heritage (3000+ devices on orbit).

3.1.2. Plasma Contactor

The Plasma Contactor generates a plasma cloud that offsets the charging impact of firing the accelerator. Plasma contactors have flown on the NASA Polar [Comfort et al., 1998], ESA Cluster [Torkar et al., 2001], and NASA MMS [Torkar et al., 2016] missions. This payload is essentially an EP propulsion system without the hardware to focus and accelerate the plasma into a thruster. The plasma contactor is composed of three contactors (cathode, anode, keeper, and heater assemblies), a Xenon tank, valves, regulators, flow controllers, power supplies, radiators, and controller. Two contactors will be activated any time the accelerator fires with a redundant contactor available to meet mission lifetime needs. The plasma contactor is mounted to the bottom of the spacecraft so that the plasma is released in the opposite direction as the accelerator electron beam.

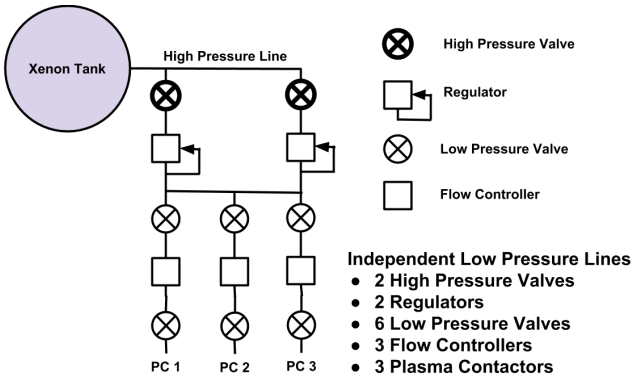

Figure 3-3: The plasma contactor schematic shows that it is an EP system.

3.1.3. Electron Drift Instrument

The Electron Drift Instrument (EDI) measures the direction of the magnetic field line to a high level of accuracy. To do that, the instrument fires a pair of electron beams in opposite directions, normal to the magnetic field line. The electron beams curl around the magnetic field line and are detected via a pair of detectors on the opposite sides of the spacecraft (co-located with the other beam generator). The direction of the returning beams defines the plane normal to the local magnetic field. The EDI is comprised a pair of Gun-Detector Units (GDUs) and a Gun Detector Electronics box. The EDI has successfully flown on Cluster and MMS, but some additional shielding will be needed to mitigate the MIO radiation environment. EDI also measures the magnetospheric electric field and the electron drift velocity.

3.1.4. Fluxgate Magnetometer

The Fluxgate Magnetometer (FGM) instrument measures the three-dimensional DC magnetic field. The FGM instrument in the notional MIO payload is based on the MAG instrument flown on the MESSENGER mission to Mercury (Anderson et al., 2007). For MIO, the FGM sensor will be mounted on a single 2-m-long boom in a configuration designed to maintain alignment with the EDI sensor.

3.1.5. Electric Field Waves

The Electric Field Waves (EFW) instrument measures the three-dimensional AC electric field to help assess the wave dynamics and loss processes at play in the Jovian magnetosphere. The EFW instrument in the notional MIO payload is based on the LPW instrument flying currently on the MAVEN and Juno missions.

3.1.6. Magnetometer (Daughter)

The daughtership magnetometer and boom are the GTOSat design with a similar magnetometer to MAVEN, Juno, PSP, and VAP.

3.1.7. Electrostatic Analyzer (Daughter)

The Electrostatic Analyzer (ESA) on the daughterships is baselined as the ESA flown on the THEMIS mission [*McFadden et al.*, 2008]. If the daughters are descoped from MIO, a pair of these instruments will be added to the mother.

3.2. Flight System Description

The MIO flight system consists of one mothership with four daughters. The daughter spacecraft can be dropped in a descope option with reduced science return. All spacecraft must be capable of communication with Earth, maneuvers, payload support, and power generation/distribution. During nominal operations, all data collected by the daughters will be relayed to the mother for downlink. The spacecraft are largely single-string with select redundancy based on the operating environment. If one of the four daughters fails, the science impact is minimal: in that case the three surviving daughters will adjust their formation in order to maintain radial and in-track gradient measurements.

3.2.1. Mothership

The mothership is a 3-Axis stabilized, single-string spacecraft with maximum dry mass of 849 kg. The spacecraft bus is roughly 1.25 m across and 2.5 m high, with two deployable arrays and mounting/deployment interfaces for the four daughters, as shown in Figure 3-4. The lower structure contains the launch vehicle interface, propulsion tank, plasma contactor, and daughter interfaces, while instruments and spacecraft electronics are mounted in the upper structure. Due to its size (about the size of a surfboard), the accelerator runs the full length of the spacecraft. The details of the spacecraft are summarized in this section with design summaries, block diagrams, and technical budgets available in Appendix A.6.

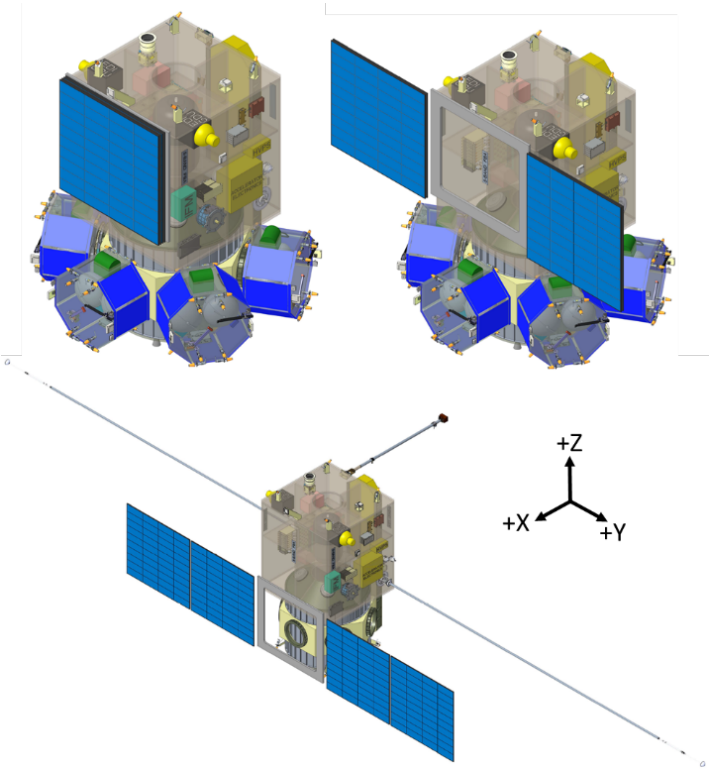

Figure 3-5: Mothership flight system shown in the fully stowed (top-right), partially deployed (top-left), and fully deployed (bottom) configurations.

During daylight operations, the spacecraft will be oriented so that the arrays (+ X) are directly pointed towards the sun and the local magnetic field runs perpendicular to the line between the EDI GDUs (Y–axis) as well as perpendicular to the EFW booms (also Y-axis). Another way to stating this is that the local magnetic field needs to be parallel to the X-Z plane of the spacecraft. Since the bus is free to rotate around the Y-axis, these two pointing constraints can be met without gimbaling. Since the radiator for the accelerator is on the –X face of the spacecraft, the radiator will be partially warmed by the Earth, saving power on survival heaters while the accelerator is not operating.

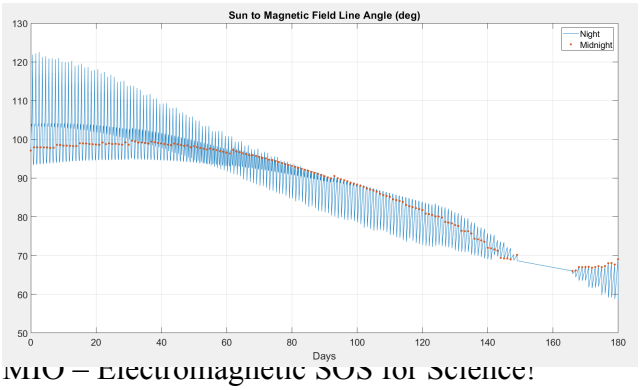

During accelerator operations, the accelerator (+ Z) needs to be aimed along the magnetic field line. The spacecraft is still free to rotate around the Z-axis, but it is no longer possible to keep the arrays pointed directly at the sun without gimbaling the arrays. The magnitude of this offset ranges from 0 degrees at local dawn/dusk to a worst-case offset at local midnight that trends from + 10 degrees near the winter solstice to -25 degrees near the summer solstice at local midnight. Since this offset is less than 10 degrees for most of the year and never exceeds 30 degrees, the reference design in this write-up opted to go with a fixed array. This design approach results in larger arrays, but provides a simplified mechanism for the partial/full deployment of early operations and reduced interference in the EDI and EFW instruments.

Figure 3-6: Angle between the sun vector and local magnetic field line. The red dots show the worst-case offset at midnight each night.

3.2.1.1. Configuration/Mechanical

The core structure for the notional design is essentially the IMAP structure with the DART structure stacked on top of it. This approach provides a lower, cylindrical structure that is focused on housing the propellant tank and Daughtership launch interfaces while the upper structure provides plenty of mounting surfaces for the electronics boxes and instruments. This approach also provides an elongated structure that fits the length of the accelerator.

Mechanisms onboard the spacecraft include: solar array storage/deployment, one magnetometer boom, two waves stacers, and four daughtership separation systems. The solar array folds up on the upper half of the +X face for launch and is partially deployed post-separation. At this stage, the two wings fold out in the ±Y with one panel on each wing facing in the +X direction and the other panel facing in the –X direction. After orbit insertion and daughtership separation, the array is fully deployed by flipping the "yoke" down over the lower half of the +X face (which previously housed the daughters) and fully unfolding each wing so that all panels are facing in the +X direction. Moving the array to the lower half of the bus reduces the impact the array has on EDI and EFW operations. The magnetometer boom is a two-meter boom that folds up alongside the accelerator for launch. Due to the length of the accelerator, the boom only needs a single hinge. The stacers are stowed within the bus and are deployed axially in the ±Y direction. The reference design draws heritage from MAVEN, but other missions (like STEREO) have flown similar designs. Finally, the daughtership interface was sized based on the Lightband from Planetary Systems Corporation.

The reference configuration is primarily driven by the launch/insertion strategy and payload suite. For example, if the launch vehicle is capable of directly injecting the spacecraft into the mission orbit, ~75% of the delta-V is no longer needed and the daughters can launch via an ESPA ring instead of being carried by the mother for the first 3 days of the mission. In addition, the solar array deployment is simplified.

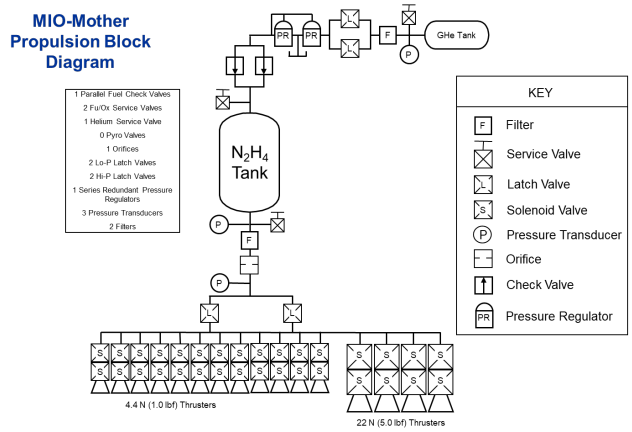

Figure 3-7: Notional schematic for MIO Mother Propulsion subsystem.

3.2.1.2. Propulsion

The reference design is a pressurized, monoprop, hydrazine design with eight, 4.4 N (1 lbf) thrusters for attitude control and momentum dumping and four, 22 N (5 lbf) thrusters facing in the –Z direction for delta-V. An ATK 80507-3 PMD tank has been selected as the propellant tank with a smaller, pressurant tank mounted above it. This system has excess capacity beyond the propellant needs of the mission (with margin). All components are COTS with flight heritage.

3.2.1.3. *Electrical Power*

The Electrical Power Subsystem design is driven by the power needs of the accelerator and, to a lesser extent, plasma contactor. The reference architecture is a Direct Energy Transfer (DET) system with a battery dominated power bus. The 147 A-hr battery is comparable to the one being designed for the Dragonfly mission. The solar array is sized to generate 1,410 W BOL and 1,184 W EOL with triple-junction GaAs cells that are commercially available. To mitigate environmental effects, the solar array has a full grout/dissipative design (similar to Van Allen Probes) and has six mil CMG coverglass with ITO. Due to the current draw during accelerator operations, the battery is providing most of the payload power during these operations with the arrays serving to hold up the battery charge throughout the night. The primary power bus of the spacecraft is a 100 V bus, which helps to mitigate the current draw on the battery during accelerator operations. Many COTS subsystem components are available in a 100 V configuration while other techniques can be used to reconfigure 28 V components to run on 100 V services (like wiring select heaters in series). Where needed, the reference design includes a 30 V down converter to provide a low-voltage power bus for select loads.

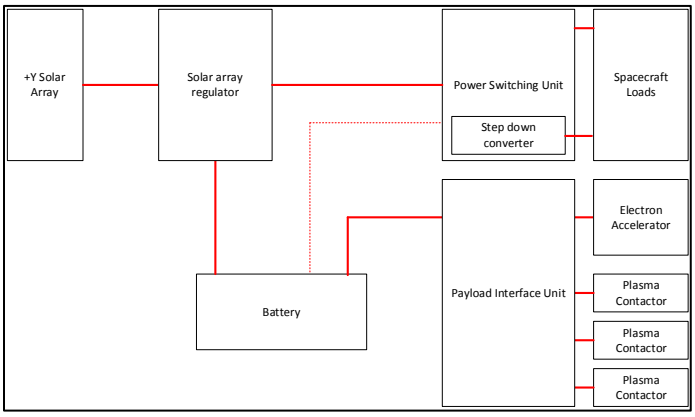

Figure 3-8: Notional schematic for MIO 100V architecture showing separate payload interface and step down converter for 28V loads

3.2.1.4. *Thermal*

The MIO mission can be accomplished with a passive, cold-biased thermal design. Preliminary modeling has shown that the bus and accelerator can be kept within temperature limits during hot and cold operating conditions as well as Cold safe modes. When not performing accelerator operations, the accelerator will be allowed to cool down to its survival limits before using operational heaters to bring it back to 25 C in preparation for firing. With 3, 0.5 second pulses separated by an average of 5 minutes, only 50% of the accelerator base plate is needed as a radiator. Since the base is facing the –X direction, this plate will be facing deep space during accelerator operations and will see the Earth only when the accelerator is not firing. For the rest of the bus, ~ 40% of ± Y panels are needed for radiators with the rest covered in MLI. Thermostatically controlled operational/survival heaters will be used on the payload and bus with additional heaters for thrusters. No bus-level heat pipes or louvers were needed for the reference design. The accelerator includes a set of heat pipes to maintain thermal stability across the central core.

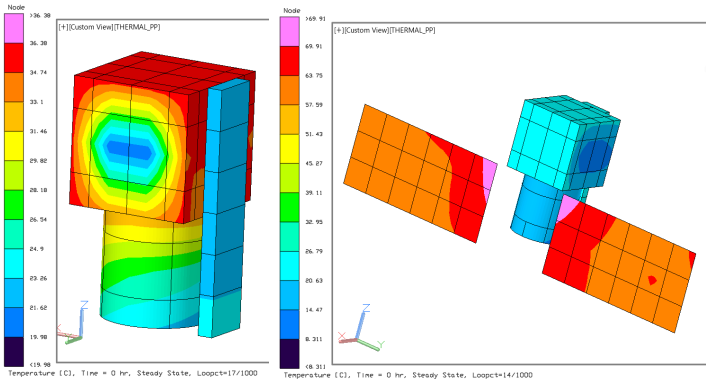

Figure 3-9: MIO can be run with a cold-biased thermal design, using the back of the accelerator to radiate heat between bursts.

3.2.1.5. *Avionics*

The avionics is a slice-based architecture with no special development needed. The reference design has a DC-DC converter, SBC, interface card, TAC, and SSR. The GPS receiver is also housed within

the avionics box. SpaceWire has been chosen for the high data-rate interfaces to the Accelerator, EFW instrument, and TT&C and UART (LVDS, RS-422) for other digital components. The reference design draws heritage from DART and PSP.

3.2.1.6. Guidance & Control

The G&C subsystem is sized to maintain 3-Axis control of the spacecraft with enough torque to manage multiple booms (1x 2 m, 2x 7 m) and a Plasma Contactor that generates disturbance torque when operating. No thruster firings are allowed when pulsing the Electron Accelerator so wheels have been sized to keep the accelerator aligned along the magnetic field line. The 8 attitude control thrusters are housed on the corners of the ± Z faces of the spacecraft and are angled to provide a torque about any axis. Thrusters will be used for detumble, momentum off-loading, trajectory control, and orbit disposal.

Sensors	Vendor/Model
Star Tracker x 1	Leonardo AA-STR (PSP, DART)
Inertial Measurement Unit x 1	Honeywell MIMU (DART)
Digital Sun Sensors (SSE x 1, DSSH x 6)	Adcole Sun Sensor Assembly (DART) Number of DSSH TBR based on s/c configuration
GPS Receiver (x 1) * RF to supply antenna(s)	Moog NavSBR GPS (MMS, GOES-R)

Actuators	Vendor/Model
Reaction Wheels (x 4)	Rockwell Collins/Teldix Space Wheels (PSP) RSI 2-76/60
Mono-propellant Thrusters	Aerojet 1 lbf (5 N) x 8

Since this is a Class C mission, the majority of the subsystem is single-string, but an additional reaction wheel has been incorporated due to the operating environment. A star tracker and IMU have been incorporated to meet the driving pointing/knowledge requirements (Pointing < 0.5°, Knowledge < 0.1°). In addition, the EDI and magnetometer measurements of the local magnetic field direction will need to be incorporated attitude control in order to aim the accelerator and keep the EDI and EFW instruments oriented properly. Sun sensors have also been included for detumble and safing and a GPS receiver has been included for navigation.

3.2.1.7. Flight Software

The Flight Software (FSW) subsystem can be built with heavy reuse from legacy software that provides a common set of applications for command management, telemetry, formatting, data recording and playback, autonomy, file management, and application scheduling that can be used with minimal changes/updates. A notional flight software design and its heritage is given in Figure 3-10. Some unique components would be required for a mission like MIO, but none that present any unsurmountable challenges from those normally solved during the FSW development for current missions. No major showstoppers or risks have been identified for this mission from a FSW perspective.

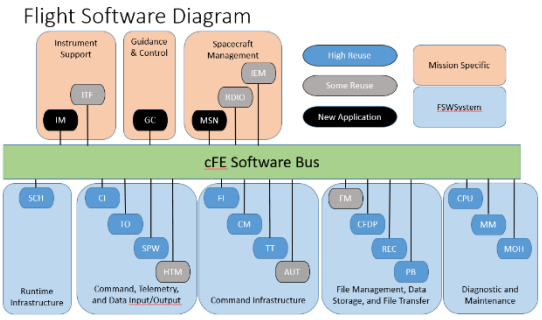

Figure 3-10 The FSW Architecture Concept built on cFE applications. As shown, nearly all applications in flight software system can be reused entirely, while there are some mission specific apps that will be customized for MIO, as is typical for any mission.

3.2.1.8. Telecommunications

The decision to use S-Band communications was driven by two factors: wide beamwidths to simplify crosslink and ground communications (the attitude of the spacecraft can be driven by the magnetic field and sun vector), and a desire to keep the daughtership design aligned with the Goddard MagCon concept which is also using S-Band.

The telecommunications architecture is also driven by how many channels can be allocated for the mission. It would be ideal to have 5 channels (one for each spacecraft), but this is unlikely. Having separate channels for mothership ground operations and daughtership communications would simplify the interfacing between the mission elements, but the notional design would allow the mission to be run via a single channel. The mothership configuration for ground communication (RX: 2025-2118 MHz; TX: 2200-2300 MHz) is opposite the crosslink configuration (RX: 2200-2300 MHz; TX 2025-2118 MHz). In the single-channel architecture, the mother initiates all crosslink operations and the ground station initiates all ground links. Recipient IDs are included in each message to make sure commands are only executed by the intended target.

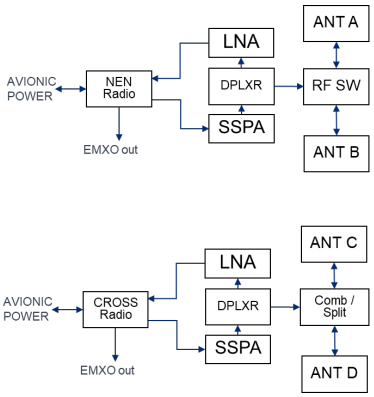

Figure 3-11: Notional schematics of mother TT&C to support ground communication and crosslinks

A frontier classic radio (VAP heritage) has been selected for the ground link, which also provides an oscillator for maintaining the system time. A 10 W SSPA is also included in the design. The crosslinks can either be closed via a frontier lite or Vulcan intersatellite link radio. +15 dBi patch arrays will be mounted on the ±X and ±Y faces to provide full coverage about the X-Y plane. With this design, the ground link is capable of downlinking at 5 Mb/s to the NSN and the crosslink is capable of 60 kb/s at a range of up to 500 km (65 minutes per day to transfer data at worst-case range). At < 300 km range, the crosslinks are capable of 100 kb/s which reduces the transfer time to < 40 minutes per daughter per day. Low rate communications (1 kbps) can also be established with a small, dedicated ground station (17.6 dBi Yagi at U of Calgary).

3.2.2. Daughtership

The daughters are spin stabilized spacecraft (5 RPM) with maximum dry mass of 77.4 kg. The spacecraft's octagonal bus is 0.9 m across and 0.4 m tall with 7 body-mounted solar panels (7 of the 8 octagonal faces) and two deployable booms for the magnetometer and antenna (figure 3-12). The notional design for these spacecraft are heavily influenced by the Goodard MagCon mission and either mission would benefit from the work done on the other.

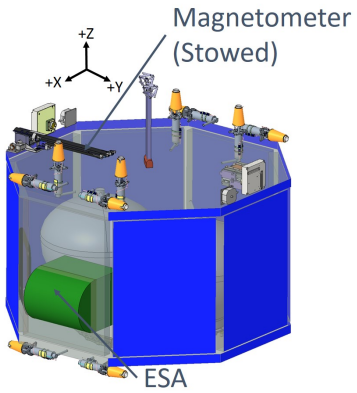

Figure 3-12: Daughtership showed in its stowed configuration. The magnetometer boom will deploy in the -Y direction.

3.2.2.1. Configuration/Mechanical

The daughters will be spinning about their Z-axis which is nominally pointed North out of the orbit plane. In this orientation, the solar panels, magnetometer (deployed on a 2m boom in the –Y direction), and ESA are oriented so that their faces/sensors will sweep about the spin axis. The antenna is aligned with the spin axis and raised in the +Z direction so that its beam pattern forms a torus in the X-Y plane. The –Z face houses a 15" lightband for mounting to the mother. Four thrusters are mounted on the +Z face for large maneuvers and two sets of four thrusters are mounted on the ±X faces to control the spin rate and precess the spin axis.

3.2.2.2. Propulsion

The daughter must be capable of maintaining its orbit and performing the end-of-life disposal maneuver (~330 m/s total) so a blowdown monoprop system has been sized with twelve 4.4 N (1 lbf) hydrazine thrusters (8 ACS, 4 delta-V) and two ATK 80444 diaphragm propellant tanks with MESSENGER heritage. Like with the mother, there is excess tank capacity that allows room for

spacecraft mass growth beyond current design margins. The remaining components are COTS with flight heritage.

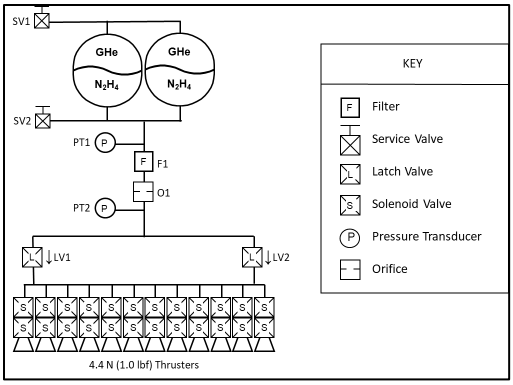

Figure 3-13: Notional schematic of the daughtership propulsion subsystem.

3.2.2.3. Electrical Power

The Electrical Power Subsystem (EPS) is a DET system with a 24-33 volt power bus and Single electronics unit for regulation and distribution. The solar arrays will produce 72 W BOL (61 W EOL) which is sufficient for most operations. The 12 A-hr battery has been sized to handle spacecraft maneuvers, specifically the end-of-life disposal. Just like the mothership, the solar array has a full grout/dissipative design (similar to VAP) and has six mil CMG coverglass with ITO.

3.2.2.4. Thermal

The daughters will use a passive, cold-biased thermal design, which benefits from the mission orientation to keep the internal temperature even. Thermostatically driven heaters will be selectively placed around the bus and radiators will be mounted on the ±Z faces.

3.2.2.5. Avionics

The avionics subsystem is fairly basic and can be constructed from any architecture capable of operating within the mission environment. The reference design is based on DART with a slice-based architecture containing a DC/DC converter, SBC, S/C interface card, TAC, and SSR. The avionics box also houses the GPS receiver.

3.2.2.6. Guidance & Control

The G&C subsystem has been sized to keep the spin-axis aligned to < 5° of orbit normal at nominal spin rate of 5 rpm. In addition, the subsystem has been designed to perform station-keeping and precession maneuvers in order to maintain the constellation geometry and execute the disposal maneuver. Nutation dampers will passively stabilize the spin axis while thrusters will set the spin rate and precess the spin axis. Higher accuracy SSAs (Sun Sensor Assemblies) have been selected in order to provide spin axis knowledge < 1° (driven by the payload) and a GPS receiver is included for navigation.

Sensors	Vendor/Model
Spinning Sun Sensor Assembly (SSE x 1, Heads x 2)	Adcole Spinning Sun Sensor Assembly (RBSP/VAP design)
GPS Receiver (x 1) * RF to supply antenna(s)	Moog NavSBR GPS (MMS, GOES-R)
Actuators	**Vendor/Model**
Nutation Dampers (x 2)	TBD
Mono-propellant Thrusters (x 8 ACS radial/spin plane)	Aerojet 0.2 lbf (1 N)

3.2.2.7. Flight Software

The Flight Software (FSW) subsystem can be built with heavy reuse from legacy software that provides a reused common set of applications for command management, telemetry, formatting, data recording and playback, autonomy, file management, and application scheduling that can be used with minimal changes/updates. Heavy reuse between the mother and daughters also provides an avenue for cost reduction. The team defined a notional set of operating modes (figure 3-14) along with a state machine that provide some insight into how the mothership coordination can be achieved with a fairly simple architecture.

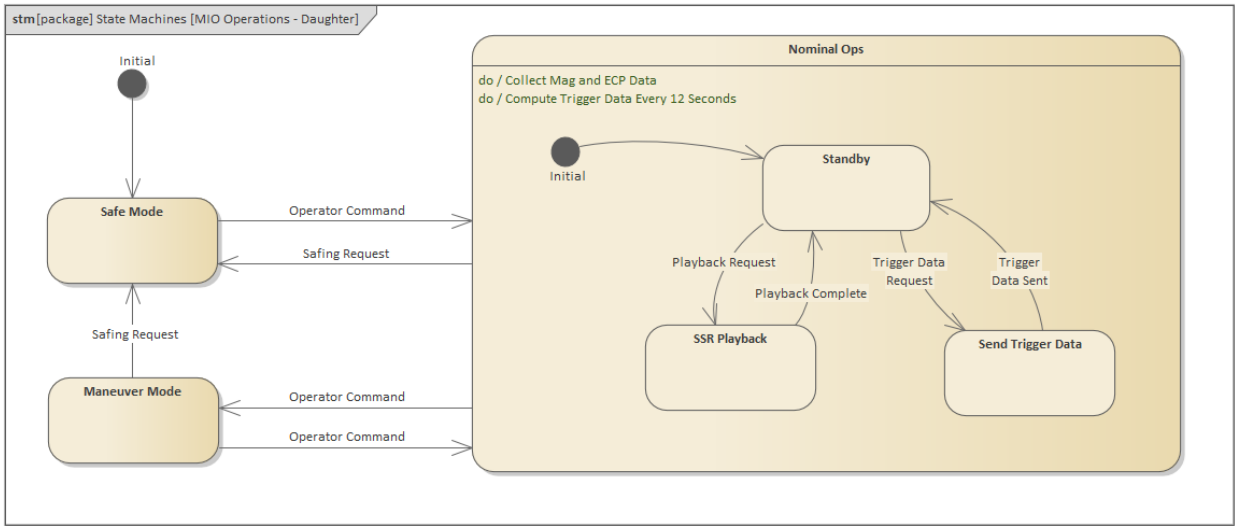

Figure 3-14: The daughters operate within a basic set of operational modes.

3.2.2.8. Telecommunications

The telecommunications subsystem aligns with the MagCon design with a Vulcan NSR-SDR-S/S radio and Garden Wiesel antenna. This architecture can support the crosslink to the mothership, commanding from the NSN, and low-rate, emergency command/telemetry from the dedicated ground station.

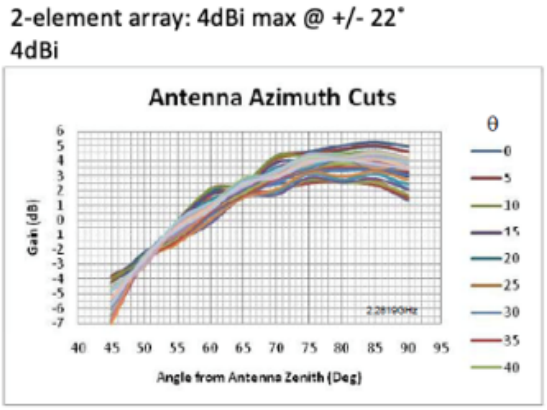

Figure 3-15: Garden Wisesel antenna performance.

3.3. Mission Design

The science drivers of the MIO mission require the spacecraft to fly through the transition region between the Earth's dipolar magnetic field and magnetotail and maintain a magnetic ground footprint that passes over the TREx PFISR, HAARP, and SuperDARN ground sensors in Northern Canada and Alaska. The resulting orbit is a 4.3 x 9 Re orbit (SMA = 42,164 km, e = 0.3565) with an inclination less than 5 degrees and a geographic ground track that wanders between Hawaii and the Eastern US. All spacecraft in the constellation are in roughly the same orbit with the daughters evenly spaced around a ~200 x 400 km relative orbit of the mother. The mission design analyses were performed with a Tsyganenko magnetic field model (T96 using IGRF internal, PS = 11.7°, I_{opt} = 3).

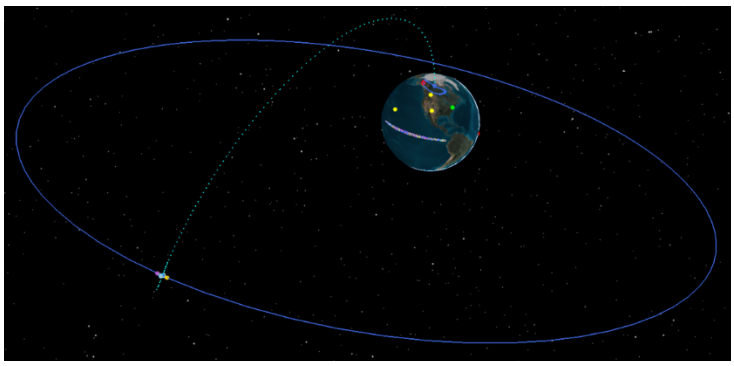

Figure 3-16: The MIO mission orbit with subsatellite ground track, magnetic ground track, and ground stations shown.

A variety of launch and insertion methods were considered for this study including direct injection to the mission orbit, launch to apogee (with and without inclination change), bi-elliptic transfers, and launch to LEO with EP spiral out. Cape Canaveral was the launch site for this study in order to stick with a generic launch vehicle. Future studies should evaluate lower latitude launch sites like Kwajalein if the specific launch vehicle is capable of launching from that site. A launch to the mission apogee has a C3 of -9.46 km^2/s^2 without accounting for the inclination change. Including the inclination change is a challenge without selecting a specific launch vehicle because there are different trajectories that balance the total time from launch to separation vs the total mass to orbit. We opted for a longer, more efficient trajectory and assessed the C3 of our launch to be close to 0 km^2/s^2 for a launch to the mission apogee at an inclination of 2° (26.4° inclination change). With this launch C3, the mission will need to use launch option 2. It is unlikely that the spacecraft will end up small enough to use option 1.

After separation, the mother will perform the 886 m/s perigee raise across three orbits before the daughters separate from the mother. Upon breakwire separation, the daughter will fire thrusters to spin up to desired spin rate (Sun Sensor Assembly in-the-loop during spin-up maneuver) before precessing the spin axis to align with orbit normal. The transition from deployment through the final mission orbit will take six days with each daughter performing up to 10.0 m/s of delta-V.

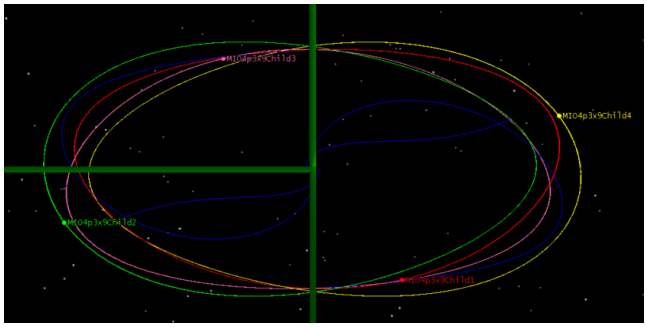

Figure 3-17: Relative orbits of daughter spacecraft about the mother (center of diagram)

Stationkeeping during nominal operations is focused on compensating eastward drift of the magnetic ground track and keeping Fairbanks within access. The two major disturbances that need to be corrected are period offsets due to the Earth J2, and constellation drift caused by solar pressure effects on the mother vs. the daughters. The mother and daughters will need 0.9 m/s per month on average in order to maintain the orbit semi-major axis and constellation phasing. This approach does not fix the locations of apogee and perigee, but they will drift a total of ~30 degrees across the mission

lifetime. This is acceptable for maintaining apogee near local midnight in the winter and perigee near local midnight in the summer.

At the end of mission, both the mothers and daughters need to perform a disposal maneuver of 242 m/s in order to raise the orbit perigee above the GEO graveyard. Other disposal options exist, but this is the most efficient.

3.3.1. ΔV Budget

The ΔV budget for the MIO spacecraft are provided in Table 3-2 and covers any launch year given the assumptions listed.

Table 3-3: MIO ΔV budget

Maneuver	Mother □V (m/s)	Daugher □V (m/s)	Assumptions
Orbit Insertion	886	-	Perigee Raise after launch to Apogee. Maneuver performed with daughters attached
Orbit Station-Keeping (2 years)	24	24	Hold semi-major axis to ± 10 km. 0.9 m/s per month average
Formation Station-Keeping (2 years)	8.2	51.8	Dominated by solar radiation pressure
Disposal	242	242	Raise Perigee to GEO graveyard
ACS	4	-	Momentum Dumping
Subtotal	**1164**	**318**	Total allocated ΔV
Unallocated Margin	**175**	**48**	15%
Total	**1339**	**365**	

3.4. Concept of Operations

The MIO mission involves two main modes of operations that are split between day and night. Accelerator operations take place only at night (weather permitting) and involve bursts of three, half-second pulses spaced at a minimum average of five minutes apart. Standby operations occur whenever the accelerator is not firing and involve continuous collection of payload data as well as planned mission maintenance operations.

Figure 3-18: A dual-yagi set up like this is baselined for the dedicated ground station.

A hybrid ground approach is recommended for this mission in order to mitigate costs while balancing data return and real-time commanding needs. The NSN will be used for data downlink and mission maintenance activities like command loads or software updates, while a small, dedicated ground station will be used for real-time triggers of pulses and updates to the operations schedule based on weather at the optical ground stations. It is recommended that the dedicated ground station be located at the University of Calgary so that it is collocated with TREx network operations. Any ground station can be used to communicate with any MIO spacecraft that is in safe mode.

3.4.1. Standby Operations

During standby operations, the mother is oriented with the solar arrays directly on the sun and the local magnetic field line aligned with the spacecraft's X-Z plane. This orientation optimizes power while keeping the EDI and EFW instruments in the correct orientation for data collection.

Various mission maintenance activities will be scheduled during the daylight hours each day. Each daughter will relay its recorded data to the mother for eventual downlink. These will be scheduled when the range between the spacecraft is less than 300 km in order to run at a higher data rate. Just like with other mother-daughter operations, these relay events are orchestrated by the mother and kicked off by a command from the mother to the daughter. Other periodic maintenance activities include data downlink (~3 times per week), momentum dumps, stationkeeping maneuvers, software/command sequence/ephemeris uploads, and telemetry monitoring. Data downlinking and uploads will require NSN passes, but other activities can be done via the dedicated ground station. If there is a need to do maintenance operations at night (orbit maintenance for example), the full moon provides an extended period each month where accelerator operations will not be possible.

3.4.2. Accelerator Operations

Accelerator operations will take place when it is night at the magnetic ground point of the spacecraft and observing conditions are optimal (clear skies, little moonlight). The accelerator will nominally fire one burst (three, half-second pulses) every five minutes, but there are two other conditions that may alter the timing: boundary detection and ground trigger. If either of these conditions are tripped, the next nominal burst is delayed in order to maintain the five minute average between bursts. There is no expectation that the other payloads (FGM, EDI, EFW) will collect good data during the bursts, but they should continue to collect data between bursts.

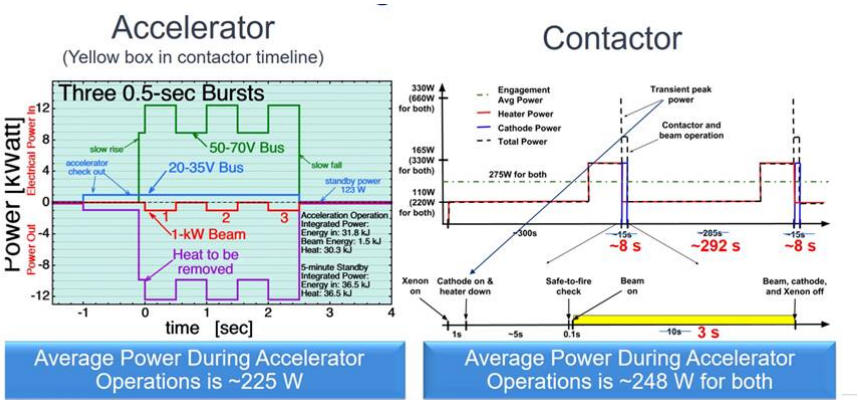

Figure 3-19: The coordinated operations between the accelerator and plasma contactor for accelerator operations.

The burst sequence involves coordinated activities between the Accelerator, FGM, Plasma Contactor, and EFW instrument. Burst –1 min: the plasma contactor increases the cathode heater power in preparation for firing. Burst -40 sec: main spacecraft tipped to align Accelerator with local magnetic field. Burst -20 sec: the EFW instrument performs a 20 second waveform capture. Burst -7 sec: plasma contactor heater lowers power and cathode powered on. Burst -2 sec: the plasma contactor emission is turned on. Burst -1 sec: the accelerator starts to checkout system and ramp up power and safe-to-fire checks are performed. Burst -0 sec: The accelerator and plasma contactor beams turn on. Burst +0.5 sec: accelerator completes first pulse, plasma contactor beam stays on. Burst +1 sec: accelerator performs second 0.5 second pulse. Burst +2 sec: accelerator performs thirst 0.5 second pulse. Burst +2.5 sec: Accelerator beam and plasma contactor emission turn off beams, accelerator powers down, and contactor cathode powers off. The accelerator control electronics and plasma contactor low power heaters remain on between bursts.

Boundary detection is performed onboard the mother with data from the daughters. Every twelve seconds, each daughter is completing a full revolution and can compute the ten values that need to be relayed to the mother ($\vec{B}$ $\vec{V}$ T_i T_e n_i n_e). During the next revolution, the mother commands each daughter, one at a time, to relay these values to her (< 3 seconds per daughter). After that, the

mother can do basic ratio calculations on the four data packets (40 values total) to determine if a boundary has been crossed and whether or not to initiate a burst.

Ground triggered bursts are initiated via ground command from the small, dedicated ground station. When the scientist is in the loop, the mother is in contact with the dedicated ground site and sending low rate telemetry on the health and status of the accelerator, plasma contactor, and vehicle. The operator will be able to see when the accelerator is firing and determine, based on data from the ground network, if there is a desire to manually trigger a burst.

3.4.3. Ground System

The Conceptual GDS Architecture needs to coordinate operations between the MOC, SOC, NSN, and dedicated ground station. Various architectures can be developed that are largely dependent on how much operational freedom is given to the scientist-in-the-loop and whether or not an operator is needed in the MOC for manual triggering of accelerator bursts. This will drive staffing costs as well as determine the flexibility of operations that can be performed via the dedicated ground station. A notional block diagram is provided in Figure 3-21 that shows an architecture where the SOC can trigger the bursts directly through the dedicated ground station, but operations at that site have been limited to pulsing operations only.

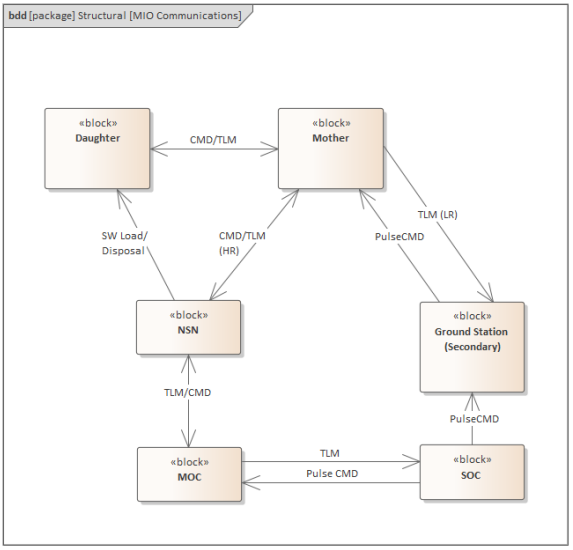

Figure 3-20: Command and control architecture to facilitate mission data handling as well as real-time operations.

3.5. Ground-Based Observatories

Ground-based imaging of the electron beam's interaction with the atmosphere is essential to the success of the MIO mission concept. To ensure this success, an expanded network of TREx imagers is costed as part of the mission. Other available ground-based scientific assets will be exploited in the MIO science. The MIO orbit has been chosen so that once every 24 hours the magnetic footpoint of MIO will pass in the vicinity of both the PFISR and HAARP facilities in Alaska. The SuperDARN radar network will certainly by utilized. And ground-based campaigns with MIO can be fielded.

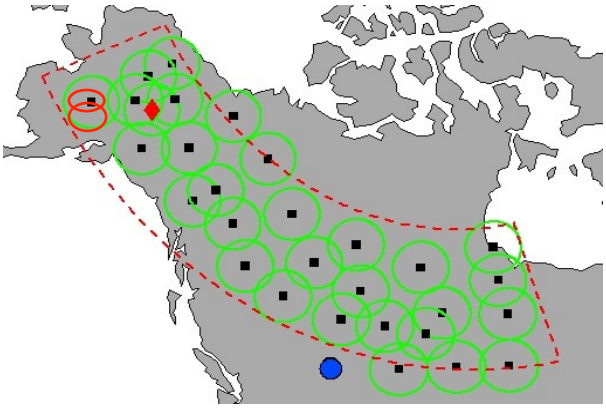

Figure 3-22 The locations costed for the extended TREx array of 29 optical imagers (black squares). The red triangle is Fairbanks between the locations of the PFISR and HAARP ionospheric facilities. The blue dot is the location of the University of Calgary ground station.

TREx Imaging: The 4.3x9 RE 24-hr orbit of MIO is chosen so that its magnetic footpoint in the atmosphere is imagable via the 427.8-nm band emission of nitrogen using an expanded ground-based array of TREx opitical imagers. The locations costed for the network of TREx imagers are shown in Figure 1. Each TREx imager will also be accompanied by a co-located white-light auroral all-sky imager. More information about TREx can be found at (https://www.ucalgary.ca/aurora/projects/trex). Emma Spanswick, the TREx PI, is on the science team for this MIO concept study.

PFISR: The Poker Flat Incoherent Scatter Radar is located at the Poker Flat Research Range north of Fairbanks. Besides the radar, the ionosphere and atmosphere over the Research Range are extremely well diagnosed with LIDAR, magnetometers, riometers, all-sky auroral cameras, a meridian-scanning photometer, a Fabry-Perot interferometer, low-light color auroral imager. More information about PFISR and PFRR can be found at (https://amisr.com/amisr/about/about_pfisr/) and (https://www.pfrr.alaska.edu/content/welcome-poker-flat). Roger Varney, the PI of PFISR, is on the science team for this MIO concept study.

HAARP: The High-frequency Active Auroral Research Program is an ionospheric-heater facility south of Fairbanks. It is also the site of extensive ionospheric diagnostics such as riometer, ionosonde, magnetometers, and auroral imagers. Ionosphere-Magnetosphere coupling experiments are possible with the coordination of HAARP heating activities with the magnetic footpoint of MIO. More information about HAARP can be found at (https://haarp.gi.alaska.edu). Jessica Matthews, the Program Manager for HAARP, is on the science team for this MIO concept study.

SuperDARN: An important diagnostic of ionospheric properties and convection is the Super Dual Auroral Radar Network network comprised of 24 radars in the northern hemisphere that fully cover the geographic area spanned by the MIO magnetic footpoint. More information about SuperDARN can be found at (http://vt.superdarn.org/tiki-index.php). Mike Ruohoniemi, who is a SuperDARN staff member at Virginia Tech, is on the science team for this MIO concept study.

Ground-Based Campaigns: Ground based campaigns can be fielded along various regions of the MIO footpoint track by moving portable facilities such as riometers, imagers, and ionosondes. A discussion of possible atmospheric and ionospheric scientific campaigns with MIO are discussed in the Appendix of Borovsky et al. [2020a]: these include atmospheric chemistry, ionization-recombination physics, atmospheric electricity, microburst electrodynamics, and triggering of thundercloud discharges.

3.6. Risk List

The top mission risks are listed below. They are classified as either technical, schedule, or cost/schedule. Likelihood and Consequence has been assessed for each.

A. Accelerator does not reach TRL-6:
   If the accelerator technical maturity does not reach TRL-6 by PDR, then the mission will not be able to perform its primary science [Cost/Schedule, Likelihood: 2, Consequence: 5]. The accelerator is a key enabler of this mission so technology maturation efforts should be pursued prior to the detailed design and integration of the MIO mission. There is some flexibility in this risk in that the likelihood is dependent on the work done before mission selection. Development and maturation efforts are discussed in appendix A.2.

B. Ground test of accelerator operations:
   If the accelerator operations cannot be ground-tested with the integrated flight system, then there is a risk of failure when fired for the first time on orbit [Technical, Likelihood: 1, Consequence: 5]. An iterative approach to testing the accelerator at various power levels is discussed in the appendix in order to test out the hardware before integration with the spacecraft. In addition, the fault management of the spacecraft includes analysis and mitigation of impacts due to off-nominal accelerator firing. A test of the full fight unit will have to take place in a large chamber with a GSE cap that will conduct the energy out of the chamber. The B-SPICE mission will fly an accelerator/contactor pair on a NASA LCAS rocket, providing an opportunity for in-space demonstration prior to mission selection.

C. Daughtership hardware failure in environmental testing:
If a hardware failure is experienced during daughtership environmental testing on a unit other than the first unit, then previously delivered hardware will need to be proven unaffected or potentially retested [Cost/Schedule, Likelihood: 1, Consequence: 4]. Qualification testing on the first daughter prior to integration of the remaining daughters increases the likelihood of finding common failures prior to integrating the remaining spacecraft.

D. I&T Staff and Facilities:
If adequate Staff and Fabrication Facilities for flight builds are not available during Phase C, then Phase D and SIR will be delayed [Schedule, Likelihood: 1, Consequence: 3]. Three daughters and the mother will be integrated at the same time. These units can be built at different facilities in order to ease the burden on any one site or staff. Integrating one daughter early will help to work out the I&T issues on the daughters before mothership I&T begins. Additionally, the GSE for the mother is different from the daugthers, further separating the I&T facility impacts between the mother and daughters.

E. Mother-daughter interface changes after first daughter has been integrated:
If the design of the mother changes after the first daughter I&T begins, then it could cause changes to the mother-daughter interface and impact the I&T of the daughter [Cost/Schedule, Likelihood: 1, Consequence: 2]. A change to the mother that impacts the physical interface to the daughter is unlikely late in the design phase. ESPA-like launch interfaces are very mature and the keep-out zones for daughter-accommodation will have some margin. This will only impact the first daughter to be integrated.

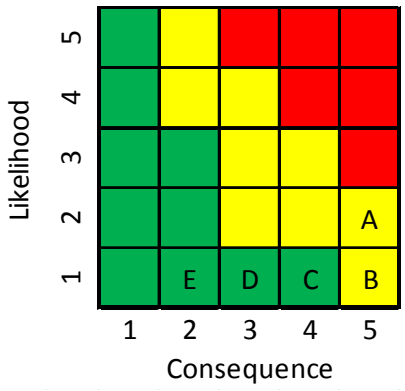

Figure 3-23: Risk Matrix for MIO

4. Development Schedule and Schedule Constraints

The High-Level Mission Schedule for MIO (Figure 4-1) is based upon DART, a mission of analogous scope and complexity for the main spacecraft. The complexity of the Mothership is the main driver and focus of the schedule. The four Daughterships are less complex and not expected to drive the schedule. More detail into I&T is available in Appendix A.7.

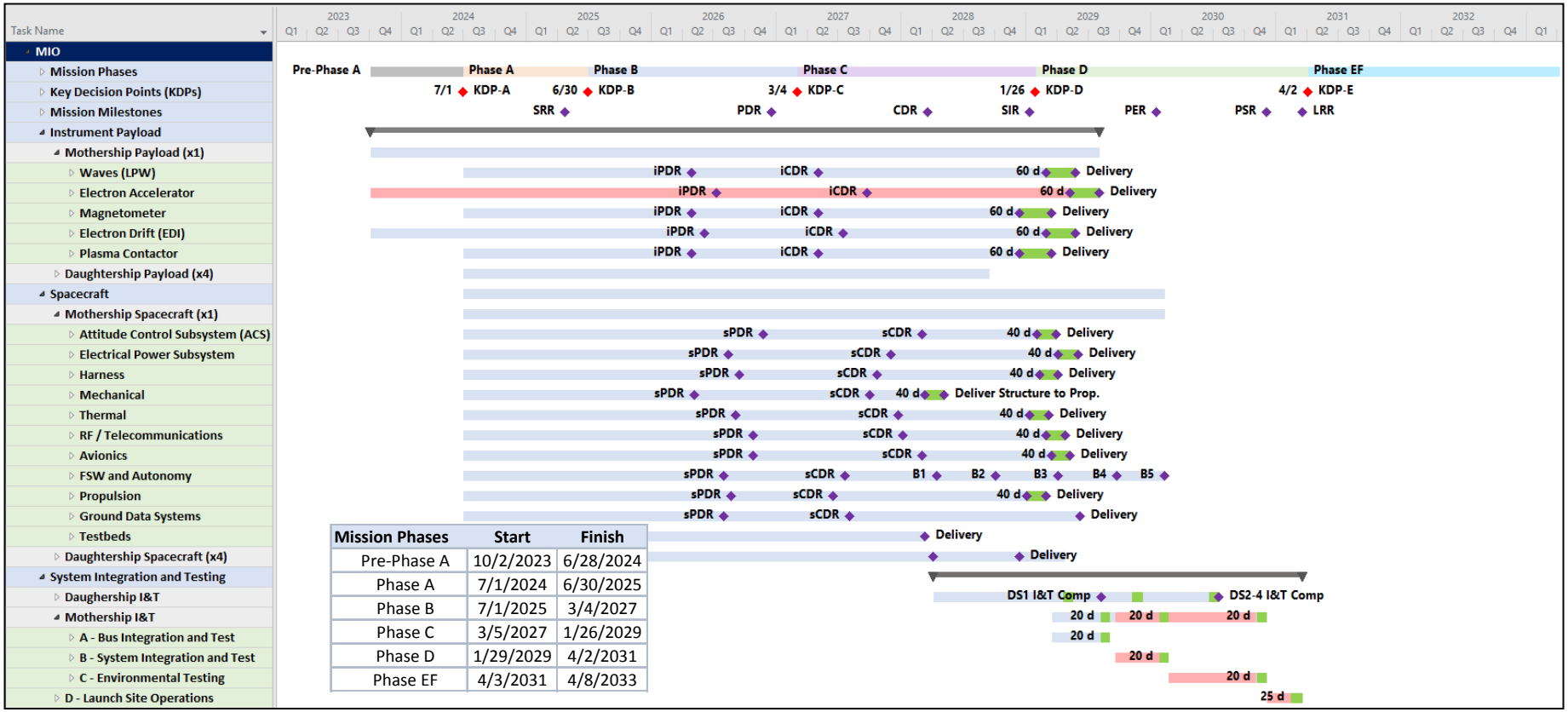

Mission Phases	Start	Finish
Pre-Phase A	10/2/2023	6/28/2024
Phase A	7/1/2024	6/30/2025
Phase B	7/1/2025	3/4/2027
Phase C	3/5/2027	1/26/2029
Phase D	1/29/2029	4/2/2031
Phase EF	4/3/2031	4/8/2033

Figure 4-1MIO Mission Schedule

Table 4-1: Key phase duration table

Project Phase	Duration (Months)
Pre-Phase A	9 mos.
Phase A – Conceptual Design	12 mos.
Phase B – Preliminary Design	20 mos.
Phase C – Detailed Design	23 mos.
Phase D – Integration & Test	26 mos.
Phase E/F – Primary Mission Operations / Extended Mission Operations	24 mos.
Start of Phase B to PDR	18 mos.
Start of Phase B to CDR	33 mos.
Start of Phase B to Delivery of Waves (LPW)	47 mos.
Start of Phase B to Delivery of Electron Accelerator	50 mos.
Start of Phase B to Delivery of Magnetometer	45 mos.
Start of Phase B to Delivery of Electron Drift (EDI)	47 mos.
Start of Phase B to Delivery of Plasma Contactor	45 mos.
Start of Phase B to Delivery of Attitude Control Subsystem (ACS)	46 mos.
Start of Phase B to Delivery of Electrical Power Subsystem	48 mos.
Start of Phase B to Delivery of Harness	46 mos.
Start of Phase B to Delivery of Thermal	45 mos.
Start of Phase B to Delivery of RF / Telecommunications System	46 mos.
Start of Phase B to Delivery of Avionics	47 mos.
Start of Phase B to Delivery of Propulsion System	45 mos.
System Level Integration & Test	24 mos.
Project Total Funded Schedule Reserve	6 mos.
Total Development Time Phase B - D	70 mos.

4.1. Science, Technology Development Plan(s)

The Electron Accelerator is not currently at TRL 6. Work will begin in Pre-Phase A c two instruments to advance the TRL prior to PDR. All other instruments and sp components are at TRL 6.

4.2. Development Schedule and Constraints

The development phase critical path includes the development and delivery of the E Accelerator instrument followed by the remaining spacecraft integration and testing activiti also Section 5.4 and Appendix A.2.1) The schedule contains a total of 6 months of funded s reserves. The Primary Launch Period is spring of 2031, but the schedule can be shifted to lat while maintaining a spring launch.

5. Mission Life-Cycle Cost

5.1. Introduction

The cost estimate prepared for the MIO mission is of Concept Maturity Level (CML) 4. The payload and spacecraft estimates capture the resources required for a preferred point design and take into account subsystem level mass, power, and risk. Our estimate also takes into account the technical and performance characteristics of components. Estimates for Science, Mission Operations, and Ground Data System elements whose costs are primarily determined by labor take into account the Phase A–D schedule and Phase E timeline.

The result is a mission estimate that is comprehensive and representative of expenditures that might be expected if the MIO mission is executed as described. The MIO Phase A–F baseline mission cost, including Launch Vehicle (LV) and unencumbered reserves of 50% (A–D) and 25% (E–F), is $1.3B in fiscal year 2022 dollars (FY22$), as shown in Table 5-1. Excluding all LV-related costs, the MIO Phase A–D mission cost with reserves is $1.1B FY22. All tables and estimates below refer to the baseline mission configuration, with the exception of the descope estimate, which follows the baseline Confidence and Cost Reserves section.

Table 5-1. Estimated Phases A–F MIO baseline mission cost by level 2 WBS element.

MIO Mission Estimate - Baseline (FY22$M)					
WBS	**Description**	**Ph A-D**	**Ph E-F**	**Total**	**Notes**
	Phase A	**$ 6.0**	**$ -**	**$ 6.0**	Assumption based on previous studies
1/2/3	**PM/SE/MA**	**$ 91.8**	**$ -**	**$ 91.8**	B-D: Wrap factor based recent NFs and APL missions. E-F: Bookkept with WBS 7
4	**Science**	**$ 19.7**	**$ 19.1**	**$ 38.8**	Cost per month of recent NFs and APL missions
5	**Payload**	**$ 173.7**	**$ -**	**$ 173.7**	Parametric based estimates
6	**Spacecraft**	**$ 338.6**	**$ -**	**$ 338.6**	Parametric and analogy based estimates
7	**Mission Operations**	**$ 11.4**	**$ 22.5**	**$ 33.9**	Based on VAP
8	**LV**	**$ 200.0**	**$ -**	**$ 200.0**	Option 2
9	**Ground Data Systems**	**$ 16.1**	**$ 1.7**	**$ 17.8**	Ground ROMs from SMEs
10	**I&T**	**$ 65.1**	**$ -**	**$ 65.1**	APL historical I&T % of HW (incl testbeds)
	Subtotal	**$ 922.4**	**$ 43.3**	**$ 965.7**	
	Reserves	$ 358.2	$ 10.8	$ 369.0	50% B-D, 25% E-F, excludes launch services costs
	Total w/Reserves	**$ 1,280.6**	**$ 54.2**	**$ 1,334.7**	**FY22$M**

5.2. Mission Ground Rules and Assumptions

- Estimating ground rules and assumptions are derived from the "Ground Rules for Mission Concept Studies in Support of Heliophysics Decadal Survey" dated January 2022.
- Mission costs are reported using the level-2 (and level-3 where appropriate) work breakdown structure (WBS) provided in NPR 7120.5F.
- Cost estimates are reported in fiscal year 2022 (FY22) dollars.
- The NASA New Start inflation index was used to adjust historical cost, price data, and parametric results to FY22 dollars if necessary.
- The mission requires Technology Development dollars (Pre-Phase A) to advance the Accelerator instrument to TRL 6. The estimate for the technology development is discussed in

the Payload section and is outside of the total mission cost per the guidelines. All other MIO mission components will be at or above TRL 6 when required.

- A launch vehicle cost estimate of $200M is held in WBS 8, corresponding to Launch Vehicle Option 2 from the "Ground Rules for Mission Concept Studies in Support of Heliophysics Decadal Survey" dated January 2022.
- A 44% cost to copy factor is applied to all copies of instruments and spacecraft (Whitley 2013).
- Phase A–D cost reserves are calculated as 50% of the estimated costs of all components excluding the launch vehicle. Phase E–F cost reserves are calculated as 25% of the estimated costs of all Phase E elements excluding DSN aperture fees.

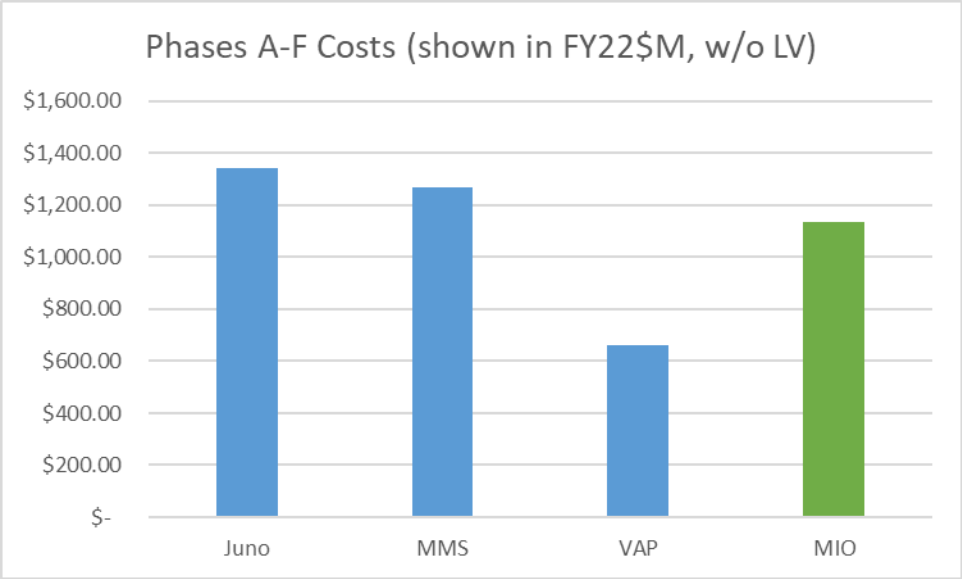

Figure 5-1. Mission-level cost comparison to other analogous missions.

5.3. Cost Benchmarking

The cost and scope of the MIO concept corresponds well with NASA missions of similar complexity (see Figure 5-1). The estimated cost to develop MIO compares favorably to current analogous missions under development as well as past missions, excluding launch vehicle costs.

5.4. Methodology and Basis of Estimate

The MIO CML 4 mission cost estimate is a combination of high-level parametric and analog techniques and incorporates a wide range of uncertainty in the estimating process. No adjustments were made to remove the historical cost of manifested risk from the heritage data underlying the baseline estimate. Therefore, before reserves are applied, the estimated costs already include a historical average of the cost of risk. This approach is appropriate for capturing risk and uncertainty commensurate with early formulation stages of a mission. The following describes the basis of estimate for each element.

WBS 1, 2, 3 Project Management, Systems Engineering, Mission Assurance (PM/SE/MA)

Because these functions depend on multiple mission- and organization-specific characteristics (Hahn, 2014), cost analogies to comparable historical missions are preferred over cost model output, which does not take the mission into account. Existing analyses demonstrate that hardware costs are a reliable predictor of these critical mission function costs. APL has conducted thorough and rigorous analyses of PM/SE/MA costs, both for historical APL missions and for analogous missions. The PM/SE/MA estimate for MIO relies on APL's analysis of historical PM/SE/MA practices on Van Allen Probes (VAP), Parker Solar Probe (PSP), and New Horizons (NH). VAP and PSP in particular include costs associated with current NASA requirements (e.g., Earned Value Management System [EVMS], 7120.5F). MIO's total mission PM/SE/MA cost is 15.9% of the flight system (payload + spacecraft + I&T). This percentage is allowed to vary along with hardware costs as part of the mission cost risk analysis, discussed below, to capture uncertainty (particularly given CML-4-level design phase).

WBS 4 Science

This element covers the managing, directing, and controlling of the science investigation. It includes the costs of the Principal Investigator (PI), Project Scientist (PS), science team members, and activities. The Phase A–D and E–F science estimate is an analogous estimate based on the cost per month of NH, MESSENGER, Dragonfly, OSIRIS-REx, and Juno. The analogy costs are representative of expenditures for science on a typical Discovery or New Frontiers mission. The estimate reflects the manpower needed to create various data products as well as to ensure closure to science objectives.

WBS 5 Payload

The WBS 5 estimate includes a science payload of five instruments on the mothership, 2 instruments plus an electronics box on each of the four daughterships and payload-level PM/SE/MA. Cost shown in Table 5-2 reflect the first unit instrument estimate, plus a 44% cost to copy factor (Whitley 2013) for subsequent units for the daughterships. The 8.2% cost-to-cost factor for estimating payload PM/SE/MA costs is based on the VAP, NH, MESSENGER, and PSP payload suite cost data with PM/SE/MA costs estimated as a percentage of the payload hardware. Technical management and systems engineering costs for individual instruments are carried in their respective instrument development costs.

Given the early design phase, multiple approaches are used to estimate each instrument to capture the potential range in cost. This includes two parametric estimates that rely on different sets of input variables (SEER Space and NICM 9). Historical analogous for heritage instruments were not available. The closest analog missions are either too old (Polar) or do not provide detail at the instrument level (MMS). Therefore, an average of the two parametric estimates is used as the point estimate to prevent estimate bias (high or low). These estimates are subject to a cost risk analysis (discussed below) to further quantify uncertainty.

There is technology development required for the Accelerator instrument (cf. Appendix A.2.1). This technology development will occur prior to Phase A, and is estimated to be $27.1M-52.4M FY22$. This estimate is kept outside of the cost table shown here per the study report guidelines. The schedule provided in Section 4 is notional and can be adapted to accommodate the technology development of the Accelerator. The MIO mission merely requires a spring launch with a science campaign that spans two winters and two summers.

Table 5-2. WBS 5 costs in FY$22M.

MIO Mission Estimate - Baseline (FY22$M)			
WBS	**Description**	**Ph A-D**	**Notes**
5	**Payload**	**$ 173.7**	Parametric based estimates
	PL PM/SE/MA	*$ 13.2*	*Based on VAP, NH, MESSENGER, PSP*
	Mothership Payload	*$ 143.1*	*NICM 9 and SEER Space Average*
	MAG	$ 3.9	
	Accelerator	$ 102.2	
	Plasma Contactor	$ 24.4	
	EDI	$ 10.3	
	LPW	$ 2.2	
	Daughtership Payloads (4)	*$ 17.4*	
	MAG	$ 6.1	
	ESA	$ 7.0	
	Electronics Box	$ 4.3	

The main strategy for increasing TRL and reducing cost of an Accelerator instrument would be to build a scaled down laboratory accelerator test stand in a space flight like configuration. The Accelerator concept is intentionally designed to be modular. A laboratory test stand consisting of a small number of Accelerator zones would be sufficient for maturing key technologies. The test Accelerator would then be relatively easy to scale up since it simply means adding more "zones" with identical hardware. (See App. A.2.1)

WBS 6 Spacecraft

The WBS 6 spacecraft (SC) estimate includes the mothership, the four daughterships, component engineering and flight software (Table 5-3). SC PM/SE/MA is carried in WBS 1, 2, and 3 consistent with APL in-house builds [Hahn 2015]. The basis of estimate relies primarily on historical $/kg analysis and parametric models. SEER Space is one of the primary estimating methodologies because it was designed specifically for missions in early formulation stages. The exception to this is the SC propulsion systems and flight software which are estimated via a ROM by subject-matter experts. No major technology development is required for the SC. A 44% cost to copy factor is applied for the second, third and fourth daughtership units (Whitley 2013).

The MIO FSW ROM is leverages significant code re-use from other missions. The operating modes are basic since science modes and safe mode have similar attitudes for all spacecraft. Data rates are low (~35 kb/s) allowing for older, hardware-based solutions to be employed. There are several protocols that support the mission and are also able to handle the added complexity due to the mother-daughter crosslinks. This includes options like CCSDS AOS symmetric protocol, or an approach where crosslink operations are orchestrated by the mother which can reuse software that governs the relationship between prime and spare SBCs. Since the spacecraft are single string and safe modes similar to operating modes, the autonomy complexity is at the lower end, closer in scope to missions like DART and Van Allen Probes. Although autonomy will need to be developed for two different busses, code will be reused across the two. Finally, the Daughtership ADCS software will be reused from prior spinning missions with minor modifications. The ADCS software for the mothership will also benefit from extensive reuse, with modifications to incorporate EDI measurements into the controller when trying to point the Accelerator along the magnetic field line.

MIO Mission Estimate - Baseline (FY22$M)			
WBS	**Description**	**Ph A-D**	**Notes**
6	**Spacecraft**	**$ 338.6**	Parametric and analogy based estimates
	Mothership	**$ 179.9**	1 spacecraft
	Mechanical	$ 31.2	All subsystem estimates utilize both historical $/kg analysis of previous APL S/C builds and parametric SEER Space results. S/C PM/SE/MA is held in WBS 1-3
	Avionics	$ 36.8	
	Power	$ 45.4	
	GNC	$ 28.1	
	Thermal	$ 4.7	
	RF	$ 8.7	
	Harness	$ 4.9	
	Prop	$ 11.2	ROM via subject matter expert
	Component Engineering	$ 9.0	VAP
	Daughterships (4)	**$ 145.6**	4 spacecraft, 44% copy factor
	Mechanical	$ 4.0	All subsystem estimates utilize both historical $/kg analysis of previous APL S/C builds and parametric SEER Space results. S/C PM/SE/MA is held in WBS 1-3
	Avionics	$ 71.5	
	Power	$ 11.2	
	GNC	$ 16.3	
	Thermal	$ 0.8	
	RF	$ 10.2	
	Harness	$ 0.5	
	Prop	$ 13.8	ROM via subject matter expert
	Component Engineering	$ 17.4	VAP
	FSW	**$ 13.1**	ROM via subject matter expert

Table 5-3. WBS 6 costs in FY$22M.

WBS 7 and 9 Mission Operations (MOps) and Ground Data Systems (GDS)

The MIO mission operations estimate includes mission operations planning and development, network security, data processing, and mission management. The pre- and post-launch mission operations estimates are based on VAP with insight from recent proposal submittals. VAP represents expenditure on pre and post-launch MOps of a project of comparable scope and complexity. The GDS estimate is a BUE from a ground data systems subject matter expert. The MIO Ground Data system provides full life cycle support for Subsystem Test, Observatory I&T, Hardware Simulator Control, & Flight Operations. The cost estimate is based on extensive reuse of PSP, IMAP, and DART Ground Software via JHU/APL's Mission Independent Ground Software (MIGS) as well as use of the existing Mission Operations Center (MOC). An additional estimate for the use of the Transition Region Explorer (TREx) imaging facility is also included. The University of Calgary provided the estimate, which has been converted from CAD to USD using the exchange rate of $1 USD per $1.26 CAD (rate on 04/21/22).

WBS 8 Launch Vehicle and Services

The mission requires a launch vehicle that corresponds with Option 2 of the options described in the Decadal Survey Ground Rules.

WBS 10 System Integration and Testing (I&T)

This element covers the efforts to assemble and test the mothership, daughterships and instruments. The MIO I&T effort is estimated as 12.7% of the hardware. This percentage is based on a detailed analysis of cost actuals from previous APL missions, including MESSENGER, NH, STEREO, VAP, and PSP. This percentage is allowed to vary along with hardware costs as part of the mission cost risk analysis to capture the risk historically manifested during I&T.

Deep Space Network (DSN) Aperture Fees

This element provides for access to the DSN infrastructure needed to transmit and receive mission and scientific data. Costs for DSN are not applicable to MIO.

5.5. Confidence and Cost Reserves

The cost risk ranges by major WBS element as inputs for the MIO probabilistic cost risk analysis to quantify total cost risk are found in Table 5- and are described below.

Table 5-4. Inputs to cost distributions in FY$22M.

MIO (FY22$M)			
WBS		Point	High
	Phase A	$ 6.0	$ 6.0
1,2,3	PMSEMA	$ 91.8	$ 126.8
4	Science	$ 38.8	$ 48.5
5	Payload	$ 173.7	$ 229.5
6	Spacecraft	$ 338.6	$ 478.2
7	Mission Operations (MOps)	$ 33.9	$ 42.3
8	Launch Vehicle	$ 200.0	$ 200.0
9	Ground Data Systems (GDS)	$ 17.8	$ 22.3
10	Integration & Test (I&T)	$ 65.1	$ 89.9

PM/SE/MA

Given the use of cost-to-cost factors to estimate these functions, both the CER and underlying cost drivers are allowed to range so that all sources of uncertainty can be quantified.

Science, GDS, and MOps

These are low-risk cost elements but are subject to cost growth as part of the cost risk analysis.

Payload

The 70th percentile cost model estimate is used to inform the MIO payload risk model to capture the uncertainty given the CML-4-level design phase.

Spacecraft

Each subsystem is subject to a data-driven risk analysis based on historical APL cost growth. Mass input also varies in the SEER model consistent with early design programs to 30% over current best estimate.

I&T

I&T as a percentage of the payload and spacecraft from the point estimate is used to inform the risk analysis, allowing I&T to vary with hardware cost.

Figure 5-2. S-curve summary.

Table 5-5. Cost risk analysis. The estimate includes unencumbered cost reserves of 50% of the estimated costs of all Phase A–D elements except for the launch vehicle. A probabilistic cost risk analysis shows 76.0% confidence that the mission is achievable within the estimated costs of this study.

Description	Value (FY22$M)	Confidence Level
Point Estimate	$ 965.7	46.2%
Mean	$ 1,102.3	
Standard Deviation	$ 474.7	
Reserves	$ 369.0	
Total w. Reserves	$ 1,334.7	76.0%

The high confidence level is driven primarily by the large cost reserves for this pre-proposal concept. Given a typical competitive pre-Phase A NASA environment with 25% reserves on Phase A–D elements and 10-15% on Phase E-F, the probabilistic cost risk analysis shows 64.2% confidence that the mission would be achievable. A 50th- to 70th-percentile confidence level is expected and reasonable for a pre-Phase A concept with this level of reserves.

A coefficient of variation (standard deviation/mean) of approximately 43% indicates appropriate levels of conservatism given the early formulation phase. The model confirms the point estimate and provides a reasonable basis for the MIO CML-4 study.

5.6. De-Scope Options

The following describes the MIO mission de-scope option. The same estimating methodologies for the baseline mission was applied to the de-scope option.

De-Scope 1

The de-scope option takes the baseline mission and removes the four daughterships and adds two ESAs to the mothership. There are no changes to the launch vehicle assumption from the baseline mission. The summary cost estimate for De-Scope 1 is shown in Table 5-6.

Table 5-6. De-Scope 1 summary estimate (FY22$M).

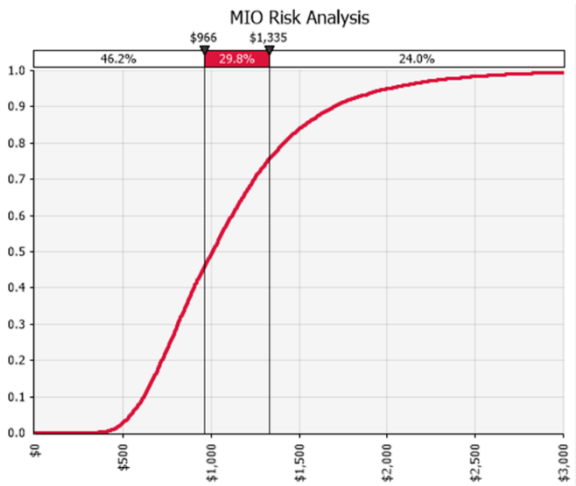

MIO Mission ROM Estimate - Descope 1				
WBS	Description	Ph A-D	Ph E-F	Total
	Phase A	**$ 6.0**	**$ -**	**$ 6.0**
1/2/3	**PM/SE/MA**	**$ 61.6**	**$ -**	**$ 61.6**
4	**Science**	**$ 16.3**	**$ 19.1**	**$ 35.4**
5	**Payload**	**$ 159.7**	**$ -**	**$ 159.7**
	PL PM/SE/MA	*$ 12.1*	$ -	*$ 12.1*
	MAG	$ 3.9	$ -	$ 3.9
	Accelerator	$ 102.2	$ -	$ 102.2
	Plasma Contactor	$ 24.4	$ -	$ 24.4
	EDI	$ 10.3	$ -	$ 10.3
	LPW	$ 2.2	$ -	$ 2.2
	ESA (2)	$ 4.5	$ -	$ 4.5
6	**Spacecraft**	**$ 184.1**	**$ -**	**$ 184.1**
	Mothership	$ 170.9	$ -	$ 170.9
	FSW	$ 13.1	$ -	$ 13.1
7	**Mission Operations**	**$ 11.4**	**$ 22.5**	**$ 33.9**
8	**LV**	**$ 200.0**	**$ -**	**$ 200.0**
9	**Ground Data Systems**	**$ 16.1**	**$ 1.7**	**$ 17.8**
10	**I&T**	**$ 43.7**	**$ -**	**$ 43.7**
	Subtotal	**$ 698.8**	**$ 43.3**	**$ 742.1**
	Reserves	$ 246.4	$ 10.8	$ 257.2
	Total w/Reserves	**$ 945.2**	**$ 54.2**	**$ 999.3**

De-Scope Considerations

The mission impacts of de-scoping the various individual instruments on the main spacecraft and the daughter spacecraft have been considered. For viable de-scope options, the impacts would be the following.

- ***Enhanced Density of Ground-Based Optical Imagers:*** The MIO mission has built in a design to increase the spatial density of the TREx ground-based imagers. A denser network of imagers means the optical beamspot is nearly always closer to an imager and easier to detect in the presence of aurora. Making the imager network denser is a trade decision: increasing the density of the imagers is a much easier solution than increasing the power of the electron accelerator. Furthermore, it is a much more cost-effective option.
- ***Waves on the Main Spacecraft:*** Eliminating the Waves instrument on the main spacecraft is a viable de-scope option, with a resulting reduction in science. Eliminating Waves reduces the science ability to discern the magnetospheric drivers of certain auroral and ionospheric phenomena, and eliminating Waves prevents the mission from determining the plasma density when the density is high preventing the identification of the plasmasphere and the boundary of the plasmasphere (plasmapause).
- ***Eliminating one of the four Daughter Spacecraft:*** The MIO mission goals are still fully attainable, unless one of the remaining three daughters fails.
- ***Eliminating All four of the Daughter Spacecraft:*** This is the de-scope option called "MIOcore" that was budgeted in this study, saving ~$300M. This de-scope option impacts science objective 4 of the mission "Determine in what ways the magnetosphere drives field-aligned currents". Without the 4 daughters, the critical magnetospheric gradients cannot be well quantified, but they can be identified to identify the mechanisms operating to drive currents. If desired, select redundancy may be considered to increase the reliability of the Mother Spacecraft – this has not been reflected in this study.

- *Electrostatic Analyzers on the Daughter Spacecraft:* Eliminating ESAs on the daughters defeats the purpose of having the daughter spacecraft. In this case, it makes sense to go to de-scope-option MIOcore eliminating the 4 daughter spacecraft.
- *Magnetometers on the Daughter Spacecraft:* Eliminating magnetometers on the daughters defeats the purpose of having the daughter spacecraft. In this case, it makes sense to go to de-scope-option MIOcore eliminating the 4 daughter spacecraft.
- *Reducing the power of the Electron Accelerator:* Reducing the power of the accelerator is a great risk to the success of the mission, disabling the ability to connect the magnetosphere with the ionosphere in the presence of aurora. (For changes in the accelerator design, see Appendix A.2.2 for accelerator trades.)

The Electron Accelerator, Plasma Contactor, Magnetometer, and EDI (Electron Drift Instrument) on the Main Spacecraft are not viable de-scope options. These are all crucial to accelerator operations. There is no point to the MIO mission without the accelerator used to connect the magnetosphere and the ionosphere.

A. Appendices

A.1. Beam Operation and Detection

A.1.1. Safety of MIO Operations

Gian Luca Delzanno and Joe Borovsky

Two aspects of safe operation are considered in this appendix and operational safety measures are described for both. The first discussion is on the mitigation of spacecraft charging on the MIO main spacecraft when the electron accelerator is fired and the second discussion is about other spacecraft being hit by the MIO 1-MeV electron beam.

A.1.1.1. Spacecraft Charging Mitigation

Firing the 1-mA MIO electron accelerator for 0.5 sec removes 5×10^{-4} C of negative charge from the main MIO spacecraft. In the tenuous magnetospheric plasma the spacecraft is by no means grounded and will charge positively to a high Voltage. In Figure 1 an orbit-motion-limited (OML) calculation [Mott-Smith and Langmuir, 1926] of the charging of a 1-meter-radius spacecraft in a hot low-density ($n = 1$ cm^{-3}, $T_e = 1$ keV) magnetospheric plasma with a 100 nT magnetic field is calculated for the beam properties of MIO. The 0.5-sec beam-on interval consists 100 pulses of 10 mA of current that are each of 500 μs in duration with 4500-μs intervals of beam off between the pulses. In Figure 1 the potential of the main spacecraft with respect to infinity is plotted as a function of time. As can be seen, the potential of the spacecraft rapidly reaches ~100 kV positive and oscillates with the 200-Hz beam pulsing. When the beam is turned off, the spacecraft potential decays in a timescale of ~0.01 sec. These large spacecraft potentials are unacceptable.

In answer to a research call in the most-recent National Academies decadal survey to solve this problem [National Research Council, 2012], extensive computer-simulation-based studies [Delzanno et al., 2015ab, 2016; Lucco Castello et al., 2018], supported by laboratory experiments [Miars et al., 2020], have demonstrated that the operation of a plasma contactor releasing a high-density charge-neutral plasma plume before and during a beam firing will greatly mitigate the charging of the MIO spacecraft during the accelerator operation. For spacecraft-charging mitigation, the plasma-contactor technology has been successfully used in several past missions [Olsen, 1985; Gilchrist et al., 1990; Katz et al., 1994; Prech et al., 1995, 2018; Comfort et al., 1998].

The plasma contactor on the main spacecraft will be initiated prior to the accelerator operation with the ion and electron currents of the contactor exceeding the peak 10-mA electron emission of the accelerator. Theoretical analysis and computer simulations of the beam and contactor in the magnetosphere has led to a new picture of how the contactor will eliminate spacecraft charging [Delzanno et al., 2015a, 2015b; Lucco Castello et al., 2018]: rather than the contactor's Xenon-plasma plume acting as a collector of magnetospheric electrons to ensure current balance, the surface of the contactor's plasma plume will act as an emitter of Xenon ions to ensure current balance. Laboratory experiments have been performed to verify the simulation results [Miars et al., 2016, 2017, 2018a,b, 2020]. Estimates of the long-time spacecraft charging levels during electron-beam emission with the MIO parameters are plotted in Figure 2. These estimates find spacecraft Voltages of 1 kV or less [Lucco Castello et al., 2018; Borovsky et al., 2020a] as plotted in Figure 2 as a function of the radius of the plasma-contactor plume. Plume

radii of a few km are expected for MIO with the contactor fired beginning 2 seconds or so before accelerator operations.

As an operational safety measure, a mechanism is implemented in the MIO mission design wherein the accelerator cannot be operated unless current is flowing between the anode and cathode in the plasma contactor, ensuring that a plasma plume is being created.

A.1.1.2. The Electron Beam Hitting Another Spacecraft.

According to Table 1 of Appendix XX, the MIO 1-mA beam expands to a beam radius of r_{beam} = 242 m in a distance D_{full} = 150 km from the accelerator. (This calculation is for an ambient magnetospheric magnetic-field strength of 100 nT: if the magnetic field is weaker the beam expands beyond r_{beam} = 242 m.) When the beam is expanded to a large radius, its current density j_{beam} is weakened and it cannot drive strong spacecraft charging on any spacecraft that it might intercept. Three cases are examined.

For the first of three cases, consider a spacecraft in the hot, low-density magnetosphere. At r_{beam} = 242 m, the current density of the MIO beam is $j_{beam} = I_{beam}/\pi r_{beam}^2 = 5.4\times10^{-9}$ A/m^2. This is three orders of magnitude less than typical photoelectron currents off spacecraft surfaces in the Sun. It is also several orders of magnitude less than the ambient hot-electron flux to the spacecraft: for n_{plasma} = 1 cm^{-3} and T_e = 1 keV the ambient magnetospheric electron current to a spacecraft is $j_{plasma} = nev_{Te} = 2.1\times10^{-6}$ A/m^2, 400 times the current from the MIO beam.

For the second case, consider a spacecraft in the cold dense plasmasphere without a hot magnetospheric electron population. At r_{beam} = 242 m, the current density of the MIO beam is $j_{beam} = 5.4\times10^{-9}$ A/m^2. Again, this is three orders of magnitude less than typical photoelectron currents off spacecraft surfaces in the Sun. The cold-plasmaspheric electron flux to the spacecraft for n_{plasma} = 100 cm^{-3} and T_e = 1 eV is $j_{plasma} = nev_{Te} = 6.7\times10^{-6}$ A/m^2, three orders of magnitude greater than the current from the MIO beam.

For a third case, consider a low-Earth-orbit spacecraft above the atmosphere near the beamspot. As the field strength increases near the atmosphere, the beam radius decreases as the pitch-angle of the beam electrons increase. For 90^o pitch angle 1-MeV electrons in a field of 0.5 Gauss, the beam radius (= gyroradius) is r_{beam} = 102 m and the beam current density $j_{beam} = I_{beam}/\pi r_{beam}^2 = 3.1\times10^{-8}$ A/m^2. This is two orders of magnitude less than photoelectron currents on spacecraft. Calculating the ram ambient plasma flux to a low-Earth-orbiting spacecraft it is equivalent to a plasma current $j_{plasma} = nev_{ram} = 1.1\times10^{-6}$ A/m^2 for $n = 1\times10^3$ cm^{-3} and v_{ram} = 7 km/s.

In all three cases, the beam current to an accidentally intercepted spacecraft is much less than the ambient plasma particle fluxes to that spacecraft and beam-induced spacecraft charging will not be a problem.

When the beam is expanded to r_{beam} = 242 m, the 1-MeV electron flux in the beam is $F_{beam} = 3.4\times10^6$ electrons/cm^2/sec. 1-MeV electrons have a range of about 2.1 mm in aluminum. If another spacecraft was illuminated by the MIO beam, it would experience this flux F_{beam} one time for about 0.5 sec. This beam flux is about half as intense as the peak 1-MeV equatorial omnidirectional flux in the AE-8MAX radiation belt model (at about L = 4.5) [cf. Figs. 40 and 41 of Vette, 1991]. (This conclusion is the same with the AE9 model.) The total energetic-electron dose the intercepted spacecraft would receive is equivalent to a 1-second of the peak of the electron radiation belt. We do not anticipate that this would be problematic.

As an operational safety measure, the MIO accelerator beam will not be operated if another spacecraft is within D_{full} = 150 km of the main MIO spacecraft.

Note that at 150 km, the chance of hitting another spacecraft is remarkably small. At 150 km distance, the areal fraction of the sky that a 242-m radius beam intercepts is 6.5×10^{-7}.

Borovsky, J. E., Delzanno, G. L., Dors, E. E., Thomsen, M. F., Sanchez, E. R., Henderson, M. G., Marshall, R. A., Gilchrist, B. E., Miars, G., Carlsten, B. E., Storms, S. A., Holloway, M. A., Nguyen, D. (2020a). Solving the Auroral-Arc-Generator Question by Using an Electron Beam to Unambiguously Connect Critical Magnetospheric Measurements to Auroral Images. J. Atmos. Solar-Terr. Phys. 206:105310, doi.org/10.1016/j.jastp.2020.105310.

Comfort, R. H., Moore, T. E., Craven, P. D., Pollock, C. J., Mozer, F. S., Williamson, W. S. (1998). Spacecraft potential control by the Plasma Source Instrument on the Polar satellite. J. Spacecraft Rockets 35:845.

Delzanno, G. L., Borovsky, J. E., Thomsen, M. F., Moulton, J. D. (2015a). Beam experiments in the magnetosphere with plasma contactors: the electron collection and ion emission routes, J Geophys. Res. 120:3588.

Delzanno, G. L., Borovsky, J. E., Thomsen, M. F., Moulton, J. D., MacDonald, E. A. (2015b). Beam experiments in the magnetosphere: how do we get the charge off the spacecraft? J Geophys. Res. 120:3647.

Delzanno, G. L., Borovsky, J. E., Thomsen, M. F., Gilchrist, B. E., Sanchez, E. (2016). Can an electron gun solve the outstanding problem of magnetosphere-ionosphere connectivity? J Geophys. Res. 121:6769.

Gilchrist, B. E., Banks, P. M., Neubert, T., Williamson, P. R., Myers, N. B., Raitt, W. J. Sasaki, S. (1990). Electron collection enhancement arising from neutral gas jets on a charged vehicle in the ionosphere. J. Geophys. Res. 95:2469.

Katz, I., Barfield, J. N., Burch, J. L., Marshall, J. A., Gibson, W. C., Neubert, T. (1994). Interactions between the space experiments with particle plasma contactor and the ionosphere. J. Spacecraft Rockets 31:1079.

Lucco Castello, F., Delzanno, G. L., Borovsky, J. E., Miars, G., Leon, O., Gilchrist, B. E. (2018). Spacecraft-charging mitigation of a high-power electron beam emitted by a magnetospheric spacecraft: Simple theoretical model for the transient of the spacecraft potential. J. Geophys. Res. 123:6424.

Miars, G., Leon, O., Gilchrist, B. E., Delzanno, G. L., Borovsky, J. E. (2016). Electrically Isolated System Response to Rapid Charging Events Using Hollow Cathode Neutralization, 14th Spacecraft Charging Technology Conference, Noordwijk, Netherlands, April 4-8.

Miars, G, Leon, O, Gilchrist, B. E, Delzanno, G. L, Lucco Castello, F, Borovsky, J. E. (2017). Ion Emission Experiments Enabling Electron Beam Emission in Tenuous Plasmas, Active Experiments in Space, Santa Fe, NM, September 11-15.

Miars, G., Leon, O., Gilchrist, B. E., Delzanno, G. L., Lucco Castello, F. (2018a). Parametric Experiments in Mitigating Spacecraft Charging via Plasma Contactor. American Geophysical Union Fall Meeting, Washington D.C., USA, December 10-14.

Miars, G., Delzanno, G. L., Lucco Castello, F., Leon, O., Gilchrist, B. E. (2018b). Enabling Electron Beam Use in Tenuous Space Plasmas using Plasma Contactors: the Ion Emission Model, 15th Spacecraft Charging Technology Conference, Kobe, Japan, June 25-29.

Miars G, Delzanno GL, Gilchrist BE, Leon O, Lucco Castello F. (2020). Ion Emission from a Positively Biased Hollow Cathode Plasma, IEEE Trans. Plasma Sci. 48:2693.

Mott-Smith, H., Langmuir I. (1926). The theory of collectors in gaseous discharges. Phys. Rev. 28:727.

National Research Council (2013). Magnetosphere-to-ionosphere field-line tracing technology, in Solar and Space Physics: A Science for a Technological Society, pp. 333-334, Library of Congress 2013940083, National Academies Press, Washington, D. C.

Olsen, R. C. (1985). Experiments in charge control at geosynchronous orbit—ATS-5 and ATS-6. J. Spacecraft Rockets 22:254.

Prech, L., Nemecek, Z., Safrankova, J., Simunek, J., Truhlik, V., Shutte, N. M. (1995). Response of the electron energy distribution to an artificially emitted electron beam: APEX experiment. Adv. Space Res. 15(12):33.

Prech, L., Nemecek, Z., Safrankova, J., Omar, A. (2002). Actively produced high-energy electron bursts within the magnetosphere: the APEX project. Ann. Geophys. 20:1529.

Vette, J. I. (1991). The AE-8 trapped electron model environment. NSSDC/WDC-A-R&S 91-24, https://ccmc.gsfc.nasa.gov/publications/users_publication_files/Vette_1991_Ae8Ap8-ref1.pdf.

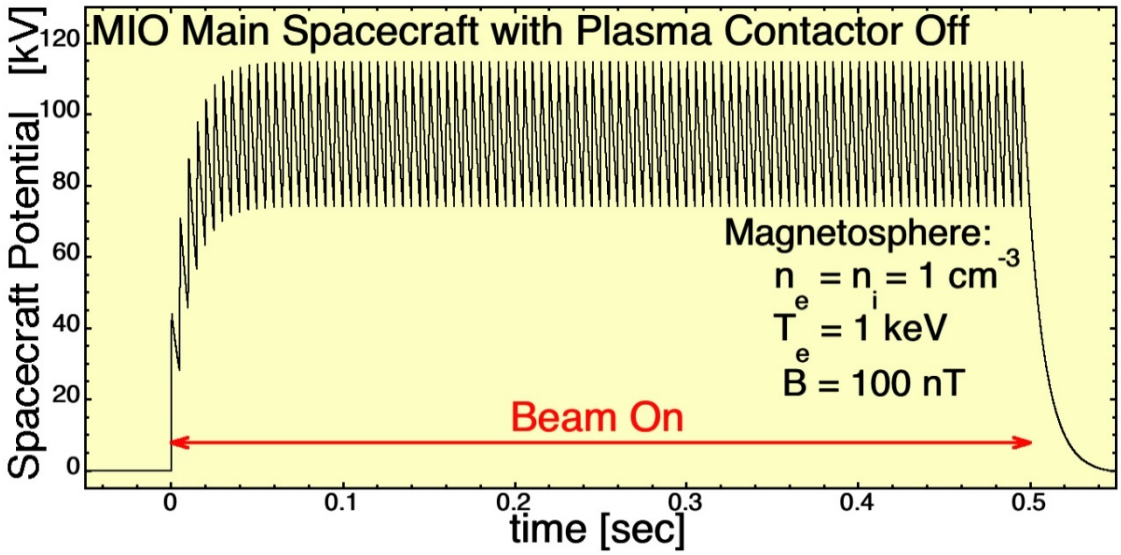

Figure 1. A calculation of the spacecraft charging of the main MIO spacecraft if a plasma contactor would not be used during the accelerator beam firing.

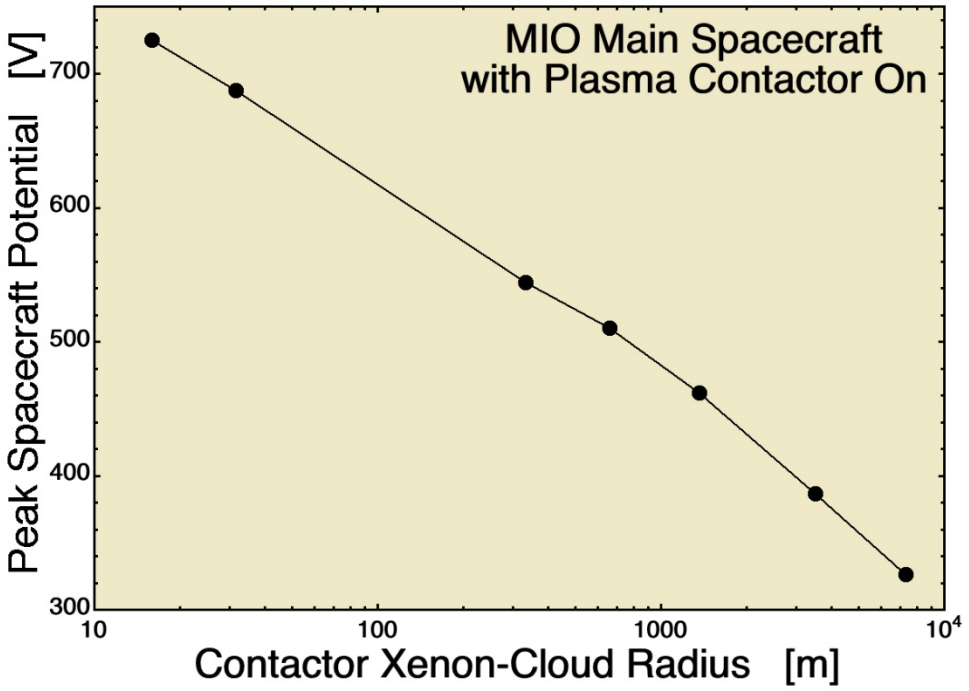

Figure 2. Peak spacecraft potential versus initial radius of the ion contactor plume prior to the emission of a 1-mA electron beam for 0.5 s.

A.1.2. Pitch-Angle Scattering of the MIO Beam Electrons by Ambient Magnetospheric Plasma Waves

Joe Borovsky and Maria Usanova

This analysis and survey of ambient-plasma-wave amplitudes in the Earth's magnetosphere concludes that ambient plasma waves are not strong enough to interfere with the propagation of the MIO 1-MeV electron beam on their flight to the atmosphere.

Naturally occurring plasma waves in the Earth's magnetosphere can produce an angular scattering of electrons. The concern for the 1-MeV MIO electron-beam mission is the amount of angular scattering the beam electrons will undergo and whether of not that angular scattering will be sufficient to deflect the beam electrons out of their pathway into the atmosphere.

The most-appropriate way to describe the amount of angular scattering by the ambient magnetospheric plasma waves is via the pitch-angle diffusion coefficient $D_{\alpha\alpha}$ for these waves, which in the literature is expressed in units of radians^2/sec. Here, the notation is that α is the electron pitch angle with respect to the local magnetic-field direction. The most-basic pitch-angle-diffusion equation describing the evolution of a distribution function of electrons $f(\alpha)$ is

$$df/dt = D_{\alpha\alpha}\, d^2f/d\alpha^2 \quad . \qquad (1)$$

Expression (1) yields an approximate spreading $\Delta\alpha$ of the pitch angles of a beam in a time t as

$$\Delta\alpha = (D_{\alpha\alpha}\, t)^{1/2} \quad . \qquad (2)$$

In order for an electron beam in the magnetosphere to effectively put its power into the atmosphere, the amount of angular scattering $\Delta\alpha$ must always be less than the local angular size of the atmospheric loss cone. In Figure 1 the angular size of the atmospheric loss cone is plotted as the two black curves for an accelerator at L=4 and at L=6.6 in a dipole magnetic field. The horizontal axis of Figure 1 is the distance along a magnetic field line from the accelerator in the equatorial plane of the dipole and the vertical axis (for the black curves) is the local angular half-width of the atmospheric loss cone at that location.

The colored curves in Figure 1 are the angular spreading $\Delta\alpha$ of an electron beam versus time (versus distance from the accelerator) as given by expression (2) owing to the scattering by various strengths of ambient plasma waves described by various values of the pitch-angle-diffusion coefficient $D_{\alpha\alpha}$. The solid curves pertain to 1-MeV electrons (with $v = 2.83\times10^{10}$ cm/s) and the dashed curves pertain to 500-keV electrons (with $v = 2.59\times10^{10}$ cm/s). If in Figure 1 a colored curve anywhere exceeds a black curve, then the pitch-angle scattering for that value of $D_{\alpha\alpha}$ is too strong for the electron beam to effectively be able to put power into the atmosphere. Figure 1 indicates that values of $D_{\alpha\alpha}$ in the range of 0.1 radian^2/s are detrimental for the operation of the MIO beam operation at L = 6.6 and values as high as 1 radian^2/s are detrimental for operation at L=4.

Five major types of magnetospheric plasma waves that can produce electron scattering are (1) whistler-mode chorus waves, (2) electromagnetic ion cyclotron (EMIC) waves, (3) whistler-mode hiss waves, (4) magnetosonic waves, and (5) electrostatic electron-cyclotron-harmonic (ECH) waves.

Whistler-mode chorus waves exist outside of the dense plasmasphere and are most intense after a substorm injection of electrons into the dipolar portion of the magnetosphere. In

Figure 2 pitch-angle-diffusion coefficients $D_{\alpha\alpha}$ for whistler-mode chorus in the nightside magnetosphere is examined. The diffusion coefficients plotted are coefficients calculated by *Horne et al.* [2013], with the matrix of $D_{\alpha\alpha}$ values supplied courtesy of Richard Horne. The top panel estimates the diffusion coefficients for whistlers when geomagnetic activity is in the normal range $2 < Kp < 3$ and the bottom panel estimates the coefficients when geomagnetic activity is high $Kp > 4$. The solid curves pertain to $D_{\alpha\alpha}$ for 1-MeV electrons and the dashed curves pertain to $D_{\alpha\alpha}$ for 600-keV electrons, which is close to 500 keV. Note that the MIO beam electrons will have pitch angles near 0^o and so the pitch-angle-diffusion coefficients $D_{\alpha\alpha}$ in the range around 0^o are of relevance. Figure 2 indicates that the pitch-angle-diffusion coefficients $D_{\alpha\alpha}$ for naturally occurring chorus waves in the magnetosphere are quite low in the vicinity of 0^o pitch angles for electron energies of relevance for the MIO beam. The chorus-wave coefficients are at least 5 orders of magnitude below the levels that would interfere with the MIO beam propagation to the atmosphere.

EMIC waves tend to be found in a wide range of radial distances, from L~2 all the way out to the magnetopause, with H^+ and He^+ band waves having different spatial distributions (e.g., Min et al., 2012). The occurrence rates of EMIC waves in the nightside inner magnetosphere are generally lowest (Figure 4). Figure 3 plots an upper limit to the amount of pitch-angle scattering by EMIC waves at L=4.5 for normal levels of geomagnetic activity. The plot is taken from Fig. 2g of *Ross et al.* [2020] where two methods are used to calculate $D_{\alpha\alpha}$ values for EMIC waves in the magnetosphere: the red Method-1 curve is the method of *Ma et al.* [2015] and the green Method-2 curve is the method of *Ross et al*. [2020]. The $D_{\alpha\alpha}$ values plotted are bounce-averaged and drift-averaged values of $D_{\alpha\alpha}$ for 2-MeV electrons. Note that values of $D_{\alpha\alpha}$ for pitch angles near 0^o are what are of interest for the MIO electron beam. The plotted values serve as upper limits for $D_{\alpha\alpha}$ for 1-MeV and 500-keV electrons in the nightside magnetosphere for two reasons. First, the $D_{\alpha\alpha}$ coefficients for 1-MeV and 500-keV are less than the coefficients for 2-MeV: this can be seen in Fig. 2a-f of *Ross et al.* [2020] and in Figs. 5 and 6 of *Kang et al.* [2015]. Second, EMIC waves occur less frequently and with lower wave power in the nightside of the magnetosphere and so $D_{\alpha\alpha}$ values in the nightside are lower than they are for drift averages of all local times: this can be seen in Fig. 3 of *Usanova et al.* [2012], in Figs. 4 and 10 of *Min et al.* [2012], and in Figs. 5-8 of *Meredith et al*. [2014]. EMIC-driven precipitation of ~MeV electrons is observed at various radial distances and local times, though the majority of the events is found on the duskside [*Qin et al*., 2018]. Further out from L=4, $D_{\alpha\alpha}$ values of 10^{-4} radian^2/s for 1-MeV and ~0 for 500 keV can be found in the literature in the dusk sector (cf. Fig. 7 of *Kang et al.* [2015]: in the midnight sector these $D_{\alpha\alpha}$ values would be less. The $D_{\alpha\alpha}$ values for EMIC waves in Figure 3 are well below values that would interfere with the MIO beam propagation to the atmosphere. Figure 4 shows EMIC occurrence distribution based on THEMIS (left) and Van Allen Probes (right) measurements. The THEMIS statistics (from *Usanova et al*. [2012]) are characterized by mostly quiet geomagnetic conditions (there were only ~20 magnetic storms with Dst<-40 nT during that period). It shows that the wave occurrence rate is rather low in the midnight sector, <1% within geosynchronous orbit (GEO), peaking at a few % beyond geosynchronous orbit. In contrast, Van Allen Probes data during an active phase of the solar

cycle shows much higher occurrence rates in the nightside, reaching ~10-20% at L~4. Due to the orbit declination, Van Allen Probes only sampled the region within geosynchronous orbit (L<6.6), so there are no data available at higher L-shells where the occurrence is expected to be higher (based on THEMIS data). The minimum resonance energy for ~80% of the wave events observed on the Van Allen Probes falls into the multi-MeV range, >2 MeV (Leslie Woodger, private communication) and would unlikely affect a 0.5-1 MeV electron beam. However, to ensure no resonance scattering by EMIC waves occur during the experiment, it is recommended to carry it out during quiet geomagnetic conditions.

Whistler-mode hiss waves in the magnetosphere are confined to the inside of the dense, cold plasmasphere, and the radius of the plasmasphere varies with time. When geomagnetic activity has been very quiet for a period of a day or two, the plasmasphere can expand out to L = 6.6 and beyond. Hiss waves are least intense on the nightside (cf. Fig. 2a of *Ma et al.* [2015]) and values of $D_{\alpha\alpha}$ for hiss that are bounce-averaged and drift-averaged yield values of $D_{\alpha\alpha}$ of 10^{-5} - 10^{-6} radian^2/s for 1-MeV to 500-keV electrons at L = 4.5 - 5 (cf. Figs. 2b and 2d of *Ma et al*. [2015]. The $D_{\alpha\alpha}$ values for hiss waves are orders of magnitude less than values that would be of concern for the operation of the MIO electron beam.

The fourth type of ambient plasma wave in the magnetosphere that can pitch-angle scatter electrons is magnetosonic waves. However, magnetosonic waves do not act on electrons with pitch angles near 0^o (see Fig. 3 of *Mourenas et al*. [2013], Fig. 3 of *Shprits et al*. [2013], Fig. 3 of *Yang et al.* [2014], and Figs. 2-9 of *Lei et al* [2017]).

The fifth type of ambient plasma wave in the magnetosphere that can pitch-angle scatter electrons is electrostatic electron-cyclotron harmonic waves (ECH). However, these waves only scatter electron with energies much lower than 500 keV (cf. Fig. 11 of *Horne et al.* [2003] or Fig. 7 of *Ni et al*. [2011]).

Horne, R. B., Thorne, R. M., Meredith, N. P., Anderson, R. R. (2003). Diffuse auroral electron scattering by electron cyclotron harmonic and whistler mode waves during an isolated substorm. J. Geophys. Res. 108:1290.

Horne, R. B., Kersten, T., Glauert, S. A., Meredith, N. P., Boscher, D., Sicard-Piet, A., Thorne, R. M., Li, W. (2013). A new diffusion matrix for whistler mode chorus waves, J. Geophys. Res. 118:6302.

Kang, S.-B., Min. K.-W., Fok, M.-C., Hwang, J., Choi, C.-R. (2015). Estimation of pitch angle diffusion rates and precipitation time scales of electrons due to EMIC waves n a realistic field model. J. Geophys. Res. 120:8529-8546.

Lei, M., Xie, L., Li, J., Pu, Z., Fu, S., Ni. B., Hua, M., Chen, L., Li, W. (2017). The radiation belt electron scattering by magnetosonic wave: Dependence on key parameters. J. Geophys. Res. 122:12338-12352.

Ma, Q., Li, W, Thorne, R. M., Kletzing, C. A., Kurth, W. S., Hospodarsky, G. B., Reeves, G. D., Henderson, M. G., Spence, H. E., Baker, D. N., Blake, J. B., Fennell, J. F., Claudepierre, S. G., Angelopoulos, V. (2015). Modeling inward diffusion and slow decay of energetic electrons in the Earth's outer radiation belt. Geophys. Res. Lett. 42:987-995.

Meredith, N. P., Horne, R. B., Kersten, T., Fraser, B. J., Grew, R. S., (2014). Global morphology and spectral properties of EMIC waves derived from CRRES observations. J. Geophys. Res. 119:5328-5342.

Min, K., Lee, J., Keika, K., Li, W. (2012). Global distribution of EMIC waves derived from THEMIS observations. J. Geophys. Res. 117:A05219.

Mourenas, D., Artemyev, A. V., Agapitov, O. V., Krasnoselskikh, V. (2013). analytical estimates of electron quasi-linear diffusion by fast magnetosonic waves. J. Geophys. Res. 118:1-17.

Ni, B., Thorne, R. M., Horne, R. B., Meredith, N. P., Shprits, Y. Y., Chen, L., Li, W. (2011). Resonant scattering of plasma sheet electrons leading to diffuse auroral precipitation: 1. Evaluation for electrostatic electron cyclotron harmonic waves. J. Geophys. Res. 116:A04218.

Qin, M., Hudson, M., Millan, R., Woodger, L., Shekhar, S. (2018). Statistical investigation of the efficiency of EMIC waves in precipitating relativistic electrons. Journal of Geophysical Research: Space Physics, 123:6223-6230. https://doi.org/10.1029/2018JA025419.

Ross, J. P. J., Glauert, S. A., Horne, R. B., Watt, C. E., Meredith, N. P., Woodfield, E. E. (2020). A new approach to constructing models of electron diffusion by EMIC waves in the radiation belts. Geophys. Res. Lett. 47:e2020GL088976.

Shprits, Y. Y., Runov, A., Ni, B. (2013). Gyro-resonant scattering of radiation belt electrons during the solar minimum by fast magnetosonic waves. J. Geophys. Res. 118:648-652.

Usanova, M. E., Mann, I. R., Bortnik, J., Shao, L., Angelopoulos, V. (2012). THEMIS observations of electromagnetic ion cyclotron wave occurrence: Dependence on AE, SYMH, and solar wind dynamic pressure. J. Geophys. Res. 117:A10218.

Yang, C., Zhang, L., He., Y., Liu, S., Zhou, Q. (2014). Radiation belt electron acceleration induced by gyroresonant interaction with magnetosonic waves. Astrophys. Space Sci. 353:389-394.

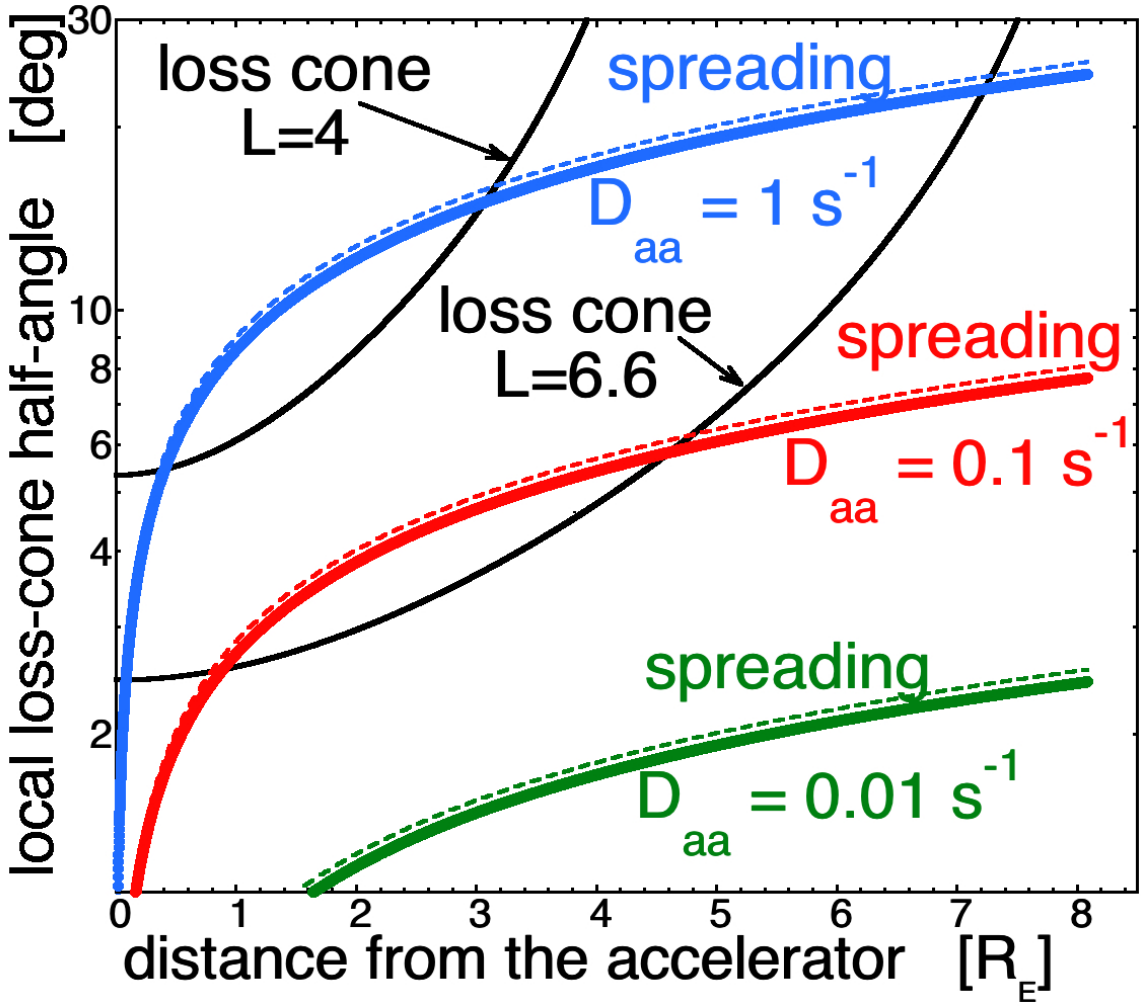

Figure 1. The black curves are the local angular half-width of the atmospheric loss cone plotted as functions of the distance along the field line from the dipole equator. The colored curves are the spreading angle of the electron beam owing to pitch-angle scattering by ambient plasma waves for given values of the pitch-angle-diffusion coefficient $D_{\alpha\alpha}$.

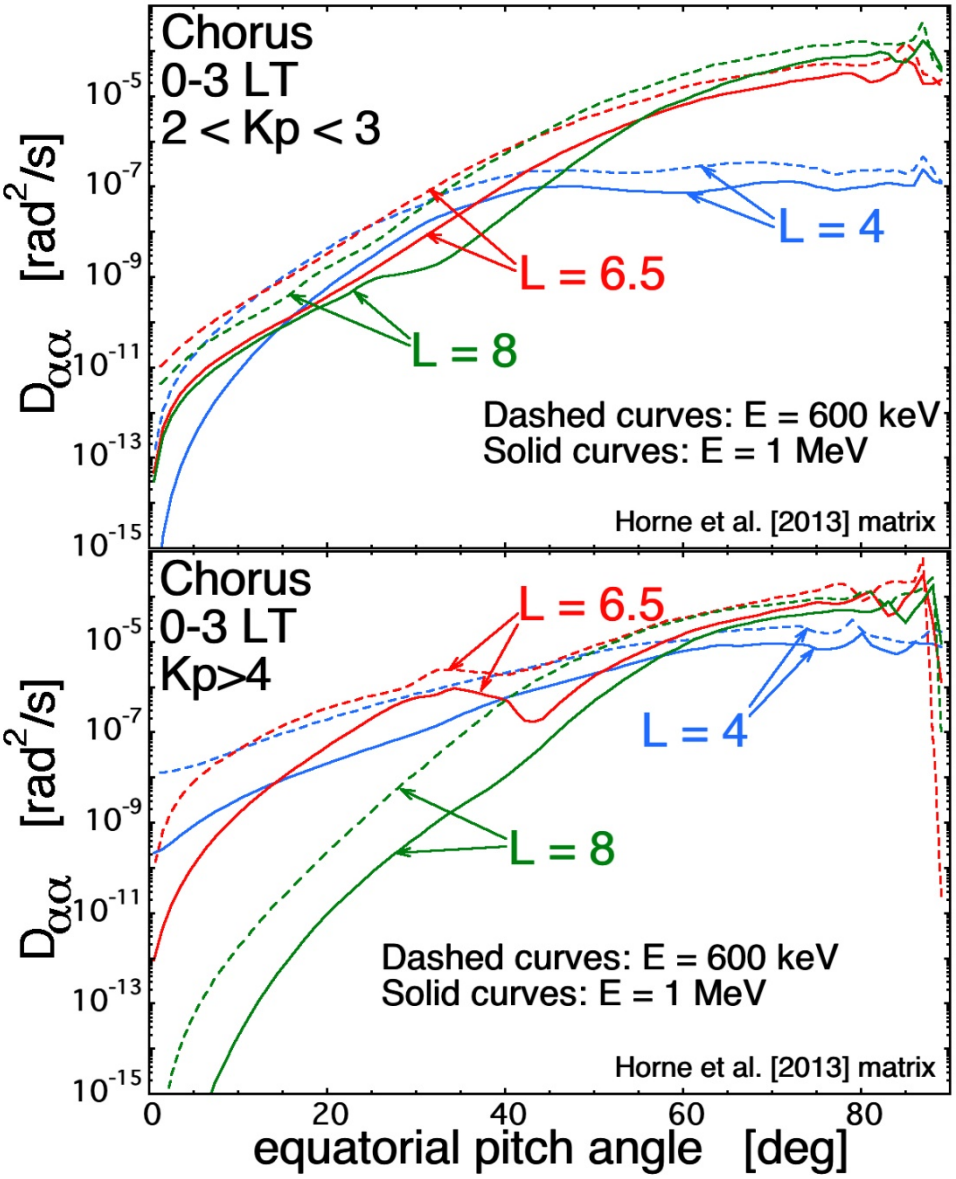

Figure 2. For ambient whistler-mode chorus waves, estimated pitch-angle-diffusion coefficients are plotted for 1-MeV electrons (solid curves) and for 500-keV electrons (dashed curves). The blue curves pertain to L=4 on the nightside, the red curves pertain to L=6.5 on the nightside, and the green curves pertain to L=8 on the nightside. The top panel is for normal levels of geomagnetic activity and the bottom panel is for strong levels of activity. The plotted $D_{\alpha\alpha}$ values are from the Horne et al. [2013] matrix.

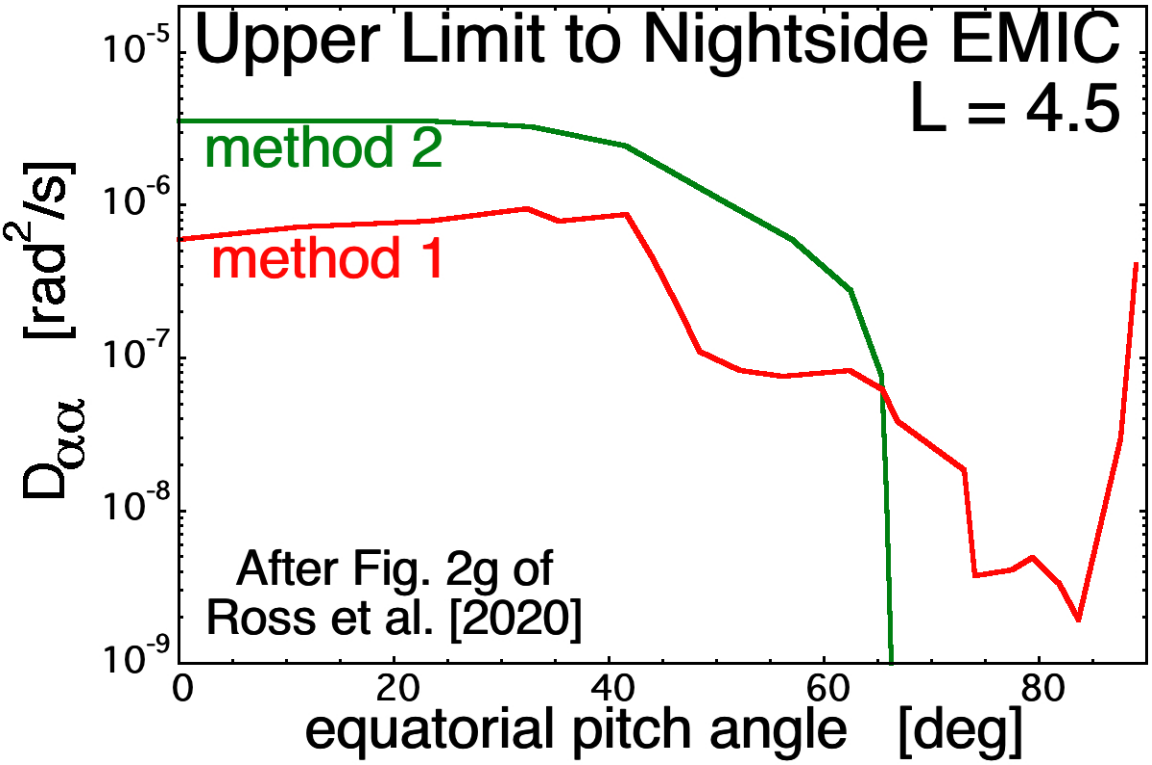

Figure 3. For EMIC waves in the nightside magnetosphere, upper limits for the values of the pitch-angle-diffusion coefficients are plotted (see text). The plot is after Fig. 2g of Ross et al. [2020].

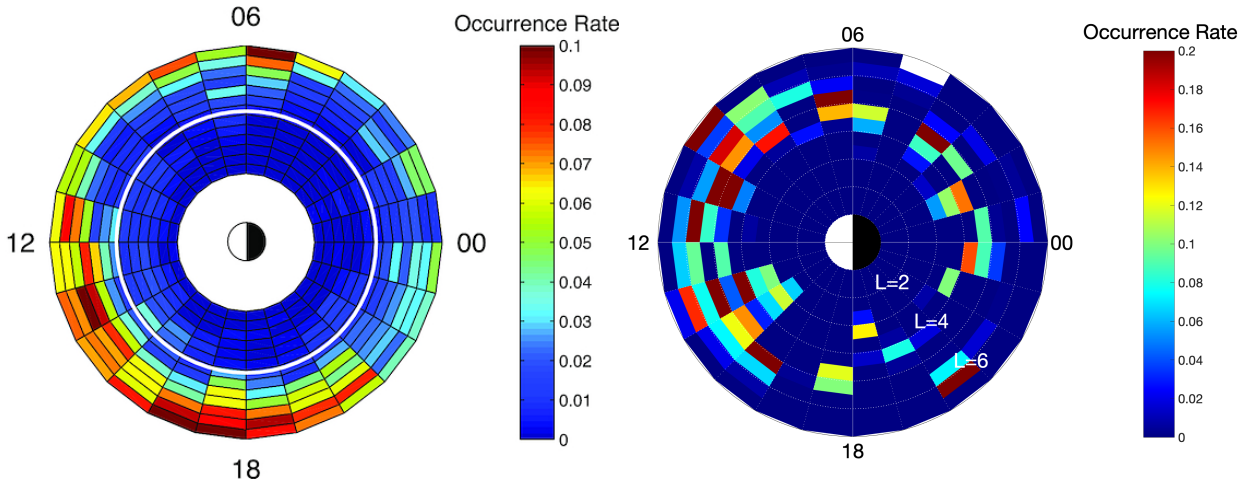

Figure 4. EMIC wave occurrence in the magnetosphere from THEMIS, L=3-10 (left) and Van Allen Probes, L=1.5-6.5 (right) measurements. THEMIS data (2007-2011) is representative of quiet geomagnetic conditions (Usanova et al., 2012), while Van Allen Probes samples a different phase of solar cycle (2012-2019) and active conditions (Usanova et al., in prep).

A.1.3. Beam-Stability Calculations

Vadim Roytershteyn, Gian Luca Delzanno, and Joe Borovsky

Theoretical analysis accompanied by particle-in-cell plasma simulations find that the 1-MeV MIO electron beam will not be disrupted by plasma-wave instabilities as it propagates from the accelerator to the atmosphere through the magnetospheric plasma.

A. Preliminary Considerations

In general, an energetic electron beam propagating through cold background plasma along a background magnetic field may be expected to become unstable. The simplest case to analyze is that of an infinite non-relativistic beam with small number density n_b compared to the background plasma number density n_o and with zero energy spread. Under such conditions, the beam is unstable to the electrostatic electron-electron two-stream instability with the growth rate $\mathrm{Im}(\omega)\sim\left({}^{n_b}/_{n_0}\right)^{1/3}\omega_{pe}$ and the most unstable wavenumbers corresponding to $kV_b\sim\omega_{pe}$ where V_b if the beam speed and ω_{pe} is the plasma frequency. Finite parallel energy spread of the beam is a stabilizing effect. If it is large enough, the nature of the instability changes from two-stream to kinetic with the growth rate $\mathrm{Im}(\omega)\sim\left({}^{n_b}/_{n_0}\right)\left({}^{V_b}/_{\Delta v_b}\right)^2\omega_{pe}$, where Δv_b is a typical velocity dispersion of the beam (e.g. Melrose, 1986). In all cases, the growth rate peaks for parallel (with respect to the beam velocity and magnetic field) orientation of the wavevector, but remains significant for a range of angles.

The finite size of the artificially created beams is an important factor affecting beam stability (e.g. Frieman *et al.,* 1962; Bogdankevich and Rukhadze, 1971; Galvez and Borovsky, 1988). To get useful insights into the influence of relativistic effects and of the size of the beam, we first consider axisymmetric electrostatic perturbations in the framework of the cold relativistic plasma theory. Following the (non-relativistic) analysis of Galvez and Borovsky (1988), we consider a cylindrical beam with radius r_b and with step-function density and velocity profile in a strong background magnetic field. Then the Poisson equation within the beam ($r \le r_b$) is

$$\frac{1}{r}\frac{d}{dr}\left(r\frac{d}{dr}\phi\right) - k^2\left(1-\frac{\omega_{pe}^2}{\gamma^3(\omega-kV)^2}\frac{n_b}{n_0}-\frac{\omega_{pe}^2}{\omega^2}\right)\phi = 0$$

where $\gamma = (1-(V_b/c)^2)^{-1/2}$ is the relativistic factor. The solution inside the beam that is finite at $r = 0$ is $\phi = C_1 I_o\left(k\epsilon_{in}^{1/2}r\right)$. Outside of the beam

$$\frac{1}{r}\frac{d}{dr}\left(r\frac{d}{dr}\phi\right) - k^2\left(1-\frac{\omega_{pe}^2}{\omega^2}\right)\phi = 0$$

where I_0, I_1, K_0, and K_1 are modified Bessel functions. The solution outside of the beam that decays at large r is $\phi = C_2 K_o\left(k\epsilon_{out}^{1/2}r\right)$. Here ϵ_{in} and ϵ_{out} are the uniform plasma dielectric functions inside and outside the beam respectively (large brackets in the Poisson equation). Matching the solutions and their derivatives at $r = r_b$, we obtain the relativistic analog of the dispersion relation presented in (Galvez and Borovsky, 1988)

$$\epsilon_{out}^{1/2} I_o\left(k\epsilon_{in}^{1/2}r_b\right)K_1\left(k\epsilon_{out}^{1/2}r_b\right) + \epsilon_{in}^{1/2} I_1\left(k\epsilon_{in}^{1/2}r_b\right)K_0\left(k\epsilon_{out}^{1/2}r_b\right) = 0$$

It is immediately apparent from the above equations that relativistic effects have a stabilizing influence on the longitudinal electrostatic instability. An example of the solution of this

dispersion relation is shown in Figure A-1 for two beam energies (E_b = 1 MeV at I_b = 10 mA and E_b = 0.5 MeV at I_b = 20 mA). An interesting feature of these solutions is that the growth rate approaches a finite constant for small beam radii, due to increasing beam density $n_b \propto 1/r_b^2$.

For the 10-mA 1-MeV beam, $\mathrm{Im}(\omega) \approx 10^{-4}\ \omega_{pe}$, where ω_{pe} is the electron plasma frequency of the background magnetospheric plasma. This gives a growth time for instability of $\tau_{growth} = 1/\mathrm{Im}(\omega) \approx 10^4\ \omega_{pe}$. Approximating a growth distance as $\lambda_{growth} = V_b\tau_{growth} = 10^4 V_b/\omega_{pe}$. For a n_o = 1 cm-3 background plasma $\omega_{pe}^{-1} = 1.8\times10^{-5}$ sec and with $V_b = 2.83\times10^{10}$ cm/s this gives a growth length $\lambda_{growth} \approx 5.0\times10^9$ cm = 7.8 R_E. With several growth lengths needed for an instability to grow out of the noise, the 1-MeV beam is safely stable on its flight from the spacecraft to the atmosphere.

Two factors will reduce the strength of the instability. First, there is an energy spread to the 1-MeV beam. In the reference frame of the background plasma, this energy spread produces a spread in the effective electron mass γm_e in the beam, which de-tunes the plasma frequency of the beam as seen from the frame of the magnetosphere, lessening the strength of any beam oscillations in the instability. Second, the beam is intermittent at 200 Hz as pointed out in Appendix XX, with intervals of 10-mA beam interspaced with intervals of no beam to produce a time-averaged beam current of 1 mA.

In addition to purely longitudinal instabilities, the beam may be unstable to a variety of other modes, including non-axisymmetric instabilities. Of particular concern are long-wavelength kink instability, which may lead to disruption of the beam. Fully kinetic, nonlinear particle-in-cell (PIC) simulations were used to study the development and saturation of such modes.

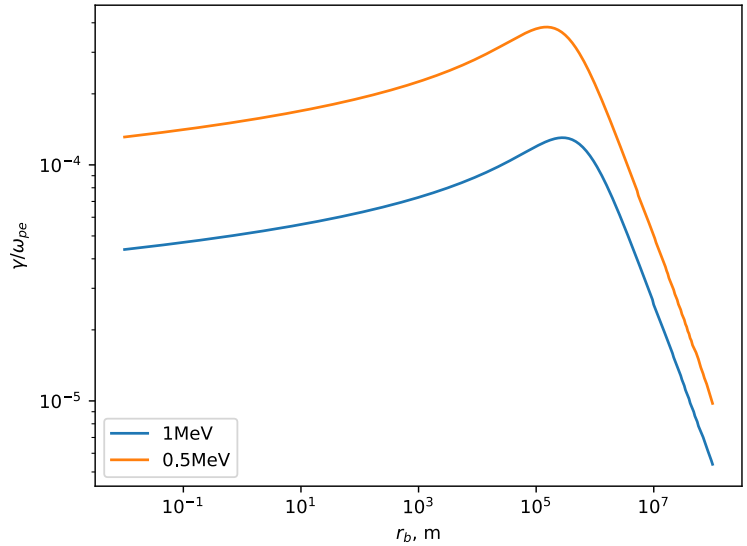

Figure A-1: Instability growth rate obtained by solving a cold relativistic dispersion relation for parallel electrostatic perturbations at two beam energies $E_b = 0.5MeV$ and $E_b = 1MeV$. The corresponding current density is $I_b = 0.02$A and $I_b = 0.01$A respectively.

B. PIC Simulations

Simulation setup: The PIC simulations solve relativistic, electromagnetic Vlasov-Maxwell system. The simulations were performed using the relativistic, fully kinetic PIC code VPIC (Bowers *et al.*, 2008). The analysis presented here focuses on the stability of the beam at time scales after the beam has expanded from the initially small radius r_b of the order of one cm to a radius of the order of 10s to 100s of meters (see Table A-1) and has become uniform. The 3D simulations utilize periodic boundary conditions along the beam to enable long-time simulations and use conducting boundary in the perpendicular directions. (The influence of the boundary conditions is discussed below.) The simulations are performed for a range of initial r_b and at two beam energies, see Table A-1 for a summary of the parameters. For all cases, we assumed the following parameters of the background plasma $T_e = T_i = 1$ keV, $n_o = 0.5$ cm^{-3}, and the background magnetic field $B_0 = 10^{-3}$G = 100 nT. The background plasma and the beam particles are represented by 100 particles per cell per species.

Table A-1: Parameters of the PIC simulations

Simulation id	Beam energy E_b, MeV	Beam current I_b, A	Beam radius r_b, m	$\Delta u/U_0$, %	Domain Length $L_z\omega_{pe}/V_b$	Transverse size, r_b	Resolution (cells)
A	1	0.01	50	0	7	20	100 x 100 x 4992
B	1	0.01	50	1	7	20	100 x 100 x 4992
C	1	0.01	300	0	50	40	200 x 200 x 5920
D	1	0.01	300	1	50	40	200 x 200 x 5920
E	1	0.01	1000	0	100	40	200 x 200 x 3552
F	1	0.01	1000	1	100	40	200 x 200 x 3552
G	0.5	0.02	50	1	2π	20	100 x 100 x 4096

Results: None of the simulations performed in this study exhibited development of significant macroscopic instabilities. While small-scale instabilities were present, they saturated at relatively small amplitudes and did not lead to a disruption of the beam. This is consistent with the results summarized in the previous section, which suggest that typical growth rates are relatively small. In order to quantify the influence of the weak fluctuations that were present, we focus on quantifying the distribution of pitch angles in the simulations. The results are summarized in a set of figures below. We note that wider beams tend to be more unstable, but the typical spread of pitch angles observed in the simulations does not exceed 0.5 degrees.

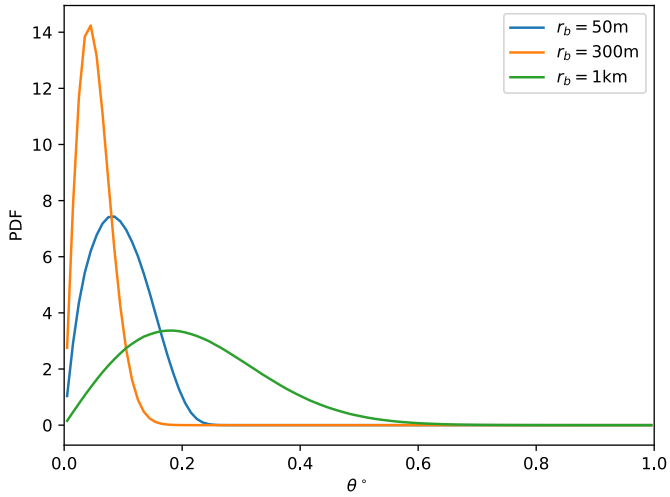

Figure A-2: Distribution of beam pitch-angles in 3 simulations with $E_b = 1$MeV (cases B, D, and F from *Table A-1*). Comparison is performed at time $t\omega_{pe} \approx 2150$.

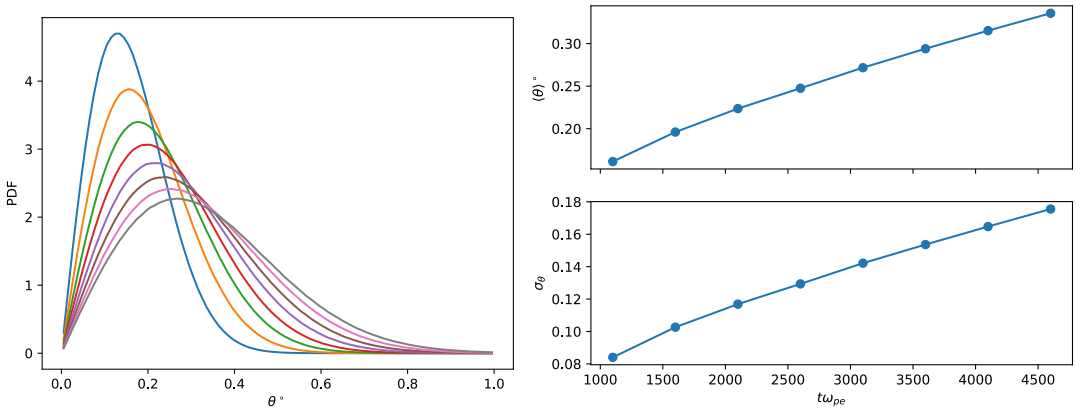

Figure A-3: Left: time evolution of the pitch-angle distribution for the case with $E_b = 1$MeV and $r_b = 1$km (*case F). Right two panels: time evolution of the mean and standard deviation of the pitch-angle in this simulation. The time instances for the distributions are marked by dots in the right panels.*

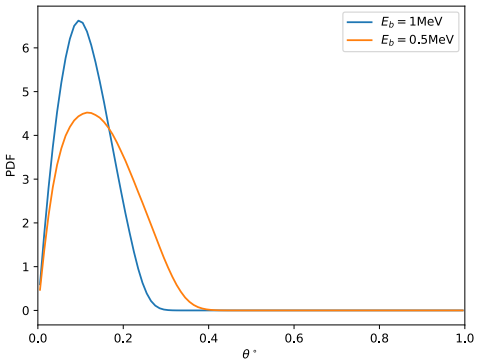

Figure A-4: distribution of the beam pitch-angles in two simulations with $r_b = 50$m *and* $E_b = 1$MeV *(case B, at* $t\omega_{pe} \approx 2900$*) and* $E_b = 0.5$MeV *(case G, at* $t\omega_{pe} \approx 2850$*).*

Limitations of the analysis: It is important to mention potential limitation of the present analysis. First, we use conducting boundary conditions in the transverse directions. The image

charges and induced currents may have stabilizing influence on various instabilities (particularly of kink type), so it would be useful to repeat at least some of these calculations with open boundary conditions. In the present calculation, this problem is mitigated to some degree by putting the boundary sufficiently far away (at least $10r_b$ from the beam center). Second, due to significant computation cost of the simulations, we used relatively coarse resolution (5-10 grid cells per beam radius) in the simulation. Potentially, this may have an influence on the early development of an instability, if the corresponding eigenfunction has sharp features in radius. Convergence studies are being performed to check the influence of the resolution and these will be published. In all cases the simulation box has a finite length and it admits only instabilities that fit into the box (i.e. have wavelengths less than or equal to the box-length L). Box lengths were used that were large enough to enable reasonable turnover speed for simulations, but still resolved what were anticipated to be unstable wavelengths. Finally, the duration of the simulations is limited, so that we are addressing beam stability over a relatively short interval of time. Under the nominal conditions considered in this study, the time interval of $\Delta T = 10^3 \omega_{pe}^{-1}$ corresponds to propagation over approximately $1R_E$.

Bogdankevich, L. S., and Rukhadze, A "Stability Of Relativistic Electron Beams In A Plasma And The Problem Of Critical Currents." Soviet Physics Uspekhi 14, 163–79 (1971) https://doi.org/10.1070/PU1971v014n02ABEH004456.

Bowers, K J, B J Albright, L Yin, B Bergen, and T J T Kwan. "Ultrahigh Performance Three-Dimensional Electromagnetic Relativistic Kinetic Plasma Simulation." Physics of Plasmas 15, 055703 (2008) https://doi.org/10.1063/1.2840133.

Frieman, E. A., M. L. Goldberger, K. M. Watson, S. Weinberg, and M. N. Rosenbluth. "Two-Stream Instability in Finite Beams." Physics of Fluids 5, 196 (1962). https://doi.org/10.1063/1.1706596.

Galvez, M. and Borovsky, J. "The Electrostatic Two-Stream Instability Driven by Slab-Shaped and Cylindrical Beams Injected into Plasmas." Physics of Fluids 31, 857 (1988) https://doi.org/10.1063/1.866767.

Melrose D B, "Instabilities in Space and Laboratory Plasmas", New York: Cambridge University Press, 1986.

A.1.4. Evolution of the MIO Linac Pulsed Beam: Filling-in Distance, Beam Angular Spread, and Beam Radius

Joe Borovsky, Vadim Roytershteyn, Gian Luca Delzanno

On a fine timescale, the electron beam of the 5.1-GHz MIO linear accelerator is comprised of electron bunches separated in time by 196 ps = 1.96×10^{-10} s = 1/(5.1 GHz) as they exit the accelerator. Each electron bunch is about 4 ps in duration. Because the charge is highly concentrated in a single bunch, each electron bunch will electrostatically expand rapidly, with the electrons picking up a transverse velocity that results in an angular spread to the beam. That transverse velocity is governed by the total charge Q_{bunch} in a bunch and by the size and shape of the bunch. That transverse velocity creates an angular spread to the beam and determines the beam radius as it propagates away from the accelerator.

For simplicity, the expansion calculation will be performed in the reference frame moving with the beam and then the results will be relativistically transformed to the frame of the accelerator. Quantities measured in the beam reference frame will have a subscript "-b" and quantities in the frame of the accelerator will have a subscript "-a".

The total charge Q_{bunch} of a electron bunch is given by the average beam current of the accelerator I_{beam} times one second divided by the number of electron bunches per second. If the accelerator were to operate continuously during a "beam-on" interval, then there would be (1 sec)/(196 ps) = 5.1×10^{9} bunches per second. But during a "beam-on" interval the accelerator switches on and off at 200 Hz with a 10% duty cycle, so there is N = 5.1×10^{8} bunches per second. Hence, the charge in an electron bunch is $Q_{bunch} = I_{beam}$ (1s)/N. This value is the same in both reference frames. The value of Q_{bunch} appears in table 1, it is 1.2×10^{7} electrons.

In the reference frame of the accelerator the electron bunches are L_a = (196 ps) v_{beam} apart, where $v_{beam} = 2.83\times10^{10}$ cm/s is the velocity of the beam out of the accelerator. The structure of the moving beam is Lorentz contracted as seen by the accelerator: in the frame moving with the beam the spacing of the electron bunches is $L_b = \gamma L_a$, where $\gamma = 2.96$ is the relativistic factor of the beam, so L_b is about 3 times the spacing as seen in the accelerator frame. Values of L_a and L_b are entered into Table 1.

In the reference frame of the accelerator the electron bunches are approximately spherical with radius $r_{bunch} \sim 0.1$ cm. In the reference frame moving with the beam an electron bunch is elongated from a sphere by a factor of $\gamma \sim 3$. For a simple electrostatic calculation in the frame moving with the beam we will approximate the charge bunch with 3 spheres of charge, as sketched in Figure 1. For $\gamma\sim3$ (1 MeV) we will separate the centers of the three spheres by distances of $2r_{bunch}$ (as denoted in Figure 1). The total charge is Q_{bunch} and a fraction F is offloaded from the center sphere to the front and back spheres. At the edge of the center sphere (marked "x" in Figure 1) the electrostatic potential in the beam frame is the sum of the electrostatic potentials for the three spheres: $\phi_{bunch\text{-}b} = [(1\text{-}F)Q_{bunch}/r_{bunch}] + 2[FQ_{bunch}/(2\,5^{1/2}\,r_{bunch})] = (Q_{bunch}/r_{bunch})[1 - 0.5528F]$. The final transverse velocity that an electron will gain in being accelerated from the point "x" transverse to the beam (arrow in Figure 1) is, by energy conservation in the frame of the beam, $v_{exp\text{-}b} = (2e\phi_{bunch\text{-}b}/m)^{1/2} = (2eQ_{bunch}/mr_o)^{1/2}\,[1 - 0.5528F]^{1/2}$, where e and m are the charge and mass of an electron. As the fraction F increases from 0 the transverse velocity will decrease. In approximating the elongated pulse by three spheres of charge F=0 is not enough spreading (where the factor $[1\text{-}0.5528F]^{1/2} = 1$) and F=1 is too much spreading (where the factor $[1\text{-}0.5528F]^{1/2} = 0.669$). As a

compromise, F = 0.5 is taken, where the factor is $[1\text{-}0.5528F]^{1/2} = 0.851$. Taking $r_{bunch} = 0.1$ cm, $\phi_{bunch\text{-}b}$ and $v_{exp\text{-}b}$ are calculated and entered into Table 1.

Owing to (1) the electrostatic expansion of the charge pulses and (2) the inherent energy spread of the accelerator, the charge pulses will eventually fill-in to make a continuous beam. We will calculate fill-in times for both processes. The time (in the beam frame) required for the beam to fill in and appear to be continuous rather than bunched owing to the electrostatic expansion of the bunches is about $\tau_{fill\text{-}b} \sim L_b/v_{exp\text{-}b}$. In the accelerator frame this filling in time is $\tau_{fill\text{-}a} = \gamma\tau_{fill\text{-}b} = \gamma L_b/v_{exp\text{-}b}$. These values are entered into Table 1. This filling-in time by electrostatic expansion is similar to the filling-in time associated with the energy spread of the accelerator beam, which is ~3% (in the accelerator frame, of course). A 3% spread of the accelerator beam energy corresponds to a velocity spread Δv_{-a} (in the accelerator frame) of $\Delta v_{-a} = 7.01\times10^{7}$ cm/sec for a 1-MeV beam. This value is entered into Table 1. This gives a fill-in time (in the accelerator frame) of $t_{fill\text{-}a} = L_a/\Delta v_{-a} = 8.27\times10^{-8}$ sec. This is entered into Table 1. In the time $t_{fill\text{-}a}$, the beam moves a distance $d_a = v_{beam}t_{fill\text{-}a}$ in the frame of the accelerator. This is the filling-in distance from the accelerator where the beam becomes continuous. Using the minimum values of $t_{fill\text{-}a}$ in Table 1, the resulting value of d_a is entered into Table 1: the beam pulses blend together to make a continuous beam at about 65 meters from the accelerator.

We are interested in the transverse (to the beam) expansion velocity in the frame of the accelerator: this will inform us about the angular spread of the beam. In the frame of the beam the expansion velocity for electrons at the outer edge of the electron bunch is $v_{trans\text{-}b} = \Delta x_b/\Delta t_b$ and in the frame of the accelerator this expansion velocity is $v_{trans\text{-}a} = \Delta x_a/\Delta t_a$. The transverse distance Δx is the same in both frames ($\Delta x_a = \Delta x_b$), but the time interval Δt is not. By time dilation, $\Delta t_a = \gamma\Delta t_b$. Hence, $v_{trans\text{-}a} = v_{trans\text{-}b}/\gamma = v_{exp\text{-}b}/\gamma$. The value of $v_{trans\text{-}a}$ is entered into Table 1.

With the transverse velocity $v_{trans\text{-}a}$ in the accelerator frame, and the beam speed v_{beam}, the angular spread $\theta_{spread\text{-}a}$ of the beam as seen in the frame of the accelerator is calculated as $\theta_{spread\text{-}a} = v_{trans\text{-}a}/v_{beam}$ (in radians). The value of $\theta_{spread\text{-}a}$ is calculated and entered into Table 1, converted into degrees. The beam angular spread caused by electrostatic expansion is 0.146^{o} half angle.

Note that the expansion of the electron bunch is a spherically symmetric expansion in the reference frame of the beam with the expansion along the beam and transverse to be beam being the same. This is not so in the frame of the accelerator where the expansion is stronger transverse to the beam than it is along the beam. In a filling-in time, the electron bunch expands a distance of L_a along the beam and a distance of $L_b = \gamma L_a$ transverse to the beam. The expanding spherical electron clouds in the beam frame are Lorentz contracted into flattened clouds in the accelerator frame.

The transverse velocity gained by electrons as the electron bunches expand will determine the beam radius away from the accelerator. This is sketched in Figure 2. Four electron orbits in the Earth's magnetic field are shown as the black curves. They move a distance of two electron gyroradii away from the beam before the Earth's field brings them back to the beam. Hence, the outer radius of the electron beam r_{beam} (dashed red curve) will be two electron gyroradii in size. Calculated in the frame of the accelerator, that is $r_{beam} = 2\gamma v_{trans\text{-}a}mc/eB$, where B is the Earth's magnetic field. For a 100 nT = 1×10^{-3} gauss field, the beam outer radius is calculated and entered into Table 1. For 100 nT the beam radius is 142 m.

The beam full-expansion timescale τ_{full} is one-half of a beam-electron gyrotime in the ambient magnetic field B, which is $\tau_{full} = \pi\gamma mc/eB$ and the distance D_{full} the beam travels before full expansion is $D_{full} = v_{beam}\tau_{full} = v_{beam}\pi\gamma mc/eB$. The value of D_{full} is calculated and entered into Table 1. It takes 150 km for the beam to reach its full radius.

Idealized beam-radius calculations using particle-orbits [e.g. Fig. B1 of Borovsky, 2002] or using a beam "envelope equation" [e.g. Fig. 7 of Sanchez et al., 2019 or Fig. 10 of Powis et al., 2019] predict that the electrons of an expanding beam will re-assemble into a small-radius beam after a time of one full electron gyroperiod. However, for MIO this idealization is spoiled by at least two factors. (1) There is a ~3% energy spread to the beam, which relativistically results in a ~2% spread in the electron gyroperiods in the beam ruining the simultaneity of the electrons re-converging to small radius. (2) The energy spread in the beam results in a velocity spread to the beam, that produces a spread in the transverse-to-**B** curvature drift speed, spreading the beam in the transverse-to-**B** direction. For a 1-MeV beam at the dipole equator at L=6.6, this curvature-drift spreading is about 23 meters per electron gyroperiod.

During a "beam-on" interval, the MIO 1-MeV beam is pulsed at 200 Hz with a 10% duty cycle. Each pulse has 10 mA of current. Each pulse duration is 0.5 msec and the pulses are 4.5 msec apart. Exiting the accelerator a 0.5-msec pulse is 150-km long and the gap between pulses is 1350 km. A 3% energy spread of a 1-MeV beam corresponds to a velocity spread of 7×10^7 cm/sec in the frame of the accelerator. The flight time of the beam to the atmosphere is in the range of 0.1 - 0.2 sec, depending on where MIO is in its orbit. In that time the velocity spread of the beam only fills in 70 - 140 km of the 1350-km gap. Hence, the gaps exist all the way to the atmosphere. Spreading in both the forward and backward directions, the beam spatial pulses lengthen from 150 km near the accelerator to about 300 - 450 km or so near the atmosphere, where the current decreases from 10 mA near the accelerator to about 3.5 - 5 mA near the atmosphere. The beam pulses hit the atmosphere with a 200-Hz cadence. A 0.5-sec 1-mA "beam-on" interval will be comprised of 100 pulses, each about 1-msec long, and each with a current of about 5 mA.

The average number density of the beam n_{beam} is given the number of electrons N per unit length in the beam, which is $N/L = I_{beam}/ev_{beam}$, and the cross-sectional area of the beam, which is πr_{beam}^2. The number density is $n_{beam} = (N/L)/(\pi r_{beam}^2) = I_{beam}/ev_{beam}\pi r_{beam}^2$. For a 10-mA pulse of beam in the magnetosphere, the value calculated for the beam number density is entered into Table 1.

Remember that the shape and size of the electron bunches exiting the accelerator matters for the calculations. If the bunches are elongated in the direction of the beam, the expansions are slower, the filling-in distance is longer, the transverse velocities are less, the beam angular spread is less, and the beam radius is smaller.

Borovsky, J. E., (2002). The Magnetosphere-Ionosphere Observatory (MIO). Los Alamos National Laboratory https://www.lanl.gov/csse/MIOwriteup.pdf.

Powis, A. T., Porazik, P., Greklek-Mckeon, M., Amin, K., Shaw, D., Kaganovich, I. D., Johnson, J., Sanchez, E. R. (2019). Evolution of a relativistic electron beam for tracing magnetospheric field lines. Front. Astron. Space Phys. 6:69.

Sanchez, E. R., Powis, A. T., Kagonovich, I. D., Marshall, R., Porazik, P., Johnson, J., Grekiek-Mckeon, M., Amin, K. S., Shaw, D. Nicolls, M. (2019). Relativistic particle beams as a resource to solve outstanding problems in space physics. Front. Astron. Space Sci. 6:71.

Table 1. Parameters for the calculations for the MIO 1-MeV 1-kWatt average beam.

		1 MeV 1 kWatt
I_{beam}	average beam-on current	0.001 Amp
v_{beam}	beam speed	2.83×10^{10} cm/s
γ	relativistic factor of beam	2.96
Θ_{bunch}	total charge in an electron bunch	1.96×10^{-12} Coul 5.88×10^{-3} statC
L_a	spacing between electron bunches (in accelerator frame)	5.80 cm
L_b	spacing between electron bunches (in beam frame)	16.4 cm
r_o	radius of charge bunch	0.1 cm
$\phi_{bunch-b}$	electrical potential at bunch edge (beam frame)	12.7 V
v_{exp-b}	electron bunch expansion velocity (beam frame)	2.12×10^{8} cm/s
τ_{fill-a}	electrostatic filling-in time (accelerator frame)	2.19×10^{-7} sec
Δv_{exp-b}	accelerator velocity spread (accelerator frame)	7.01×10^{7} cm/s
τ_{fill-a}	Δv filling-in time (accelerator frame)	8.27×10^{-8} sec
d_a	filling-in distance (accelerator frame)	6.49×10^{3} cm
$v_{trans-a}$	transverse electron velocity (accelerator frame)	7.49×10^{7} cm/s
$\theta_{spread-a}$	beam angular spread (accelerator frame)	0.146 degree
ρ_{beam}	beam radius (B = 100 nT)	242 m
D_{full}	distance to full expansion of beam (accelerator frame)	150 km
N_{beam}	beam number density (accelerator frame)	1.15×10^{-4} cm^{-3}

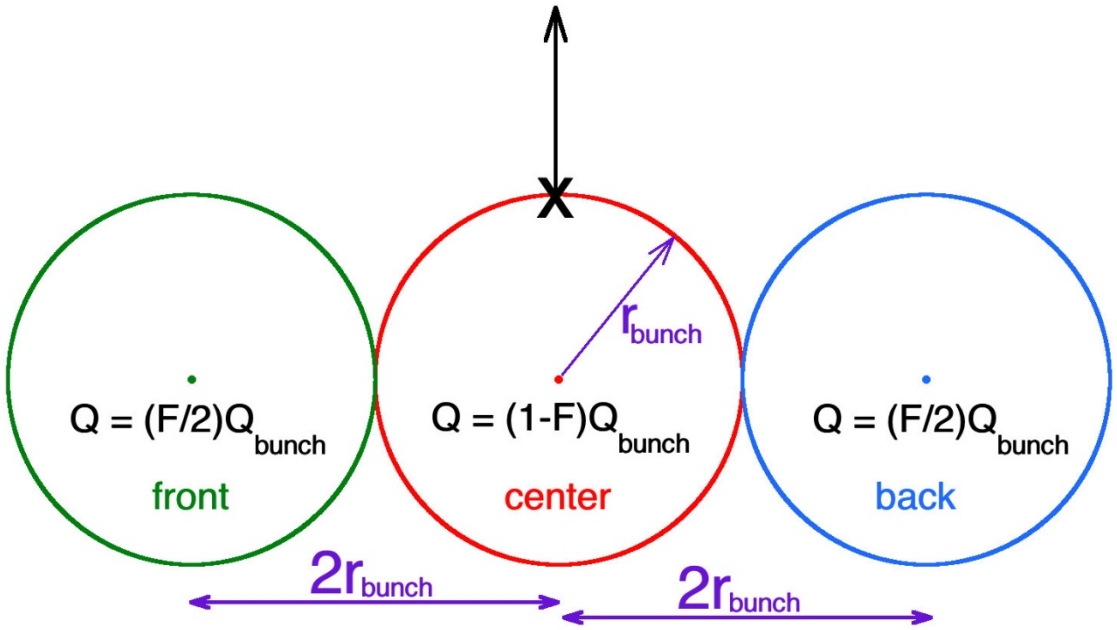

Figure 1. A sketch of the calculation of the electron-bunch transverse expansion velocity in the reference frame moving with the beam. The elongated charge bunch is approximated by three spheres of charge.

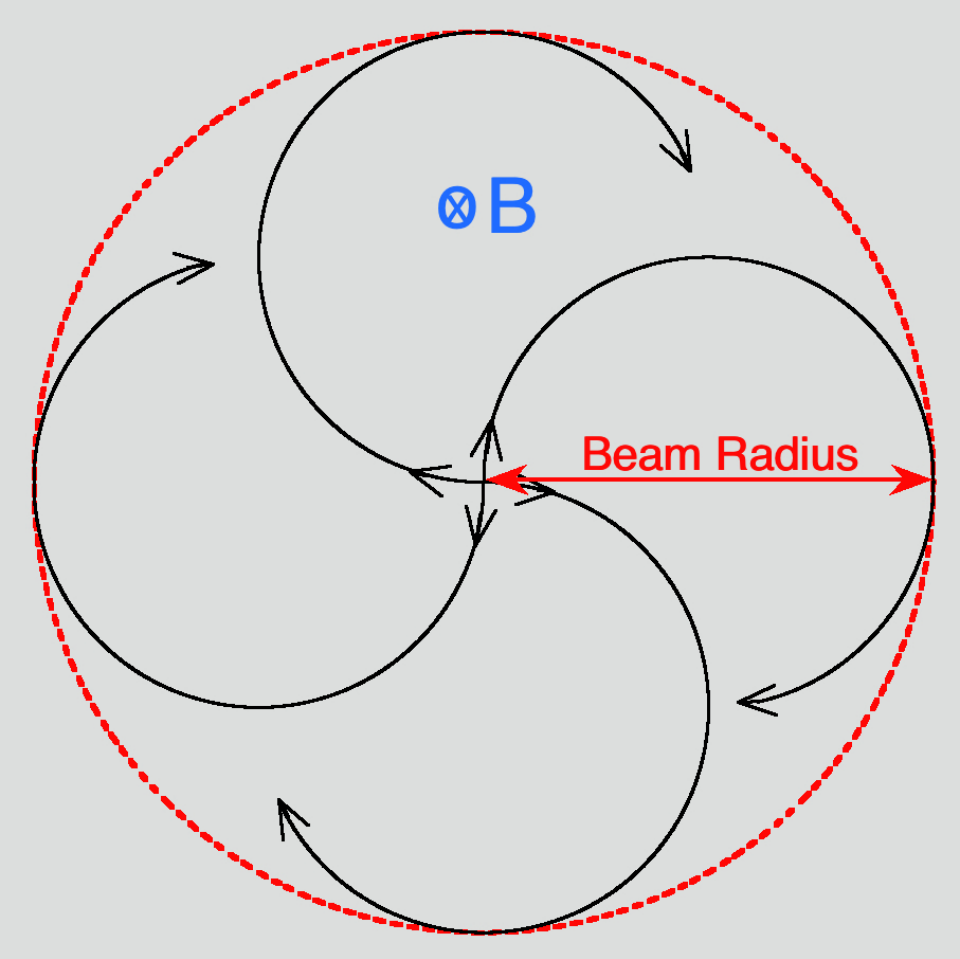

Figure 2. Electrons (black curves with arrows) expanding from an electron bunch (center of figure) across the ambient magnetic field setting the outer radius of the beam (red dashed curve). The view is looking along the Earth's magnetic field (blue notation on figure) from the accelerator toward the Earth's northern ionosphere.

A.1.5. Optical beamspot detection

Bob Marshall, Joe Borovsky, Emma Spanswick

Detection of the beamspot at the magnetic footpoint in the upper atmosphere is fundamental. Previous lower-energy experiments (e.g. Davis et al., 1980; Halllinan et al., 1990) have demonstrated that an electron beam can be detected by means of its optical signature. If the velocity vectors of a 1-MeV beam of electrons are exactly aligned with the Earth's magnetic field at the top of the atmosphere, the 1-MeV electrons will deposit their energy in a narrow altitude range with a peak at about 58 km. If the beam is fired into the loss cone but not at the center of the loss cone, the beam electrons will enter the atmosphere with more-oblique velocity vectors and the energy deposition will be at slightly higher altitudes. Through collisions with atmospheric neutrals, the beam-atmosphere interaction leads to ionization and excitation of N_2 molecules. The 427.8 nm optical band (first-negative band) of the radical N_2^+ will be used for detection of the beam.

Marshall et al. (2019) investigated 1-MeV 1-kW beams of electrons. Figure 1 provides a summary of the ionization and optical-emission properties for a magnetic-field-aligned beam of 1-MeV 1-mA electrons with an average power of 1 kW, injected over 0.5 seconds for a total deposited energy of 500 J. The beam spreads in the atmosphere due to collisions, reaching a radius of 300 m at the peak deposition altitude. Figure 1a shows the total ionization profile, integrated over the beam profile and over the 0.5-s duration of the beam, resulting in ionization pairs per meter of altitude. The peak occurs at 58 km altitude, which depends slightly on the background atmosphere profile used, and has a full-width at half-maximum of 9 km in altitude. Hence, the optical "beam-spot" will be an emitting magnetic-field-aligned column ~0.6 km in diameter and ~ 9 km in length at an altitude of about 60 km. From the ionization profile, the optical emissions are calculated and plotted in Figure 1b. Collisional quenching of the emissions is accounted for in these calculations. While the N_2 Vegard-Kaplan (VK) and First Positive (1P) band systems are the brightest, these are spread over a wide range of visible and infrared wavelengths, making detection difficult. The N_2^+ first negative band (1N) system (yellow curve) will be used, which has prominent bands peaking at 391.4 nm and 427.8 nm. The 391.4-nm band is brighter than the 427.8-nm band by a factor of 3 (Omholt, 1971), however (1) the shorter-wavelength 391.4-nm light suffers from stronger atmospheric attenuation by Rayleigh scattering and (2) camera photon detection efficiencies are typically lower at 391.4 nm than they are at 427.8 nm. For 427.8 nm, the exponential attenuation coefficient for aerosol-free STP air is 0.037 km^{-1} (Penndorf, 1957; ITT, 1977), which is an e-folding distance of 27 km at 760 Torr. At low atmospheric pressures, a 1-kW electron beam will produce 1.1 W of 427.8 nm emission (Bryant et al., 1970). The critical N_2 neutral number density for collisional quenching of the N_2^+ first negative band is 3.6×10^{16} cm^{-3} (cf. Table 4.7 of Jones (1974)). At 58 km the N_2 neutral density is about 5×10^{15} cm^{-3} (Hedin, 1987), so quenching will reduce the optical power of the beam-spot. Shooting obliquely to the magnetic field (shooting into the edge of the loss cone rather than its center) to raise the beam-spot altitude could improve spot detection and also bring the beam-spot closer to the aurora, which occur at altitudes above 100 km.

The optical signatures observed from the ground scale linearly with the total energy deposited by the beam into the atmosphere.

To estimate the optical signal on the ground from the optical emissions in Figure 1b, the optical emission rates in each altitude bin (photons per km of altitude per second, during the 1-kW 0.5-s beam deposition period) are propagated through an atmosphere to the ground using a radiative transfer code such as MODTRAN. These result in a photon flux at the ground, in photons per unit

area per second. The calculation is repeated for each optical emission presented in Figure 1b. We then integrate in wavelength across the product of the instrument wavelength response and the emission band spectrum to estimate the in-band photon flux. Using the photon emission profiles in Figure 1b for N_2^+ 1N (yellow curve), assuming an instrument with a 10 nm passband around the 427.8 nm bandhead, and assuming that the beam spot is directly over the camera, we calculate an expected flux of 8.0×10^6 photons/m^2 at the ground, integrated over the 0.5 second beam period. If the cameras used for the beam-spot detection have effective apertures (factoring in camera efficiency) of 10 cm^2, so the overhead beam-spot will put 6000 photons into the camera. This is sufficient for the beam-spot to be seen against a fairly bright auroral background. For instance, if the auroral background is 1 kR in intensity in the 427.8-nm band, then each square cm of the sky would emit 10^9 photons/s into 4π steradian. If a pixel in the sky at 100-km altitude has an area of 1 km^2, that pixel would emit 10^{19} photons/s of 427.8 nm. At the ground a distance d = 100 km away, the flux of auroral 427.8 nm photons from that sky pixel would be $10^{19}/(4\pi d^2) = 8\times10^3$ photons/cm^2/sec. With a 10-cm^2 effective camera aperture, this is 4×10^4 auroral photons into the camera in 0.5 s. The statistical noise of the $4x10^4$ auroral photons is $(4\times10^4)^{1/2} = 200$ photons. Even with the 6000 beamspot photons spread over several pixels, the beamspot signal is well above the 200 photons per pixel noise of the auroral background. Using a beam on-off blinking sequence coordinated with the camera also makes the beam easier to detect in the presence of auroral emissions.

If the beamspot is not directly above the camera then the beamspot detection is more difficult owing to the $1/d^2$ geometric falloff of the photon flux (where d is the distance between the spot and the camera) and the exponential atmospheric attenuation of the photon flux owing to Rayleigh scattering.

Ideal for this magnetospheric beam experiment, an array of 29 optical all-sky cameras across Canada (an extension of the TREx 6-camera array (Spanswick et al., 2018)) is proposed (see Figure 2). Because of the $1/r^2$ falloff of the intensity of the optical beamspot and because of the strong atmospheric attenuation of 427.8-nm photons, it is advantageous to have the beamspot closer to a ground-based imager. A trade study determined that the 29-camera network should be denser than the existing TREx network: this is a cost-saving solution in contrast to increasing the beam power of the accelerator. Each TREx camera has an approximately 2000 km × 1000 km field of view of the upper atmosphere. The cameras are multispectral imagers collecting 427.8 nm, 557.7 nm, near-infrared, and full-color optical images with high time cadence for the 427.8 nm images. Within the field of the TREx camera array there are also meridian imaging spectrographs, imaging riometers, and total-electron-content detectors.

The high-time-cadence 427.8-nm images will be processed in coordination with the accelerator on-off blink sequence to maximize the beam-spot detection in the presence of auroral 427.8-nm emission. The accelerator beam-blink sequence is 0.5-sec on, 0.5-sec off, 0.5-sec on, 0.5-sec off, 0.5-sec on. To see the optical beam spot against the aurora, the TREx images are time integrated for 0.5 sec and then image subtraction is used on adjacent integrated images. All accelerator-beam firings will be timed such that the estimated arrival time in the atmosphere of the beam front will always occur at the beginning of a UT second, so that image-processing software analyzing the TREx images geared to the UT seconds could run full time. Flight times from the accelerator to the atmosphere are in the range of 0.1 - 0.2 sec.

Bryant, D. E., Courtier, G. M., Skovli, G., Lindalen, H. R., Aarsnes, K., Maseide, K. (1970). Electron density and electron flux in a glow aurora. J. Atmos Terr. Phys. 32:1695.

Davis, T. N., Hess, W. N., Trichel, M. C., Wescott, E. M., Hallinan, T. J., Stenbaek-Nielsen, H. C., Maier, E. J. R. (1980). Artificial aurora conjugate to a rocket-borne electron accelerator. J. Geophys. Res. 85:1722.

Hallinan, T. J., Winkler, J., Malcolm, P., Stanbaek-Nielsen, H. C., Baldridge, J. (1990). Conjugate echoes of artificially injected electron beams detected optically by means of new image processing. J. Geophys. Res. 95:6519.

Hedin, A. E. (1987). MSIS-86 thermospheric model, J. Geophys. Res. 92:4649.

ITT (International Telephone and Telegraph Corporation) (1977). Reference Data for Radio Engineers. Sect. 28, Fig. 32, Howard Sams and Co., Indianapolis, Ind.

Jones, A. W. (1974). Aurora. D. Reidel Publishing, Dordrecht.

Marshall, R. A, Xu, W., Kero, A, Kabirzadeh, R, Sanchez, E. (2019). Atmospheric effects of a relativistic electron beam injected from above: chemistry, electrodynamics, and radio scattering. Front. Astron. Space Sci. 6:6.

Omholt ,A. (1971). The Optical Aurora. Sect. 2.2, Springer-Verlag, New York.

Penndorf, R. (1957). Tables of the refractive index for standard air and the Rayleigh scattering coefficient for the spectral region between 0.2 and 20.0 □ and their application to atmospheric optics. J. Optical Soc. Amer. 47:176.

Spanswick, E., Donovan, E., Liang, J., Weatherwax, A. T., Skone, S., Hampton, D. L., Gillies, M., Yang, B., Chaddock, D., Vollmerhaus, L., Kujawski, J. T. (2018). First-Light Observations from the Transition Region Explorer (TREx) Ground-Based Network. American Geophysical Union, Fall Meeting, abstract SM23B-04,2018AGUFMSM23B.04S.

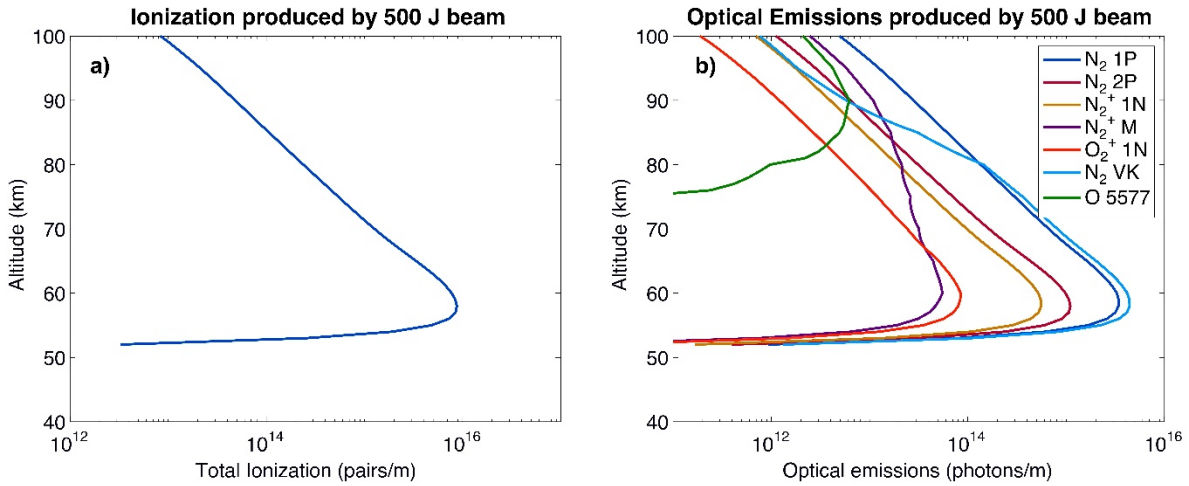

Figure 1. (a) The atmospheric energy-deposition profile a 500-J deposition from a 1-MeV electron beam. (b) The optical-emission profiles for the same 500 J deposition.

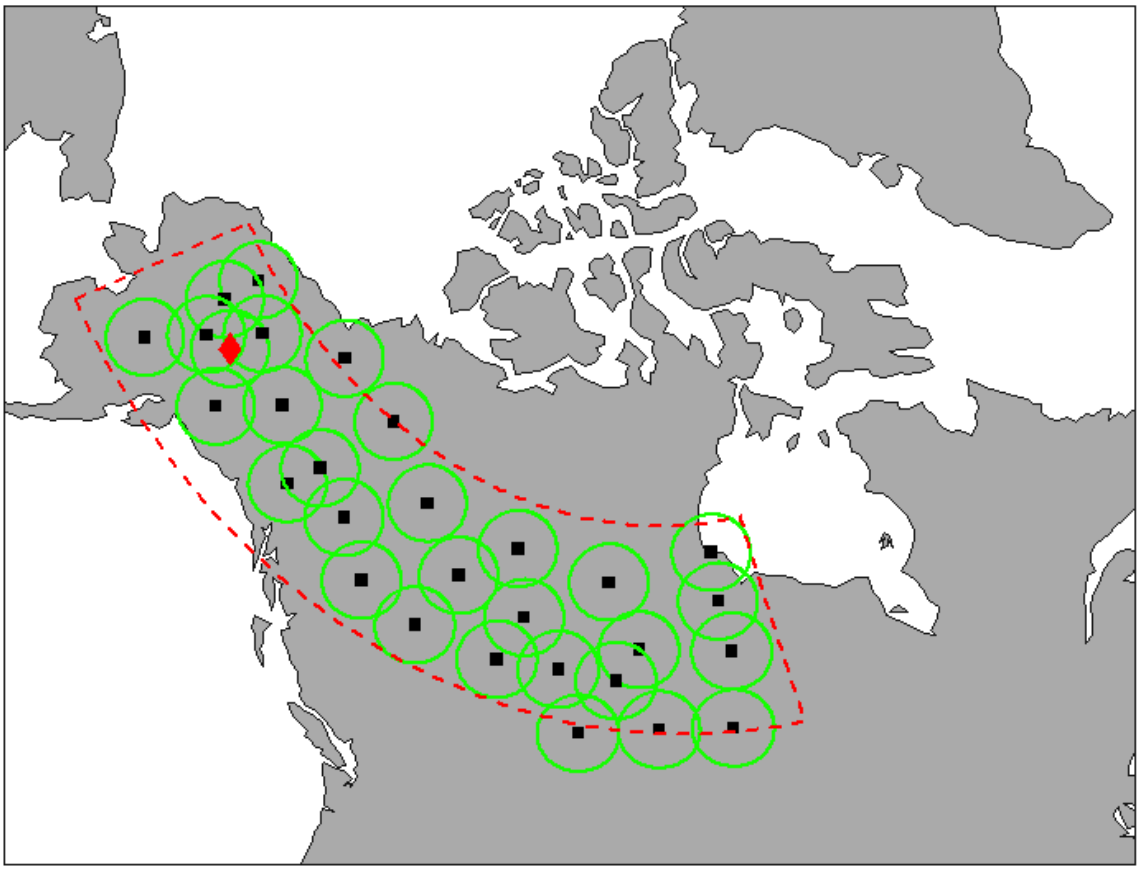

Figure 2. The locations chosen for the 29 optical imagers locating the MIO optical beamspot and putting the beamspot into the context of the aurora.

A.1.6. Clouds and Camera-Viewing statistics

Emma Spanswick and Joe Borovsky

In Figure 1 viewing statistics are shown for the locations of two of the present TREx cameras for the year 2014. The top panel is for Pinawa, Manitoba, the southernmost TREx camera location and the bottom panel is for Fort Smith, Northwest Territories, the northernmost TREx camera location. The vertical units in the graph are the number of 10-minute intervals in each month. The sum of the black and green in each bar is the number of 10-minute intervals of dark sky that month. The length of the green bar is the number of 10-minute intervals of good viewing in that month and the length of the black bar is the number of cloudy, dark-sky 10-minute intervals. Other TREx locations show similar statistics.

A distinct difference between the statistics from a higher-latitude camera (e.g. Fort Smith) and a lower-latitude camera (e.g. Pinawa) is that there are no dark-sky intervals in mid-Summer at the higher latitudes. Summer viewing is restricted to the lower-latitude cameras that are relevant for magnetic connection to the near-Earth portions of the MIO orbit.

In Winter we can expect about 1000 10-minute intervals of good viewing per month, which is about 170 hr of good viewing per month.

Note that every time a beamspot is imaged is a scientific data point magnetically connecting a point in the ionosphere with a location in the magnetosphere.

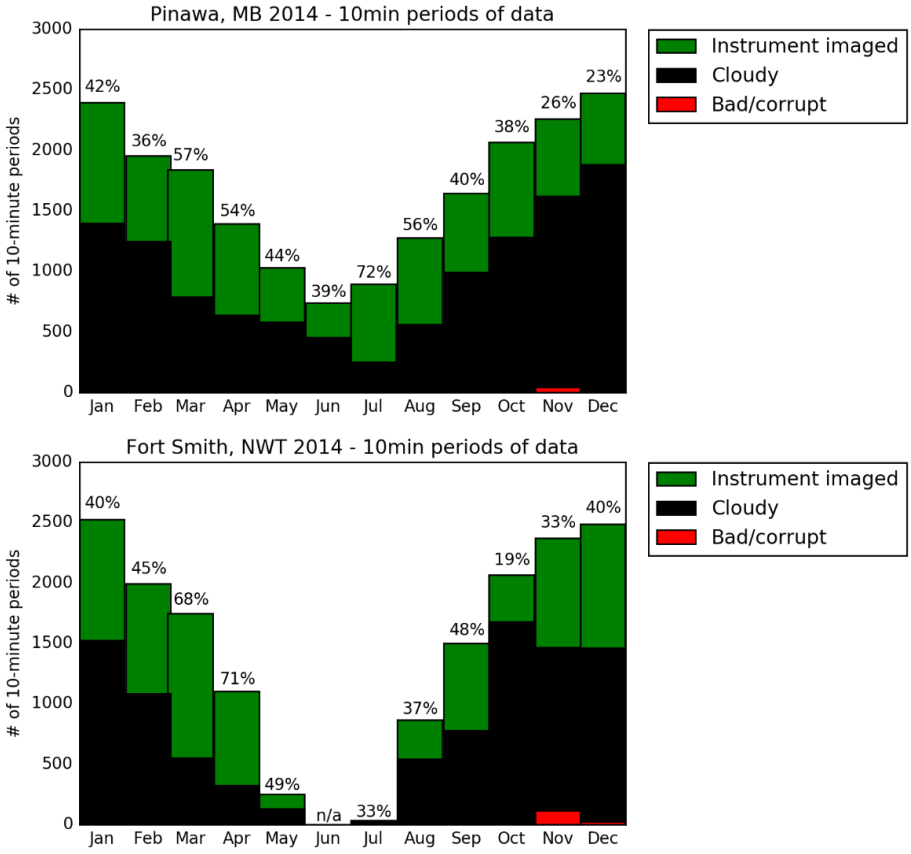

Figure A-5: Viewing statistics for the year 2014 at two of the current TREx camera locations.

A.2. Technology/Concept Maturation Efforts and Opportunities
A.2.1. Strategy for Increasing Accelerator TRL

Michael Holloway

The main strategy for increasing TRL and reducing cost of a MIO accelerator payload would be to build a scaled down laboratory accelerator test stand in a space flight like configuration. The accelerator concept was intentionally designed to be modular as shown in Fig. 1.

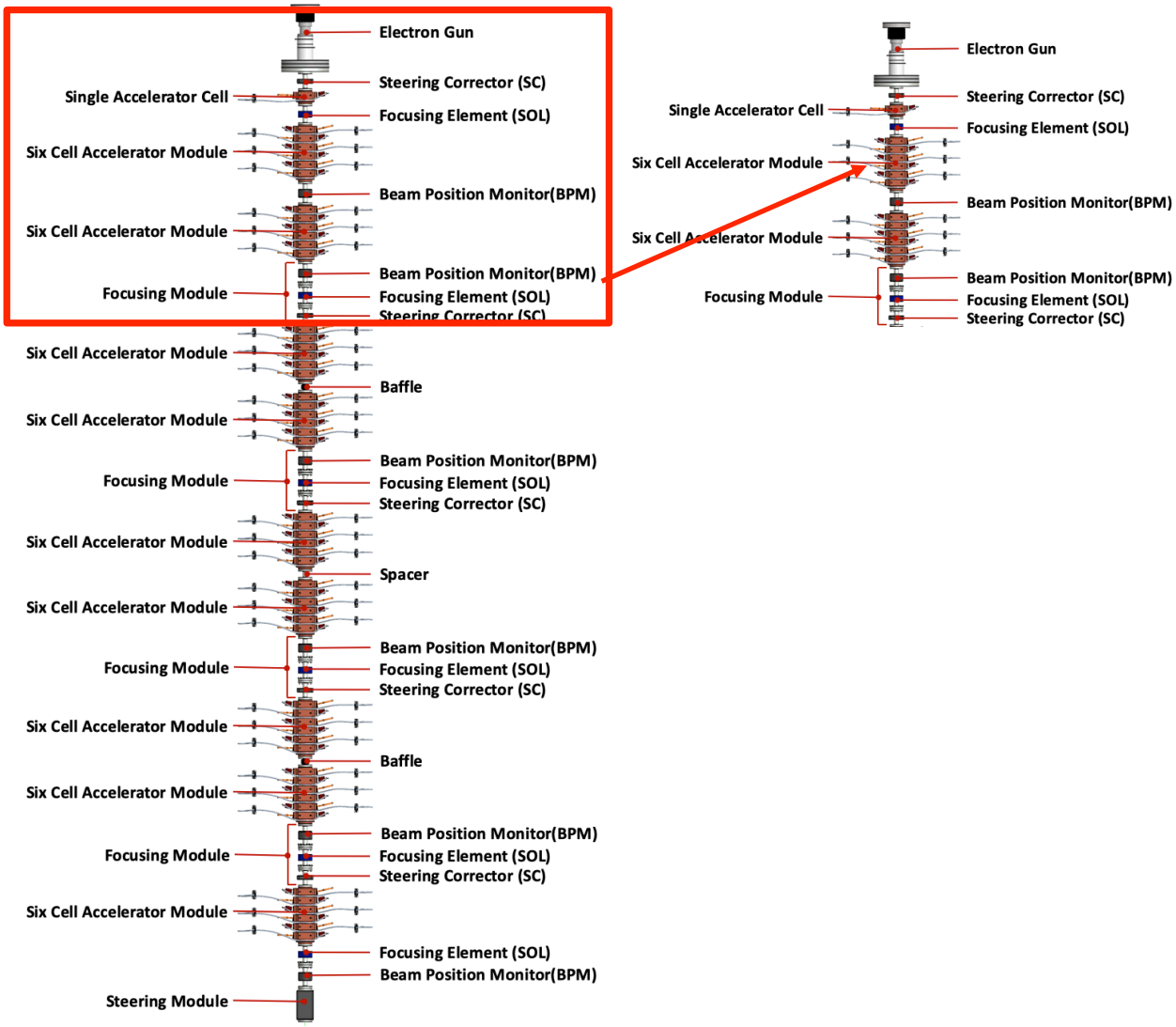

Figure A-6: MIO modular accelerator concept (left) allows for tech maturation with a reduce set of repeatable zones (right) which would significantly reduce tech maturation costs.

A laboratory test stand consisting of a small number of MIO accelerator zones would be sufficient for maturing key technologies discussed below. The test accelerator would then be relatively easy to scale up since it simply means adding more "zones" with identical hardware. Developing on a low energy version also greatly reduces costs associated with radiation safety and facility support, as the power required, and radiation produced by a low energy electron beam are easily managed. An accelerator test stand would also provide the means to explore trade spaces between beam current and beam energy as discussed in section A.2.2. Optimizing this trade space with the science mission requirements could lead to a significant reduction in the challenging technical aspects of the payload and reduce overall mission cost. There are many details of the accelerator that could be worked out and tested to realize a flight instrument using the reduced energy test stand. The following are highlights of some major areas of tech development needed for the MIO accelerator:

RF Cavity Design and Thermal Management

The mechanical design of the RF cavities as well as thermal management of the cavities under operation are crucial to achieving desired energy gain from the accelerator. As the RF copper cavities inevitably heat from ohmic losses during operation, they will expand and shift resonance, which could cause significant loss of energy gain. Ground accelerator facilities have many techniques and resources available to maintain resonance that are not feasible for space missions. The cavities and thermal management system must be designed to minimize mass, optimize cavity quality factor (cavity Q), and minimize temperature variation to ensure electron energy gain over the desired experimental mode of operation for the MIO mission. For tech maturation, cavity designs can be easily modeled and tested in a TVAC chamber to monitor resonance shifts over temperature. The ideal case will be achieving a design that can maintain its resonance during beam firings with tradition thermal management technics used on a satellite. If this cannot be achieved, then an active turner will need to be incorporated in the RF cavity. This will consist of small metallic insert with adjustable depth within the cavity. This will adjust the resonance to compensate for thermal drift. A PID feedback control of the tuning plug will be developed to maintain resonance.

Electron Injector Design and operation

High voltage and high power, power supplies (HVPS) are always challenging for space missions. The MIO mission will require an electron injector capable of at least 300W peak power with the current accelerator design and potentially more depending on results from trade space studies. There exists no off the shelf solution for either the power supply of the electron injector (or electron gun) for space flight. While there have been a few instances of electron injectors flown on satellite experiments [e.g. Prech et al., 1995, 2002, 2018; Zilavy et al., 2003], details of these designs are not available. Expertise in injector technology must be reestablished through targeted technology development. To accomplish tech maturation in this area, LANL, using internal R&D funds, is developing a fully space qualified HVPS and electron injector pair. The current design target is using the current MIO requirements of 10 to 15KeV 20 mA. The team at LANL is also looking into a design where injector emission will be easily gated to match the RF modulation to significantly reduce wasted power during the RF off cycles. If successful, this technology will advance to TRL 4 and can be ready to use in the test accelerator in a flight like configuration by the end of FY23.

RF design

The all-solid-state RF system is the key innovation that enables the MIO accelerator design. The high-power RF is delivered to the cavities by high electron mobility transistors (HEMTs) capable of 500W of peak RF output. Each cavity is driven by a pair of these devices. While a great deal of

power is needed for a MIO accelerator, these devices operate using a 50V supply. This eliminates the need for a high voltage high power solution that would likely not be feasible for the MIO space mission. These relatively new devices have yet to be proven they can be used in a space environment, and it is crucial these devices undergo radiation qualification testing. Some preliminary work was done via a Goddard-LANL partnership, but the initial testing was not conclusive.

The design using HEMTs to individually drive each RF cavity is relatively new. The RF system including the low-level RF electronics needs to be designed and tested to ensure the precise cavity phasing required to maximize electron energy gain. Currently there is a NASA funded rocket experiment at LANL called the Beam Plasma Interaction Experiment (Beam-PIE). This rocket experiment will use several HEMT devices to power a single RF cavity to accelerate electrons up to 50 – 60 KeV. This will be a first of its kind flight experiment using this technology though they will only operate for approximately 300s and will experience a full space environment. In addition, through internal funding, a ground test accelerator for Beam-PIE that uses HEMT's to drive an RF cavity has been developed and is operational. This test facility can be further utilized for the continual develop of solid-state accelerator technology for a MIO mission.

Beam Transport

Forcing particles that don't like to be near each other into tight beams is challenging. Beam transport design is what will determine the design requirements for the focusing magnets that keep the beam together while inside the accelerator. A tight solution that can only tolerant small deviations in beam angles will be difficult for a space mission. Ground accelerators facilities can take time to tweak magnets and adjust focus and steering of the beam until the full transport is achieved. A space mission will not have enough power for any sort of lengthy tuning procedure. Therefore, beam transport solutions must be forgiving to allow for a realistic means to rapidly fire and maintain electron beam performance. Active research is needed to develop beam transport solutions for a MIO like accelerator. These solutions will need to be further tested in a real beamline to ensure that achieving full beam transport in a MIO like accelerator is rapid and repeatable.

Control System/Diagnostic Design

The MIO accelerator will have to operate much differently than a typical accelerator facility. Flight control systems will need to monitor and control temperature, cavity resonance, beam current, beam position in the accelerator, and RF power to ensure beam energy and power are within mission specifications. For ground accelerator facilities, much of the delicate tuning of these machines is done manually in a control room, and it can take hours to get a beam ready for an experiment. Rapidly preparing an electron accelerator to fire on μs time scales is a unique challenge for this mission and active technology development will be needed for a MIO accelerator control system.

A.2.2. Accelerator Trades

Joe Borovsky and Michael Holloway

The MIO space-based accelerator design was optimized for maximum beam power into the atmospheric loss cone using present-day technology [cf. Lewellen et al., 2019].

One trade study that was performed was motivated by a desire to lower the MIO accelerator energy from 1 MeV to 500 keV and to increase the beam current from 1 mA to 2 mA to maintain the average beam power of 1 kW. The motivation for lowering the beam energy (besides making the accelerator shorter) was to reduce the magnitude of the angular shift of the atmospheric loss cone away from the magnetic-field direction. The decision was made not to lower the MIO accelerator energy to 500 keV. The reasons were twofold. (1) Examination of the magnitude of the loss-cone shift in the nightside magnetosphere using a realistic magnetic-field model found that the loss-cone-shift problems are not noticeably reduced by going from 1 MeV to 500 keV, and the MIO orbit selection greatly reduces the loss-cone-shift issues. (2) It is very difficult to double the beam current in the MIO accelerator design, and the loss of beam power using 500 keV and only 1 mA of current is not acceptable.

In light of future technologies, future examinations of the MIO mission concept should consider the important questions of accelerator type, accelerator energy, and accelerator power. Power, which is accelerator voltage (energy) times accelerator beam current, is of the utmost importance, but attaining more beam power drives a number of difficulties.

The trade space for choosing beam voltage and beam current is multidimensional. The multiple issues that play roles in choosing the optimal beam energy and beam current are itemized in Table 1. These issues are organized into "operational issues" that impact the performance of the scientific experiment and "engineering issues" that affect mass, power, costs, TRL, feasibility, etc. In this Appendix the discussion will focus mostly on the operational issues impacting the MIO scientific experiment.

For more power (Item 1 in Table 1), it is desirable to have higher beam energy and/or to have higher beam current.

Operational issues that are improved by increasing the beam energy are the following: (Item 1) increased beam power; (Item 4) a decreased beam angular divergence; (Item 8) even more beam stability as the beam propagates through the magnetospheric plasma; (Item 9) less angular scattering by ambient magnetospheric plasma waves since the scattering by chorus waves decreases with electron energy and the scattering by EMIC waves is approximately independent of electron energy; and (Item 14) increasing the ability to do atmospheric-electricity experiments by increasing the conductivity channel in the upper atmosphere formed by the beam.

Operational issues that are made worse by increasing the beam energy are the following: (Item 7) finding the true loss cone, since an increased beam energy means an increased electron gyroradius in the magnetosphere and larger angular shifts of the loss cone; (Item 2) the ease of pointing the accelerator, since the accelerator will be physically longer; (Item 3) the angular range of magnetic steering of the beam will be reduced since the relativistic mass of the beam electrons will be greater; (Item 11) since a more-energetic beam will deposit its energy at a lower altitude in the atmosphere

where molecular collisions are more frequency, collisional quenching of the beam's optical emission will be greater, meaning less optical emission per Watt of beam power; (Item 12) since a more-energetic beam will deposit its energy at a lower altitude in the atmosphere where electron attachment to molecules is faster, the free-electron number density caused by beam ionization of air will decay faster and if ground-radar study of the beam spot is of interest, it will be more difficult for radars to detect the beamspot; finally (Item 15) the beam electrons having higher energies means they are more penetrating to any neighboring spacecraft that might be hit by the MIO beam, requiring more-stringent safe-operating procedures for MIO.

Operational issues that are improved by increasing the beam current are the following: (Item 1) increasing the beam power; (Item 12) the detectability of the beamspot in the atmosphere by ground-based radar (increasing the ionization); (Item 13) increasing the possibility of detecting the beamspot by ground-based VLF listening (increasing the strength of the sudden current perturbation under the ionosphere); and (Item 14) increasing the ability to do atmospheric-electricity experiments by increasing the conductivity channel in the upper atmosphere formed by the beam.

Operational issues that are made worse by increasing the beam current are the following: (Item 10) spacecraft charging by removing more negative charge from the accelerator main spacecraft; (Item 4) beam divergence since a higher-current beam has more space charge and thus more space-charge-driven transverse divergence; (Item 8) beam stability since a higher-density beam brings the situation of a beam propagating through a plasma closer to instability; and (Item 15) the beam electrons having higher fluxes means they are more hazardous to any neighboring spacecraft that might be hit by the MIO beam, requiring more-stringent safe-operating procedures for MIO.

Early considerations of the MIO mission concept focused on the use of a DC electron gun to produce the electron beam [Borovsky, 2002] rather than an electron linac. In light of the evolution of technology, it might be wise to revisit the debate between DC electron guns and electron linacs with the MIO mission goals in mind [e.g. Sect. 4 of Borovsky et al., 2020c]. Multiple experiments have been flown in space using DC Voltage biases to produce electron beams in the energy range of 10s of keV and 10's of kW powers have been flown in space numerous times [e.g. Winckler et al., 1975; O'Niel et al., 1978; Rappaport et al, 1993; Prech et al., 1995, 2018; McNutt et al., 1995]. An advantage of the DC-beam methodology over the linac methodology is that much larger beam powers can be produced. High-power DC guns, however, have high beam current: two main drawbacks to these large beam currents are (1) a severe space-charge-driven beam divergence such that the beam divergence angles are larger than the size of the atmospheric loss cone and hence beam energy is wasted since it all does not reach the atmosphere and (2) larger beam currents mean more-severe mitigation needed for beam-driven spacecraft charging. If the DC beams could attain energies in 100-keV level this could be a technological sweet spot. However, such high DC Voltages require large stand-off distances to prevent electrical breakdown and these large distances drive the physical size and mass of the gun. Note that most DC electron guns were flown on rockets: designing DC guns and the needed high-Voltage power supplies for flights on magnetospheric spacecraft will present additional difficulties.

Note that lowering the energy of the electron beam reduces the difficulty of dealing with the eastward loss-cone shift, but the reduction is surprisingly mild. This loss-cone shift results in a region in the nightside magnetosphere where the MIO mission would have difficulty operating. Figure 1 illustrates this. The two panels of Figure 1 plot in color the angular size of the eastward angular shift of the atmospheric loss cone away from the direction of the magnetic field. The yellow-

shaded region in both panels is where the angular shift is 0.5° or less. In the yellow region the MIO accelerator can be operated with confidence that the beam can be aimed into the atmosphere. Regions other than yellow are "forbidden". The top panel of Figure 1 plots the shift for a 1-MeV electron beam and the bottom panel plots the shift for a 50-keV electron beam. The forbidden zone is shrunk in size in the 50-keV bottom panel, but the loss-cone-shift problem does not vanish.

In Table 1 a not-comprehensive list of engineering issues (16-23) is compiled: these are additional tradeoffs in varying the energy and current of the MIO accelerator. These trades are not discussed in this Appendix.

Borovsky, J. E., (2002). The Magnetosphere-Ionosphere Observatory (MIO). Los Alamos National Laboratory https://www.lanl.gov/csse/MIOwriteup.pdf.

Borovsky, J. E., Delzanno, G. L., Valdivia, J. A., Moya, P. S., Stepanova, M., Birn, J., Blum, L. W., Lotko, W., Hesse, M. (2020c). Outstanding questions in magnetospheric plasma physics: The Pollenzo view. J. Atmos. Solar-Terr. Phys. 208:105377.

Lewellen, J. W., Buechler, C. B., Carlsten, B. F., Dale, G. E., Holloway, M. A., Patrick, D., Storms, S. A., Nguyen, D. C. (2019). Space borne electron accelerator design. Front. Astron. Space Sci. 6:35.

McNutt, R. L., Rieder, R. J., Keneshea, T. J., LePage, A. J., Rappaport, S. A., Pualsen, D. E. (1995). Energy deposition in the upper atmosphere in the EXCEDE III experiment. Adv. Space Res. 15(12):13.

O'Neil, R. R., Shepherd, O., Reidy, W. P., Carpenter, J. W., Davis, T. N., Newell, D., Ulwick, J. C., Stair, A. T. (1978). Excede 2 test, an artificial auroral experiment: Ground-based optical measurements. J. Geophys. Res. 83:3281.

Prech, L., Nemecek, Z., Safrankova, J., Simunek, J., Truhlik, V., Shutte, N. M. (1995). Response of the electron energy distribution to an artificially emitted electron beam: APEX experiment. Adv. Space Res. 15(12):33.

Prech, L., Ruzhin, Y. Y., Dokukin, V. S., Nemecek, Z., Safrankova, J. (2018). Overview of APEX Project results. Front. Astron. Space Sci. 5:46.

Rapport, S. A., Rieder, R. J., Reidy, W. P., McNutt, R. L., Atkinson, J. J., Paulsen, D. E., 1993. Remote x-ray measurements of the electron-beam from the EXCEDE-III experiment. J. Geophys. Res. 98:19093.

Winckler, J. R., Arnoldy, R. L., Hendrickson, R. A. (1975). Echo-2: Study of electron beams injected into the high latitude ionosphere from a large sounding rocket. J. Geophys. Res. 80:2083.

Table 1. Trade issues for obtaining more beam power by increasing the beam energy and/or increasing the beam current. Issues 1-15 are operational issues "Type O" affecting the ability to achieve the mission science goals and issues 16-23 deal with engineering issues "Type E".

	Issue	Type	Increasing Beam Energy	Increasing Beam Current	Impact on Mission
1	Need for More Beam Power	O	better	better	Important
2	Ease of pointing accelerator	O	worse	no impact	Important
3	Angular range of magnetic beam steering	O	worse	no impact	Important
4	Beam divergence versus size of loss cone	O	better	worse	Minor
5	Complexity of operations	O	TBD	TBD	Important
6	Ability for on-off beam sequencing	O	no impact	no impact	Important
7	Finding the true loss cone	O	worse	no impact	Important
8	Beam stability in magnetospheric plasma	O	better	worse	Minor
9	Beam scattering from ambient waves	O	better	no impact	Minor
10	Spacecraft charging	O	no impact	worse	Important
11	Optical quenching (altitude of beamspot)	O	worse	no impact	Minor
12	Radar detection (altitude of beamspot)	O	worse	better	Minor
13	VLF (radio) beamspot detection	O	no impact	better	Minor
14	Atmospheric-electricity science	O	better	better	Minor
15	Safety issues of intercepting another s/c	O	worse	worse	Minor
16	Efficiency: energy storage to beam power	E	future	future	Important
17	Length of accelerator	E	future	future	Important
18	Mass of accelerator	E	future	future	Important
19	Thermal issues: detuning and cooling	E	future	future	Important
20	Interference: magnetic, radio-frequency, …	E	future	future	Important
21	Launch survival	E	future	future	Important
22	Radiation sensitivity	E	future	future	Important
23	TRL	E	future	future	Important

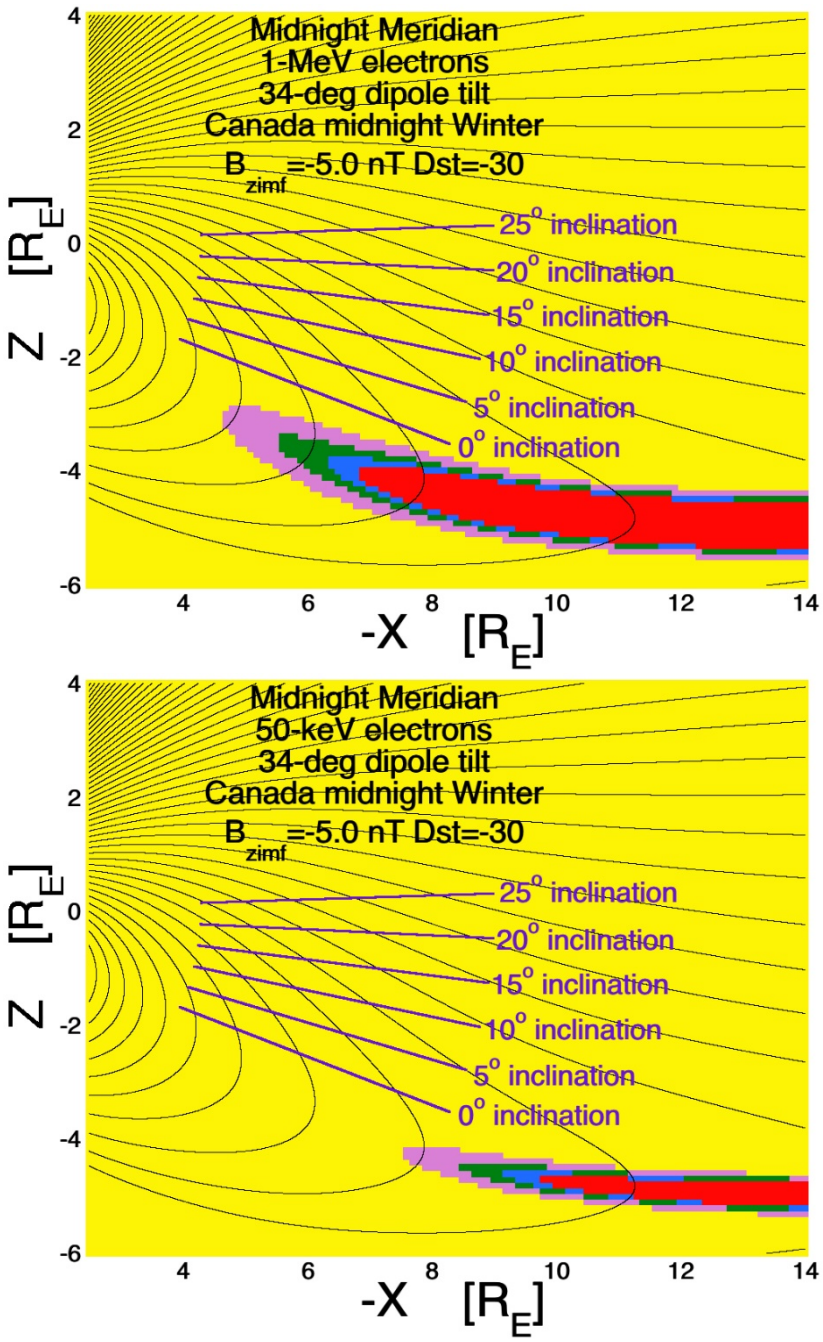

Figure 1. For the magnetic dipole tipped 34°, representing the dipole tilt at the December equinox when Canada is at local midnight, magnetic-field lines in the nightside magnetosphere in the noon-midnight meridian are drawn as the black curves using the T96 magnetic-field model. The orbital planes of a $4.3R_E$-by-$9R_E$ MIO orbit are drawn as the line segments labeled for the various orbit inclinations. The colored shading is the calculated eastward shift of the local atmospheric loss cone for 1-MeV electrons (top panel) and for 50-keV electron (bottom panel) based on the local magnetic-field strength and the local radius of curvature of the magnetic field lines calculated in the T96 magnetic-field model. The color scheme is yellow (shift < 0.5°), pink (shift 0.5° - 1°), green (shift 1° - 1.5°), blue (shift 1.5° - 2°), and red (shift > 2°). Essentially, it is prudent to operate the MIO accelerator only in the yellow shaded zones.

A.2.3. Missions that MIO can leverage for design maturation

B-SPICE: A NASA funded Low Cost Access to Space rocket experiment to confirm the MIO charging-mitigation scheme is scheduled to launch in 2023 [Miars, et al., 2019; Miars, 2020]. The payload will be an electron beam and a plasma contactor. The Principal Investigator is Brian Gilchrist at the University of Michigan.

Beam-PIE: A NASA funded Low Cost Access to Space rocket experiment to advance the technology of high-electron-mobility transistor (HEMT) use for electron accelerators in space [Reeves et al., 2020]. The electron accelerator for Beam-PIE will use the same cavity technique as MIO and, like MIO, will operate at 5.1 GHz. The Principal Investigator is Geoff Reeves at Los Alamos National Laboratory.

MagCon: The Magnetospheric Constellation (MagCon) is a NASA mission concept to deploy 24 to 36 small spacecraft in the Earth's magnetotail [Kepko, 2018]. The development of the 4 daughter spacecraft for MIO was based on the preliminary designs of the MagCon small spacecraft. Like the MIO daughters, the MagCon spacecraft each carry and ESA and a magnetometer. Larry Kepko at NASA/Goddard is the Principal Investigator for the MagCon mission concept study.

A.3. Mission Design Analysis

A.3.1. Mission Design Table

Table A-2: Mission Design Table

Parameter	Value	Units
Orbit Parameters: Apogee	9	Earth Radii
	57,200	Km
Orbit Parameters: Perigee	4.3	Earth Radii
	27,100	Km
Orbit Parameters: Inclination	1-5	deg
Mission Lifetime	24	mos
Maximum Eclipse Period	81	min
Launch Site	Cape Canaveral	
Mothership	1	Qty
Mass **with** contingency (includes instruments)	963	kg
Propellant Mass **without** contingency	767	kg
Propellant contingency	15	%
Propellant Mass **with** contingency	882	kg
Daughtership	4	Qty
Mass **with** contingency (includes instruments)	77	kg
Propellant Mass **without** contingency	15	kg
Propellant contingency	15	%
Propellant Mass **with** contingency	17	kg
Launch		
Launch Adapter Mass **with** contingency	50	kg
Total Launch Mass	2,749	kg
Launch Vehicle	2	Type
Launch Vehicle Lift Capability	3,300	kg
Launch Vehicle Mass Margin	551	kg
Launch Vehicle Mass Margin (%)	16.6	%

Note: Launch trades were performed assuming a launch from Cape Canaveral, but other launch opportunities exist which may lead to better performance. For example, launching from Kwajalein would significantly reduce the size of the orbit inclination change.

A.3.2. The Loss-Cone Shift and Its Impact on Orbit Selection

Joe Borovsky, Mike Henderson, Gian Luca Delzanno

The decision was made that the optimal orbit for MIO is a $4.3R_E$ by $9R_E$ 24-hr elliptical orbit with a low inclination and with its magnetic connections to the expanded TREx camera network in Canada-Alaska. One orbital requriement is a magnetic mapping to the vicinities of the PFISR and HAARP facilities in Alaska once per 24 hours.

Issues of concern are the locations of the spacecraft and the magnetic footpoint: specifically (1) magnetic-footpoint mapping relative to the camera arrays and (2) spacecraft location relative to the morphology of the Earth's magnetosphere. That second issue drives the choice of inclination and that the inclination should be in the range from 0^o to 5^o.

To get MIO beam electrons into the atmosphere to create a detectable optical beamspot, the MIO of accelerator beam needs to be aimed into the "atmospheric loss cone". Normally, the atmospheric loss cone is considered to be aligned with the local magnetic-field direction, so shooting into the loss cone would mean aiming the beam so that it is aligned with the local magnetic field direction. However, for energetic particles there are "finite-gyroradius" effects that shift the atmospheric loss-cone orientation away from the magnetic-field direction [e.g. Porazik et al., 2014; Borovsky et al., 2022a,b]. In the Earth's magnetic field, this shift is eastward for electrons. The magnitude of the angular shift of the loss cone depends on the mass and energy of the particles, on the local magnetic-field strength, and the local radius of curvature of the magnetic-field lines. The loss-cone shift (aberration) is simply described using the "Mozer transform" [Mozer, 1966], which points out that the angular shift is

$$\theta_{shift} = \arcsin(v_{curve}/v_o) = \arctan(v_{curve}/v_{||})$$

where v_o is the particle's total velocity, $v_{||}$ is the component of the particle's velocity that is parallel to the magnetic field, and v_{curve} is the curvature drift velocity of the particle in the magnetic field

$$\underline{\mathbf{v}}_{curve} = (m\gamma c/qB^3)\, v_{||}^{\,2}\, (\underline{\mathbf{B}}\times\nabla B)$$

(cf. eq. (2.17) of Roederer and Zhang [2014]), where m is the mass of the particle, q the signed charge of the particle, c the speed of light, and $\gamma = (1 - (v_o^2/c^2))^{-1/2}$ is the relativistic factor. For a dipole magnetic field, the angular shift is easily calculated [Mozer, 1966; Il'in et al. 1992; Il'ina et al., 1993; Borovsky et al., 2022a,b] because the radius of curvature of the field lines in a dipole is analytically calculable. In the Earth's nightside magnetosphere, where the magnetic field can be strongly distorted from a dipole morphology, the magnitude of the loss-cone eastward angular shift is not yet predictable because the local field-line curvature cannot be easily estimated.

In Figure 1 is a map of the magnitude of the loss-cone angular shift eastward in the nightside magnetosphere when Canada is at local midnight near the December solstice. The map was created using the T96 [Tsyganenko, 1995; Tsyganenko and Stern, 1996] magnetic-field model to calculate the magnetic-field strength B and the local ($\underline{\mathbf{B}}\times\nabla B$) curvature of the magnetic-field lines. Magnetic-field lines are drawn in black. Note that there is a strong "dipole tilt" to the field in the Canadian sector with the dipole equator southward from the geographic equator. The yellow-shaded zones in Figure 1 are regions of the magnetosphere where the atmospheric loss cone angular shift is small ($< 0.5^o$) and hence where the aiming of the MIO electron beam is certain to hit the atmospheric loss cone.

The purple line segments in Figure 1 denote the planes of $4.3R_E$-by-$9R_E$ orbits with different inclinations as labeled. In choosing the orbit it is very desirable (1) to not operate the MIO 1-MeV electron accelerator in regions that are not yellow, (2) to operate the beam as close as possible to the non-yellow regions (where auroral-generation physics is suspected to be highest), and (3) to not operate the MIO accelerator in regions where the beam needs to pass through a non-yellow region

to get to the northern ionosphere. Hence, orbits with inclinations near 0^o are most desirable from a mission-objective point of view.

During other times of the year (away from the December solstice) the picture in the nightside magnetosphere is very similar. Keeping the loss-cone shift small and desiring to be near the stretched-field region where the loss-cone shift is big leads to a desire to have an MIO orbit with an inclination near 0^o.

Figure 2 plots the half-angle $\theta_{l.c.}$ of the atmospheric loss cone (colors) for the same dipole tilt as Figure 1 and labeling the same orbital inclinations for MIO. Note for all of the MIO orbital planes shown, the half-angle of the loss cone is greater than 1.5^o, which presents an easy target to hit with the narrow-divergence MIO 1-MeV electron beam.

If the local curvature of the magnetic field in the magnetosphere (which is not measurable) could be ascertained, the loss-cone shift could be calculated and the accelerator aimed accordingly. With MIO operational, a program of research could be implemented and tested with the MIO beam firings wherein magnetic-field models or computer simulations of the Earth's magnetosphere could be used to predict the local curvature of field lines at the MIO location and the loss-cone angular shift could be estimated and confirmed with MIO beam firings. If that program was to be successful, then successful firings from the non-yellow zone of the magnetosphere could be made.

Figure 3 shows the estimated magnetic mapping of the $4.3R_E$ by $9R_E$ 24-hr orbit at Kp=2 (typical levels of geomagnetic activty) for January 24 (Canadian winter) for two different inclinations: the top panel is for a 28.4^o inclination and the bottom panel is for a 0^o inclination. Note that the actual mapping will depend on the level of geomagnetic acivity and on local auroral currents. With time the magnetetic footpoint of MIO moves counterclockwise along the gray plotted track. The tickmarks on the track are 1-hr intervals of time. The mappings relative to the cameras are good for both of these inclinations. At lower inclinations the 24-hr footpoint path is a simple closed curve shaped like a banana, but at higher inclinations (and at higher levels of geomagnetic activity) the orbit crosses itself. This crossing property could be advantageous in that two passes per 24 hours of the PFISR-HAARP facilities could be obtained.

Borovsky, J. E., Delzanno, G. L., Yakymenkno, K. N. (2022a). Pitch-angle diffusion in the Earth's magnetosphere organized by the Mozer-transformed coordinate system. Front. Astron. Space Sci. 9:810792.

Borovsky, J. E., Yakymenko, K. N., Delzanno, G. L. (2022b). Modification of the loss cone for energetic particles in the Earth's inner magnetosphere. J. Geophys. Res. 2021JA030106, in press.

Il'in, V. D., Kuznetsov, S. N., Yushkov, B. Y., Il'in, I. V. (1992). Quasiadiabatic model of charged-particle motion in a dipole magnetic confinement system under conditions of dynamic chaos. JETP Lett. 55, 645-649.

Il'ina, a. N., Il'in, V. D., Kuznetsov, S. N., Ysushkov, B. Y., Amirkhanov, I. V., Il'in, I. V. (1993). Model of nonadiablatic charged particle motion in the field of a magnetic dipole. JETP 77, 246-252.

Mozer, F. S. (1966). Proton trajectories in the radiation belt. J. Geophys. Res. 71:2701.

Porazik, P., Johnson, J. R., Kaganovich, I., Sanchez, E. (2014). Modification of the loss cone for energetic particles. Geophys. Res. Lett. 41:8107.

Roederer, J. G., Zhang, H. (2014). Dynamics of Magnetically Trapped Particles. Springer-Verlag, Berlin.

Tsyganenko, N. A. (1995). Modeling the Earth's magnetospheric magnetic field confined within a realistic magnetopause. J. Geophys. Res. 100:5599.

Tsyganenko, N. A., Stern, D. P. (1996). Modeling the global magnetic field of large-scale Birkeland current systems. J. Geophys. Res. 101:27187.

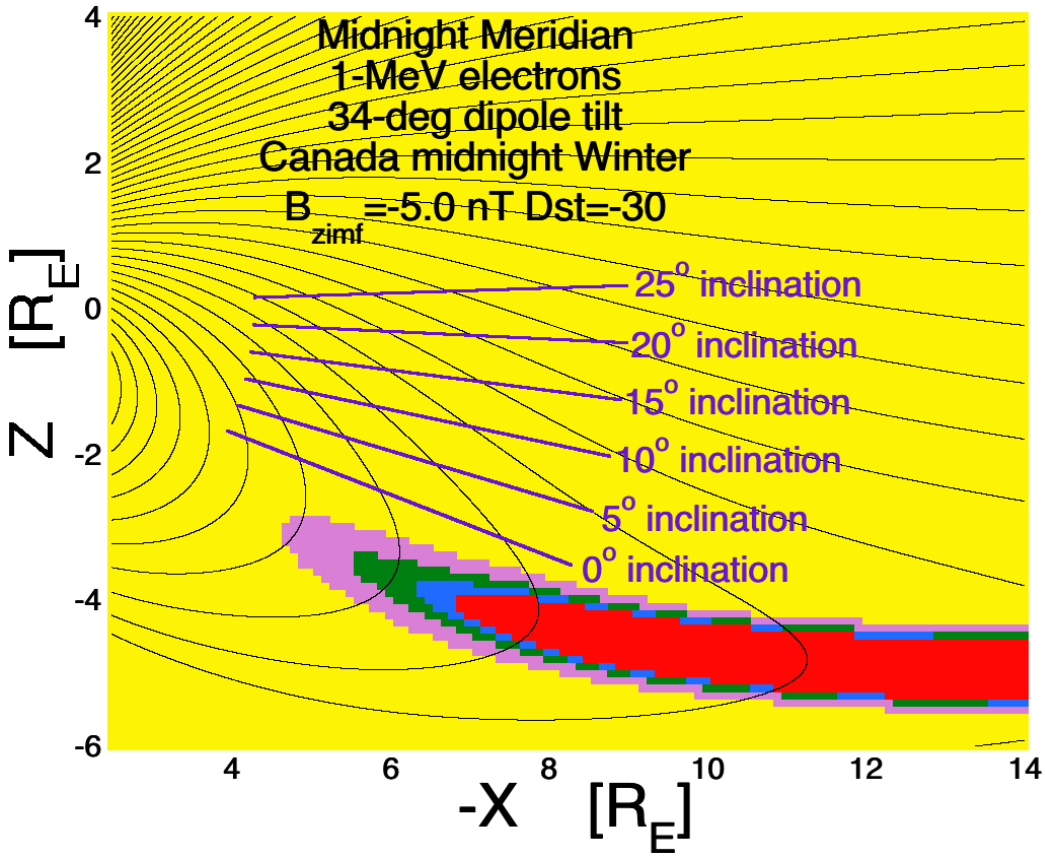

Figure 1. Magnetic-field lines in the nightside magnetosphere in the noon-midnight meridian are drawn as the black curves using the T96 magnetic-field model. The dipole equator on the nightside is tipped 34° southward, representing the dipole tilt at the December equinox when Canada is at local midnight. At this time the Earth's spin axis is tilted away from the Sun by 23° and the dipole is tilted a further 11°. In the plot Z is the north-south direction and X is the Sun-Earth direction. The approximate orbital planes of a $4.3R_E$-by-$9R_E$ MIO orbit are drawn as the line segments labeled for the various orbit inclinations. The colored shading is the calculated eastward shift of the local atmospheric loss cone for 1-MeV electrons based on the local magnetic-field strength and the local radius of curvature of the magnetic field lines calculated in the T96 magnetic-field model. The color scheme is yellow (shift < 0.5°), pink (shift 0.5° - 1°), green (shift 1° - 1.5°), blue (shift 1.5° - 2°), and red (shift > 2°). Essentially, it is prudent to operate the MIO accelerator only in the yellow shaded zones.

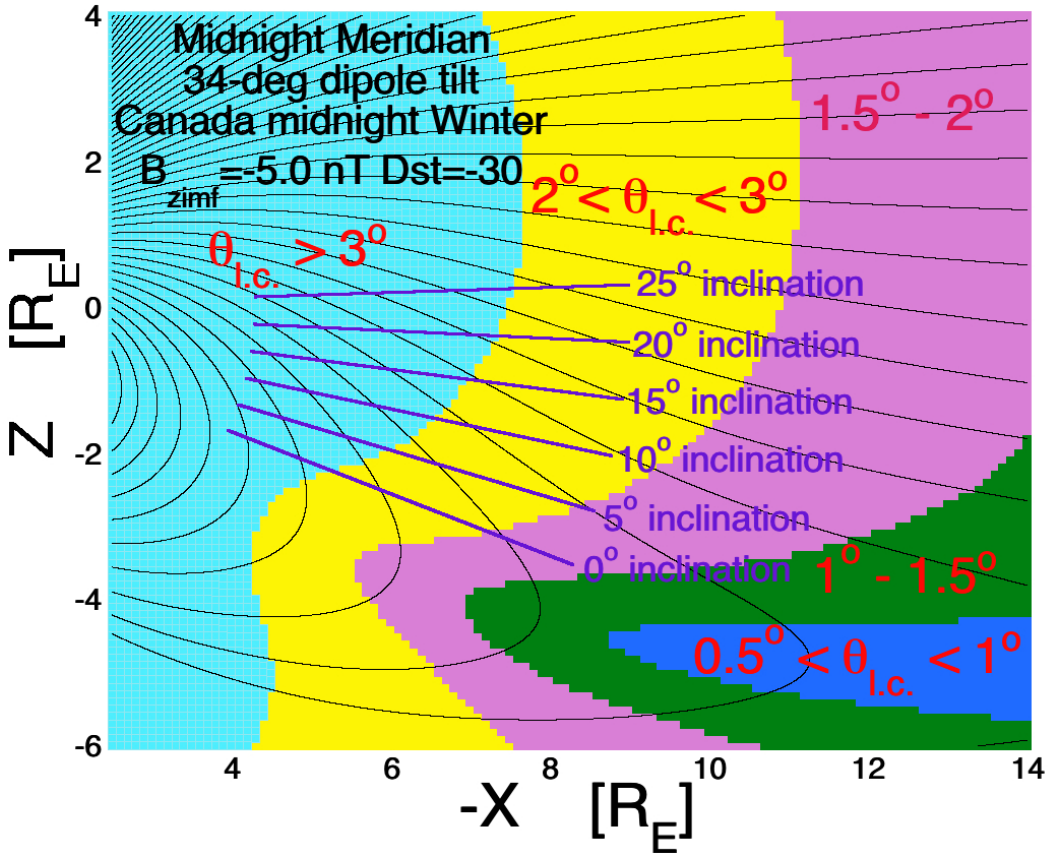

Figure 2. Same parameters as Figure 1, but the half-angle of the atmospheric loss cone θ_{lc} is plotted in color. In the light-blue shaded region $\theta_{l.c.} > 3^{o}$, in the yellow region $2^{o} < \theta_{lc} < 3^{o}$, in the pink shaded region $1.5^{o} < \theta_{lc} < 2^{o}$, in the green shaded region $1^{o} < \theta_{lc} < 1.5^{o}$, and in the blue shaded region $0.5^{o} < \theta_{lc} < 1^{o}$.

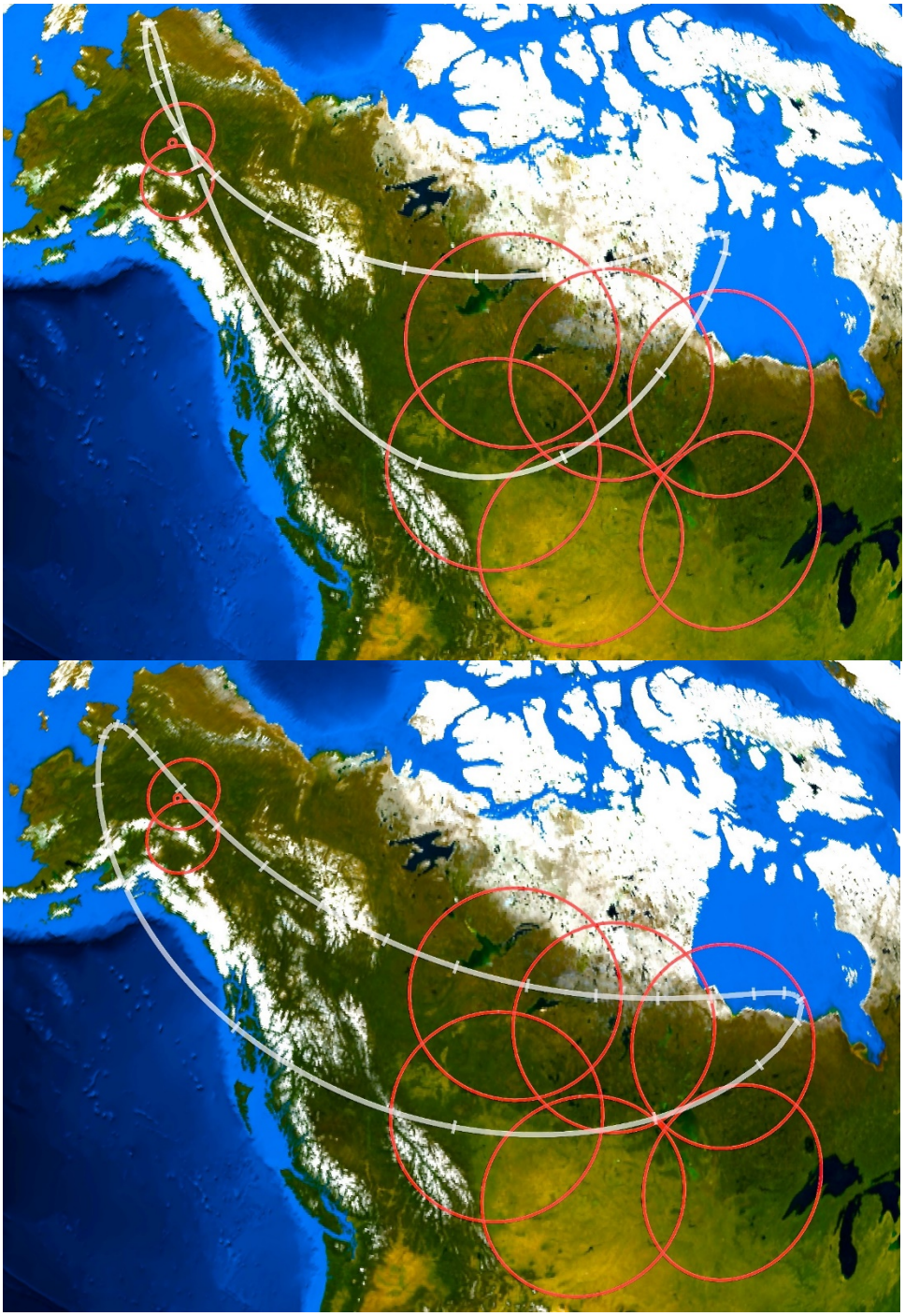

Figure 3. The approximate magnetic footpoint track for a 24-hr 4.3R_E x 9 R_E orbit. The top panel is for an orbit with 28.4o of inclination and the bottom panel is for an orbit with o0 of inclination. The large red circles are the fields-of-view of the present TREx cameras and the smaller red circles are the locations in Alaska of PFISR and HAARP.

A.3.3. Launch/Insertion

A variety of launch and insertion methods were considered for this study including direct injection to the mission orbit, launch to apogee (with and without inclination change), bi-elliptic transfers, and launch to LEO with EP spiral out. A launch to the mission apogee has a C3 of -9.46 km^2/s^2 while bielliptic transfers run from -9.46 km2/s2 to -4.78 km2/s2 (Figure A-7 and Figure A-8). EP was considered because the power needs of the payload seemed conducive to an EP system. Upon further evaluation, the power profile of the payload was incompatible with the sustained power needs of an EP system so this approach was rejected. Cape Canaveral was the launch site for this study in order to stick with a generic launch vehicle. Future studies should evaluate lower latitude launch sites like Kwajalein if the specific launch vehicle is capable of launching from that site.

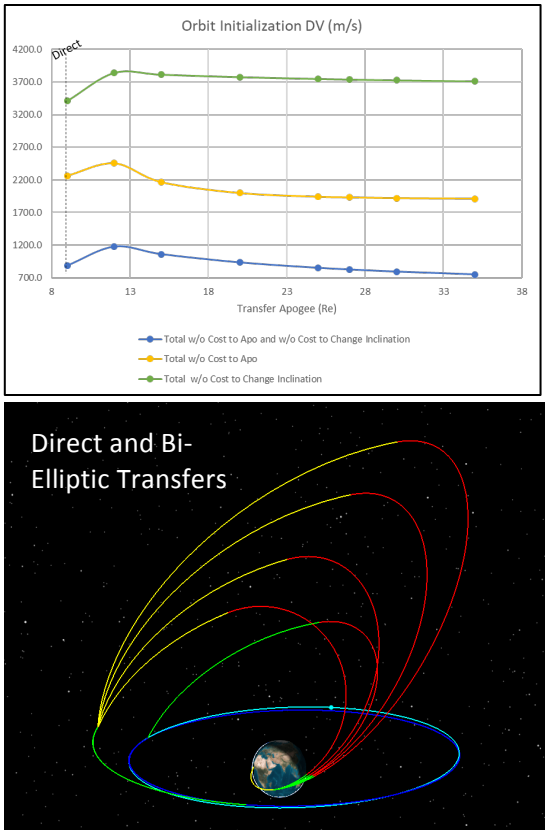

Figure A-7: Transfer orbits with delta-V required to achieve mission orbit inclination and apogee.

It should be noted that the use of a generic launch vehicle fails to account for the specific launch trajectory that a launch vehicle would utilize to enter the mission transfer orbit. Depending on the limitations on the duration of launch operations, the launch operators may opt for a less efficient launch trajectory and orbit insertion in order to minimize the duration of launch operations. For example, the orbit inclination may be shifted early in the launch instead of waiting until the launch vehicle reaches apogee. Directly injecting the spacecraft into the mission orbit would require a launch duration of approximately 10 hours. There are launch vehicles that are capable of directly injecting a payload into GEO orbit, a discussion with those teams would be needed to see if that can be done for this mission. Given these considerations, we opted for a direct launch to the mission apogee and assessed the C3 of our launch to be close to 0 km^2/s^2 at an inclination of 2° (26.4° inclination change). One interesting note about this mission is that additional mass margin may be obtained by increasing the inclination of the mission orbit. The inclination may shift to nearly 5° before impacting the mission science, providing an additional source of margin beyond what is provided in this paper.

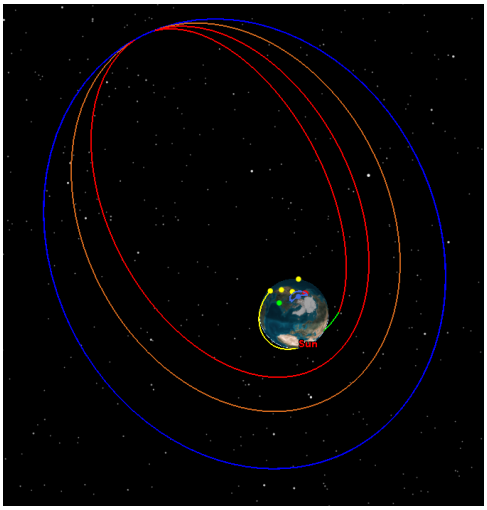

Figure A-8: A three-burn approach is recommended for raising the orbit perigee into the mission orbit.

The daughters will remain attached to the mothership until the mother has been inserted into its mission orbit. This will minimize the propellant needs of the daughters and keep their size smaller. This means the mother will need to perform launch vehicle separation, detumble, and mission orbit insertion with the daughters attached. The mother will execute a series of three perigee raise maneuvers of ~46 minutes in duration and □Vs between 258 and 337 m/s. To aid in this, the solar array is designed

to be partially deployed into a configuration that provides enough power for slewing and maneuvers without interfering with the daughters in their stowed configuration. Each Daughter will be released individually via lightband deployment since the stowed configuration precludes releasing in balanced pairs. The mothership will slew around its Z-axis to align the Daughter's separation impulse with the desired orbital phasing maneuver. Upon breakwire separation, the daughter will fire thrusters to spin up to the desired spin rate with the Sun Sensor Assembly in the loop. After achieving desired spin rate, Daughter will precess to align the spin axis with orbit normal and the mother will slew to the next deployment attitude.

A.3.4. Mother Orbit Maintenance

Corinne Lippe and Brent Duffy

The mothership's orbit, without correctional maneuvers, experiences drifts that adjusts the ground track. The drift over time is captured in Figure A-9, where the different colors represents the mothership and daughter spacecraft magnetic and orbit ground track. Due to the perturbing effects of the second degree and order sectoral gravity term and other higher order gravity harmonics, the resulting eastward longitudinal drift causes the ground track to depart from the desired ground track area in approximately 3 months.

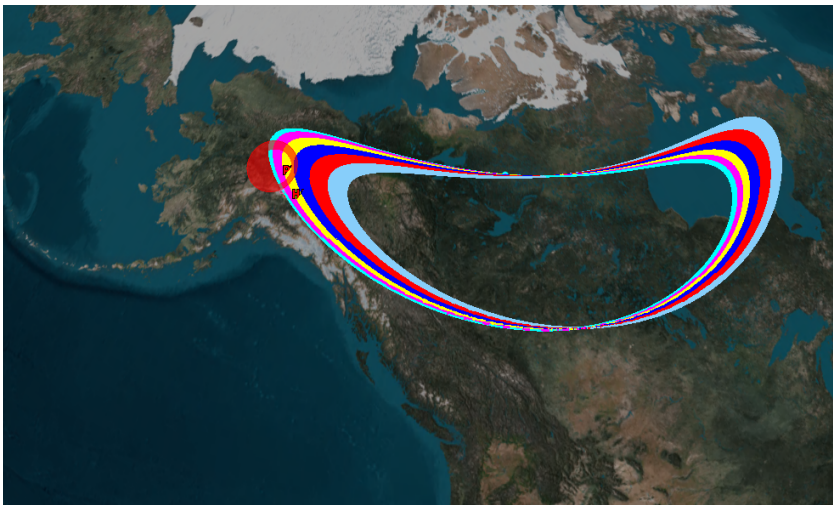

Figure A-9: Longitudinal drift of the mothership and daughter spacecraft due to higher order gravity harmonics. The ground track departs the desired target area of the ground track in approximately 3 months.

To overcome this longitude drift, a cost of 0.9 m/s in delta-v per month is required per spacecraft. The resulting ground track with this correction is presented in Figure A-10. This delta-v has been included in the budgeted value.

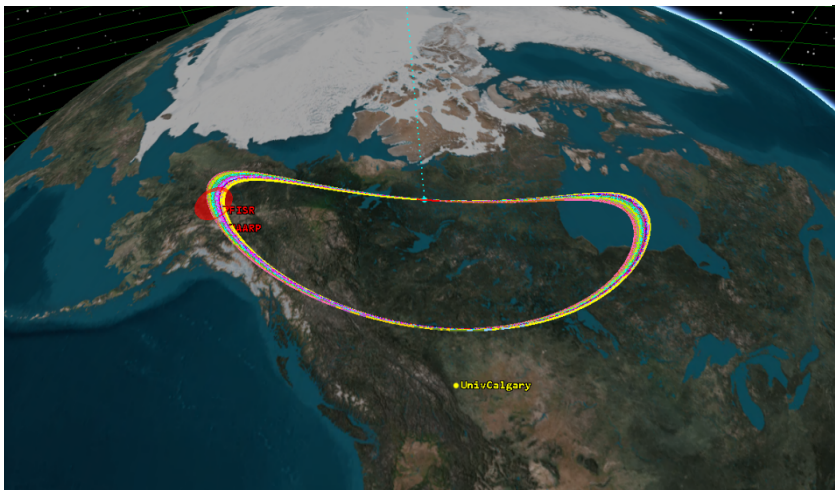

Figure A-10: Magnetic field and ground track of the mothership and daughter spacecraft when correctional maneuvers used. The ground track passes through the target ground track area when maneuvers totaling approximately 0.9 m/s per month per spacecraft are utilized.

A.3.5. Daughter Formation Design and Maintenance

Corinne Lippe

The four daughter spacecraft produced a formation with the relative motion in the orbital plane that resembled, as closely as possible with unforced motion, a 200 x 400 km ellipse with an approximate phasing of 90 degrees between the spacecraft that relies on in-plane safety. These trajectories were designed by leveraging the relative orbital element (ROE) representation from Chernick, Guffanti's (2021) collision avoidance conditions to ensure safe separation between the daughters and the mothership, and Lippe's mapping between the two formulations. The resulting relative motion over one orbit period is illustrated in Figure 1 in the local vertical local horizontal frame (LVLH). In this figure, R represents the radial direction, T represents the along-track direction, and the mothership remains at the origin.

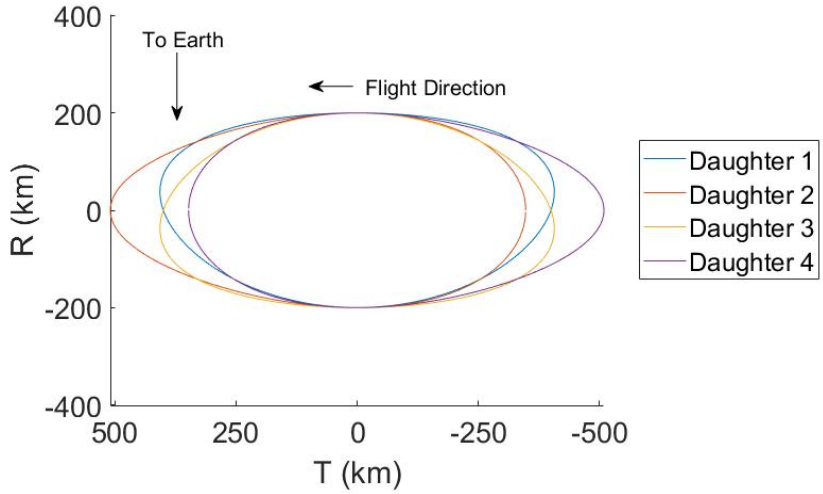

Figure 1. The relative motion with respect to the mothership produced by the four daughter spacecraft over one orbit period. R indicates the radial direction and T indicates the along-track direction. The Mothership exists at the origin of this frame over the entire orbit period.

However, the relative motion deviates from that presented in Figure 1 due to differential perturbations such as: solar radiation pressure (SRP), the second zonal harmonic of the Earth's gravity field (J_2), and third body effects from the Moon. These perturbations can create collision risks. Table 1 presents the maximum along track drift allowable until the daughter spacecraft pass within 1 km of the mothership. Due to the chosen relative orbits, the daughters risk collision with the mothership first before risking collision with each other. Consequently, the variation in the along-track motion is most restrictive when considering mother-daughter collision, so the drifts to create daughter-daughter spacecraft collisions are not provided.

Daughter	Along track drift
1	143 km
2	529 km
3	143 km
4	529 km

Table 1. The maximum along track drift allowed before the daughters risk collision with the mothership.

The aforementioned perturbations can create drifts that would risk the safety of the spacecraft. The dominant While the effects of J_2 and the Moon's third body effects are driven by the orbit of the mothership and the relative orbits of the daughters, the SRP influence is related to differential physical characteristics of the spacecraft. The effect of all of these perturbations are represented in Figure 3. Figure 2 divides the chosen ROE into planes (δa-$\delta \lambda_e$, δe_x-δe_y, and δi_x-δi_y). The definition of these ROE can be found in Chernick's work. Briefly, δa is related to difference in orbital relative semimajor axis between two spacecraft, $\delta \lambda_e$ is associated with the along-track drift, δe_x and δe_y are related to the in-plane relative motion magnitude, and δi_x and δi_y are related to the out-of-plane relative motion magnitude. Example perturbation of these ROE under the environmental effects for the different daughters are represented in Figure 2, where the variation induced by J_2 is represented in blue, the Moon's third body effects in red, and SRP in green. These variations are computed using models from Guffanti (2017) and Koenig.

As represented by Figure 2, the J_2 effects are the smallest of the perturbations but vary by each daughter. The Moon's third body effects have a non-negligible effect on the daughters' relative motion, and it influences the relative motion of the daughters differently. Finally, SRP effects the daughters similarly due to the expected similarity between the daughter spacecraft and dissimilarity between the daughter and mothership spacecraft. Consequently, the mothership can correct for these drifts, reducing the delta-v burden on the daughters. The accommodations for these perturbations have been included in the previously provided delta-v budget.

Unlike J_2 and the Moon's third body effects, the perturbation due to SRP is influences by the spacecraft physical properties. Specifically, the magnitude of the SRP perturbation is driven by the difference in the ballistic coefficient (δB) between spacecraft. This differential ballistic coefficient is proportional to the cross-sectional area of the spacecraft exposed to sunlight (A) and inversely proportional to the spacecraft mass (m).

The variation in the differential ballistic coefficient between the mother and daughter spacecraft drives the along-track drift induced by SRP and, consequently, the maneuver frequency and delta-v cost for formation maintenance. This is captured in Figure 2, which shows both the along-track drift induced by SRP given varying differential ballistic coefficients and the resulting delta-v cost for maintaining the relative motion. This cost contributes to the delta-v budget presented previously. These figures represent that certain differential ballistic coefficients are unsustainable given restricted delta-v. Furthermore, the along track (T-direction) drift at larger differential ballistic coefficients require too frequent maneuvers to ensure safe separation between the spacecraft at all times, inhibiting science objectives.

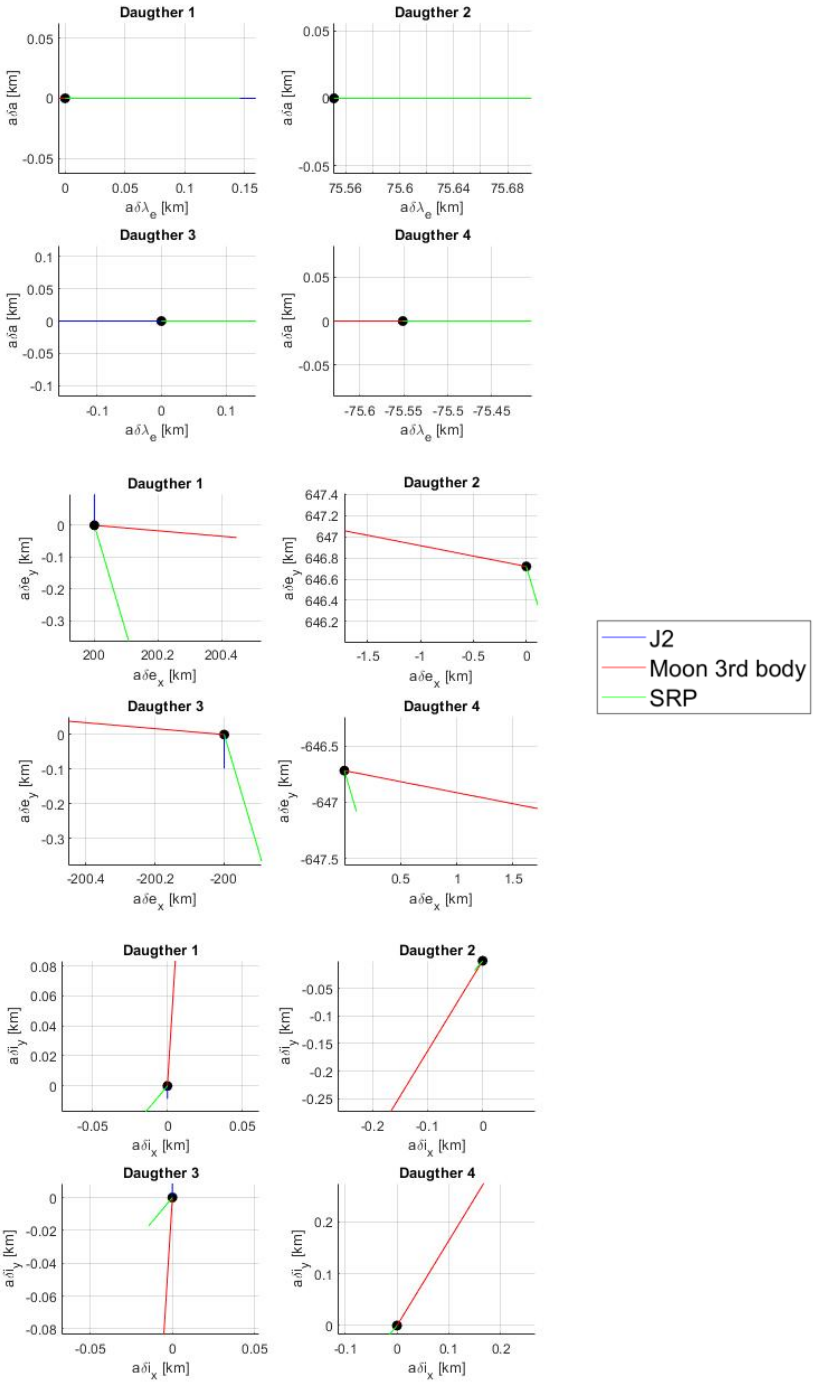

Figure 2. Example relative motion perturbation on the daughters, represented as variation in ROE, from J_2, the Moon's third body effects, and SRP per day.

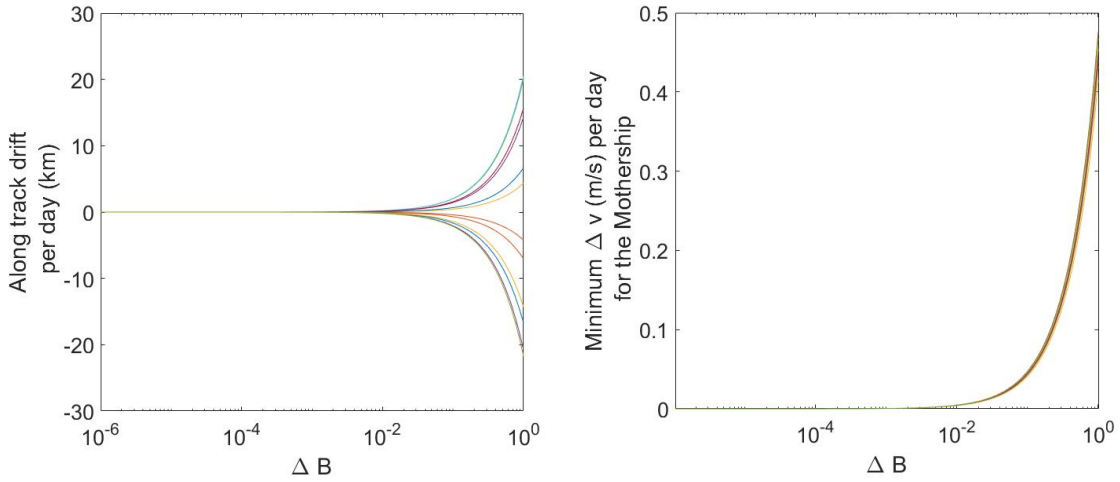

Figure 3. The delta-v cost given the differential ballistic coefficient between the mothership and daughter spacecraft. The delta-v cost is driven by the along track drift. Because the along track drift reduces the safe separation between the spacecraft, certain □B are unsustainable for accomplishing mission objectives.
Current estimates place □B at approximately 0.02, which is well within reasonable delta-v requirements. However, increases in the differential size between the mother and daughter spacecraft will result in increasing delta-v costs.

References:

Chernick, M., D'Amico, S. "Closed-Form Optimal Impulsive Control of Spacecraft Formations Using Reachable Set Theory," Journal of Guidance, Control, and Dynamics, Vol. 44, No. 1, pp. 25-44 (2021).

Guffanti, T., D'Amico, S. "Multi-Agent Passively Safe Optimal Control using Integration Constants as State Variables," AIAA Scitech 2021 Forum, Virtual Event, January 11-15 & 19-21 (2021).

Lippe, C., D'Amico, S. "Safe, Delta-v-Efficient Spacecraft Swarm Reconfiguration Using Lyapunov Stability and Artificial Potentials," Journal of Guidance, Control, and Dynamics, Vol. 45, No. 2, pp. 213-231 (2022).

Guffanti, T., D'Amico, S, Lavagna, M.. "Long-Term Analytical Propagation of Satellite Relative Motion in Perturbed Orbits," 27th AAS/ AIAA Space Flight Mechanics Meeting, San Antonia, Texas, February 5-9, 2017.

Koenig, A. W., Guffanti, T, D'Amico, S, "New state Transition Matrices for Spacecraft Relative Motion in Perturbed Orbits," Journal of Guidance, Control, and Dynamics, Vol. 40, No. 7, pp. 1749-1768 (2017).

A.3.6. Disposal

End-of-life disposal is designed to follow the disposal practices of GEO orbit regime. The table below shows the maneuver size required to dispose of the spacecraft based on a mission orbit with the same period as Geostationary orbits and an eccentricity listed on the X-axis of the figure below. The three disposal techniques evaluated are raising perigee to the GEO graveyard (GEO+300km), lowering apogee below GEO (GEO-300 km), and fully deorbiting the spacecraft. It should not be surprising that raising Perigee to the GEO graveyard was the most efficient with a maneuver size of 242 m/s for the mission orbit.

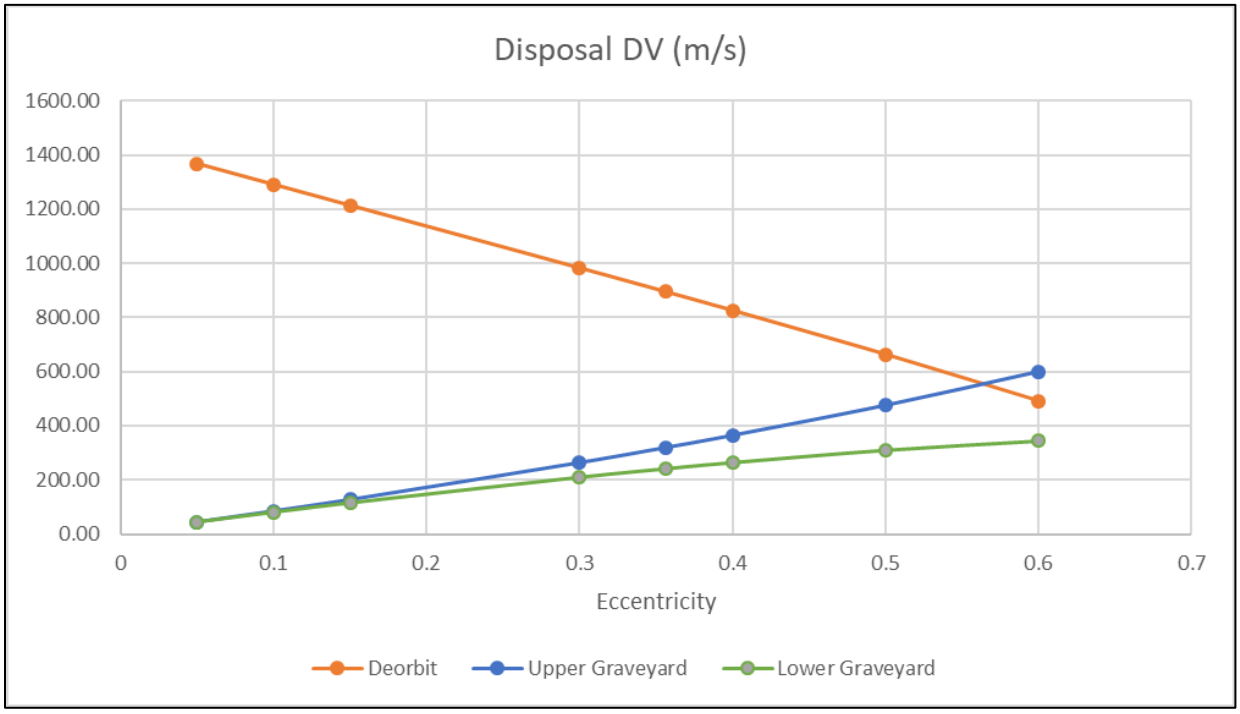

Figure A-11: Maneuver size for disposal at various orbit eccentricities.

End of life disposal places a fairly heavy burden on the daughtership design by adding large propulsion tanks and additional thrusters that need to be heated. It is unlikely that safe disposal can be accomplished without moving the daughters to a non-GEO-crossing orbit, but future studies can seek to modify the disposal maneuver operations for a simpler daughter design.

A.4. Space Environmental Effects overview

Justin Likar

Initial, proposed environments and derived requirements have been developed for Total Ionizing Dose (TID), Total Non-Ionizing Dose (TNID), Single Event Effects (SEE), and spacecraft charging (both surface charging and internal charging).

1.1 Trapped Particle populations

The baseline operating orbit for the MIO mission ($4.3\ R_e \times 9.0\ R_e$) places the spacecraft between ~20,000 km and ~50,000 km (Fig. 1). At these altitudes, and near-zero inclination, the spacecraft will spend significant time in the Outer Van Allen Belt. Trapped particle populations were determined via IRENE Ver. 1.50.00 run in both Monte-Carlo mode, which includes uncertainties and variabilities associated with measurements, gap-filling, and space weather processes as well as Perturbed Mean mode. The latter excludes space weather variability. A Confidence Level (CL) of 95% was used as was a total of 40 scenarios.

1.2 Orbit environment (TID & TNID)

Persistent exposure to ambient radiation, be it magnetospheric trapped electrons or protons, the solar wind, Solar Particle Events (SPE), or Galactic Cosmic Rays (GCR) contribute to a variety of undesirable cumulative radiation effects in EEE (Electrical, Electronic, and Electromechanical) devices and materials. The primary effect being the gradual degradation in EEE device performance as a function of accumulated dose. EEE devices, including those so-called "radiation tolerant" or "radiation hardened" devices are subject to gradual performance loss in specific electrical parameters due to Total Ionizing Dose (TID) and / or Total Non-Ionizing Dose (TNID) although the specific mechanisms differ.

Although TID and TNID are characterized as cumulative effects, non-destructive in their own rights, the continued slow degradation of a particular electrical property or EEE device

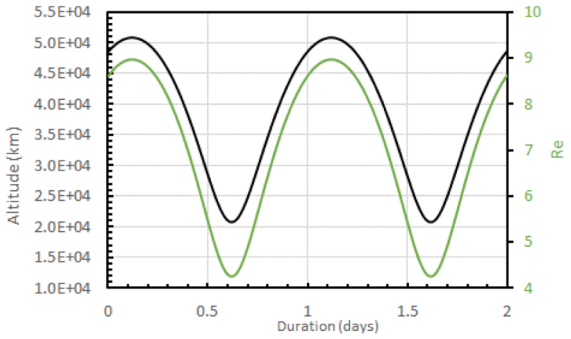

Figure 1. *The baseline operating orbit results in a significant time spent in the Outer Van Allen Belt.*

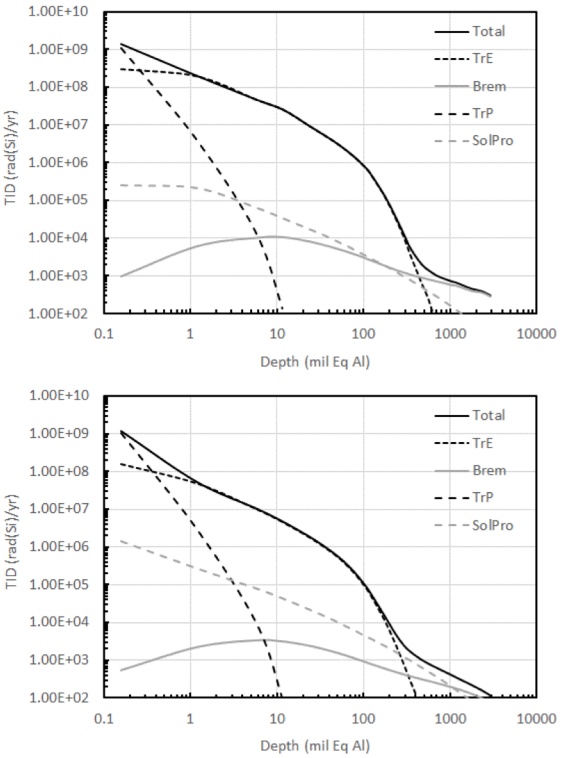

Figure 2. *Top panel presents Solid Sphere Dose (rad(Si)/yr vs Depth (mil equivalent aluminum) for the baseline operating orbit; bottom panel the Spherical Shell results.*

may eventually result in the permanent failure of the device or the higher level circuit or function reliant upon the device. Similarly the cumulative degradation in critical materials may result in undesirable changes in functionality-critical properties such as reflectance, absorptance, electrical conductivity, dielectric constant, and so on. The effect itself is likely non-destructive however, over time, the higher level systems reliant upon such properties are likely to degrade in performance.

Trapped electron and trapped proton fluences were used, along with the Solar Proton fluence determined using the ESP-PSYCHIC model at CL95, to generated predicted dose-depth plots (Fig. 2). The dose-depth plot represents predicted Total Ionizing Dose (TID) and Total Non-Ionizing Dose (TNID) as a function of equivalent aluminum shielding depth. Note that the TNID vs. depth curves are not provided herein as TID is expected to be design driver. All curves were generated using NOVICE for multiple kernels; both Solid Sphere (SoSp) and Spherical Shell (SpSh) kernels are shown in Fig. 2.

In approximate numbers it is observed that the annual dose behind 100 mil equivalent aluminum (2.54 mm) is ~280 krad/yr (SoSp) or ~90 krad/yr (SpSh) whilst the dose behind 300 mil equivalent aluminum (7.62 mm) is ~5 krad/yr (SoSp) or ~2.5 krad/yr (SpSh). Resultant values for a 2-year operational mission are ~560 krad (100 mil) (SoSp) or ~180 krad (SpSh) and ~10 krad (300 mil) (SoSp) or ~5 krad (SpSh) respectively.

Predicted mission dose levels can be satisfied by a combination of shielding and prudent EEEE part selection for both the flight systems and payloads. Certainly there, now, exists a preponderance of Radiation Hardened (RH) devices to levels of 300 krad and above however localized "spot" shielding and some amount of upscreening and / or RLAT should be anticipated.

Surface doses – those in thin-film coatings, paints, films, and other materials directly exposed to space – will exceed 1 Grad/yr.

1.3 Single Event Effects (SEE)

Passage of a single particle (e.g. proton, ion, neutron) can induce undesirable effects in sensitive EEE devices. Effects resulting from single particles are termed Single Event Effects (SEE) or Single Event Phenomena (SEP); these effects may be immediately catastrophically destructive in nature.

The specific nature of Destructive Single Event Effects (DSEE) is determined by target (victim) device type. CMOS and BiCMOS devices or those with CMOS structures therein are susceptible to Single Event Latchup (SEL) whilst Power MOSFETs and power transistors are susceptible to Single Event Gate Rupture (SEGR) and Single Event Burnout (SEB) respectively. Although detailed mechanisms of these failures are beyond the scope of this particular document it is paramount to recognize that these effects impart a level of risk to successful operations given that only a single particle can cause a permanently disabling effect in the victim device. Although, fundamentally, DSEE sensitivities exist in "radiation hardened", "radiation tolerant", and commercial devices the process control and traceability associated with the former device types offer substantially increased robustness over commercial devices.

Application specifics such as circuit filtering, impedances, operating frequencies, scrub rate, et cetera also influence, but not totally determine, the ultimate risk associated with a series of Non-Destructive SEE (NDSEE) including but not limited to Single Event Transients (SET), Single Event Upset (SEU), Single Bit Error (SBE), Multiple Bit Error (MBE), and Single Event Functional Interrupt (SEFI). Specific SEE sensitivities are determined by part type / technology. Sensitivities are found in most modern microelectronics such as microprocessors, microcontrollers, FPGAs, memories (SRAM, SDRAM, DRAM, Flash), DAC, ADC, logic devices, and linear devices.

SEE result from charge deposition in a target device "sensitive volume" by a charged particle (such as proton or ion) or a neutron. Mechanisms of charge generation include direct ionization (e.g. by the incident particle) or indirect ionization whereby the incident particle interacts with target materials (often device packaging, interconnects, and substrate materials) and creates secondary particles. GCR are known to generate SEE as are SPE

ions and protons, magnetospheric trapped protons, and neutrons.

The baseline MIO operating orbit renders SEE a relevant, though not driving hazard or concern. The operating orbit is well above the proton-dominated Inner Van Allen Belt and South Atlantic Anomaly. For purposes of assessing SEE it may be considered beyond the magnetosphere, and hence, experiencing little or no magnetospheric shielding from the solar wind, SPE, and GCR wherefore unshielded environments at 1 AU would comprise the baseline design environments. This is the same approach commonly applied to commercial GEO telecommunications missions and missions at the Lagrange points.

1.4 Spacecraft Charging

Spacecraft charging describes the series of hazards associated with the charging of spacecraft materials and / or the spacecraft itself by its immersion in plasma environments. It is frequently, and conveniently, sub-divided into hazards associated with the charging of materials and surface directly exposed to space (exterior surfaces) and those which are not directly exposed to space (interior surfaces). We term these effects Surface Charging and Interior Charging respectively. Ultimately the risk to operations is due to Electrostatic Discharges (ESD) that occur when breakdown thresholds are exceeded. Electrostatic breakdown may occur in insulators or dielectrics such as wire insulation or conformal coating. Or electrical breakdown may occur in vacuum due to differential charging of surface materials.

Surface charging results from charge (positive or negative) accumulation on external surface in direct contact with the surrounding plasma environment. It is driven by low-energy plasmas (electrons and ions) and influences the absolutely potential of the spacecraft - potential difference between the spacecraft frame and surrounding plasma. It also may create differential potentials on the spacecraft body – large potential gradients between adjacent or nearby surfaces. The potential at which a spacecraft or spacecraft surface sits relative to its surroundings is determined by a current balance of all incoming and outgoing currents. Specifically incoming electrons and ions and outgoing electrons and ions. Outgoing currents result from phenomena such as secondary electron emission, backscattered electron emission, and photoelectron electron emission. It is known that these properties are functions of temperature, contamination, radiation, et cetera. Uncertainty in these values propagates to uncertainty in the ultimate surface potential and risk of ESD. Variations in surface potentials can be quite extreme owing to the characteristic time scales associated with solar wind or magnetospheric plasmas.

ESD on the surface causes a number of undesirable effects including RF noise (EMI) and accelerated materials degradation via contamination and sputtering / redeposition. Surface ESD has proven particularly destructive for missions with include photovoltaic arrays (see subsequent paragraph below). Surface ESD also creates a risk of discharges coupling into cables and wires routed across the discharging surface. Energy which couples into wire conductors or shields (grounds) poses a risk to the interfacing electronics.

The operating accelerator on the Primary spacecraft creates a more complex surface charging scenario. In addition to the accelerator the mission includes several other payload elements moderately influence by surface charging (EFW and EDI). The instruments are "tolerant" to potential fluctuations but prudent analyses / verification is necessary to ensure accommodations are managed.

During periods of accelerator operation it strongly dominates the current balance and resultant spacecraft potentials. Initial, albeit idealized, assessments performed by LANL suggest that spacecraft operations and survival may be ensured by inclusion and satisfactory operation of a Plasma Contactor System (PCS).

An operating PCS influences the spacecraft floating potential by emitting a plasma – typically xenon. The emitted plasma is not a focused or columated "plume" but is likely to include ions of energies approaching keeper and anode voltages (typically several hundred eV). Such ions are capable of sputtering exterior surface materials, coatings, films, et cetera. Sputtered and redeposited material create modified surface properties and may be a surface charing, thermal, optical, or contamination related risk if not mitigated (e.g. by use of a baffle or deflector shield near the PCS). Ultimate verification of such mitigation would be strongly improved by characterization of the PCS plasma (energies, densities, …) in the far field regions (angles >90 deg).

PCS plasma densities of $>10^6$ #/cm^3 are expected, along with small electron and ion temperatures. These values are comparable to those of the ionospheric plasma. Should they be present in the vicinity of the operating 100 V solar array then unacceptable leakage currents may present. Further, it may cause electrostatic discharges on the array in the form of Primary Arcs and Secondary Arcs. The baseline MIO solar array includes grout as well as a controlled, purpose designed string / circuit layout for delta-V, string blocking diodes, back side charge dissipative coatings, and grounded ITO on the coverglasses.

Complete analytical and empirical verification is recommended. Analytical assessments to include a simulation of the operating accelerator, operating PCS, realistic spacecraft geometries, realistic spacecraft material properties, and both nominal and worst-case environment conditions. A tailored system level test is also recommended, wherefore verification is not solely reliant on analytical results. Such a tailored system level test should include an operating accelerator, operating PCS, flight grounding, and at least portions of a flight-like solar array and realistic locations. It is a non-trivial test requiring highly specialized vacuum chamber capabilities.

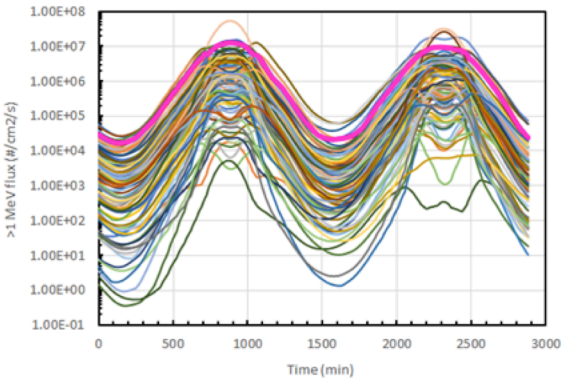

Figure 3. *Overlay of 100 Monte-Carlo scenarios of >1 MeV electron flux as function of orbit time.*

Internal (spacecraft) charging is associated with charging accumulation in, and potential breakdown of, interior dielectrics. Oftentimes these dielectrics are extremely resistive (bulk resistivities $>10^{19}$ ohm-cm) and in immediate proximity to electronics or wires, pins, contacts, et cetera which connect to sensitive electronics. Owing to their high resistivities many interior dielectrics exhibit charging time constants of days to months or even years. MIO considers both "Peak Flux" charging and "Quiet" or "Mean" flux charging to ensure mitigation against extreme events and long-duration exposure to nominal, or quiet time electrons.

Fig. 3 presents an overlay of 100 IRENE Monte-Carlo scenarios of >1 MeV electron flux over two orbits illustrating the variability due to space weather. The heavy pink line reflects the CL95% flux. The proposed "Peak Flux" environment (Fig. 4) considers a CL95% flux over a finite time period. Initial assessments of time returned a value of ~6.5 hr for the >1 MeV flux to drop to a value of $1/e$ however owing to uncertainty we propose a more familiar 10 hr value (e.g. CRRES) for initial assessments and reviews.

The resultant "Peak Flux" spectrum is compared to other, Outer Belt missions and GEO / MEO design guidelines in Fig. 4. The proposed MIO environment is slightly more severe than GEO design guidelines but less so then project specific environments /

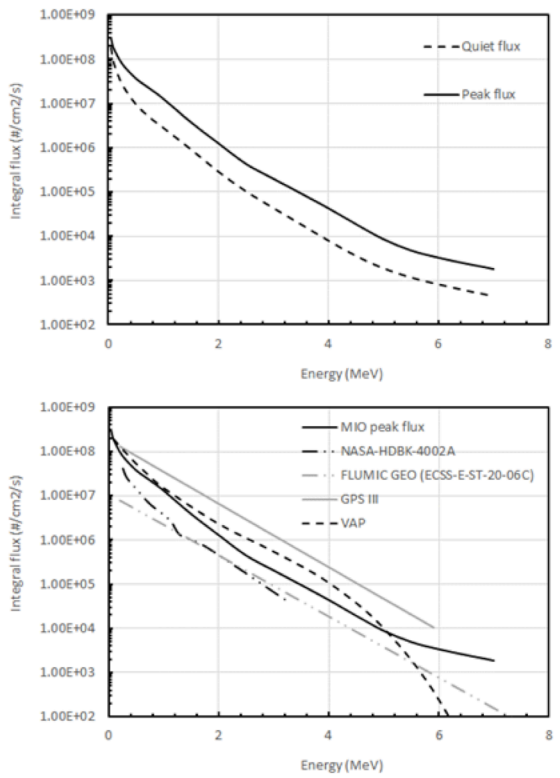

Figure 4. *Top panel depicts the derived "Peak flux" and "Quiet flux" environments for the MIO operating orbit whilst bottom panel compares the Peak flux environment to other missions or design standards relevant to the Outer Belt.*

requirements developed for missions such as GPS-III or VAP.

Internal charging ESD, or so-called IESD, may be immediately catastrophic to the interfacing electronics or circuits as the energies released by or peak currents / voltages associated with IESD events can be very high (mJ for example). These energies, or currents / voltages, may immediately destroy an EEE device. Alternatively IESD may also produce nuisance transients which may appear as "noise" on signal lines. Although not permanently disabling themselves this transients and their rate of occurrence may prove an unwelcome effect depending on the criticality of the victim circuit / function.

MIO to baseline IESD mitigation practices adopted for VAP and recent missions to the Jovian system (Europa Clipper and Juno for example). This includes a combination of (1) ellimiate the occurance of ESD and (2) verify that ESD (largest and / or repeating events) cannot damage or degrade system performance. Application of this approach includes design features such as shielding, complete elimination of ungrounded / floating metal, hardened First Circuit Interfaces (FCI), and ESD testing of EEEE devices (e.g. MIL-STD-883 TM 3015.7). Initial, quick-look calculations performed considering 0026S1664 Cheminax balanced impedence wires with XL-ETFE insulators indicates that only moderate shielding (50 mil equivalent aluminum beneath MLI) maybe required to mitigate charging in wires / cables. These initial results are specific to wires / cables but such shielding is less than required for Europa Clipper and less than that implemented on VAP.

A complete verification process likely also to include detailed 3D internal charging modeling, Monte-Carlo transport modelling, accelerator testing and creation / adoption of a robust ESD Working Group and Control Plan.

A.5. Payload Summary Tables

A.5.1. Accelerator

Table A-3: Accelerator Data Summary Table

Item	Value	Units
Type of instrument	Electron Accelerator	
Size/dimensions (for each instrument)	Accelerator: 2.47 x 0.54 x 0.14 HVPS: 0.33 x 0.23 x 0.10 Control electronics: 0.41 x 0.38 x 0.19	m x m x m
Mass **without** contingency (CBE*)	Accel: 126.6 kg HVPS: 4.5 kg Control Electronics: 8.3 kg	Kg
Mass contingency	15	%
Mass **with** contingency (CBE+Reserve)	Accel: 145.5 kg HVPS: 5.2 kg Control Electronics: 9.5 kg	Kg
Average payload power **without** contingency	Pulsing Average: 225 W Pulse Peak: 13.34 kW	W
Average payload power contingency	10	%
Average payload power **with** contingency	Pulsing Average: 248 W Pulse Peak: 15.35 kW	W
Engineering Data rate **without** contingency (no science data)	1.23 orbit average 224 peak diagnostic rate 22 nominal peak rate	kbps
Fields of View (if appropriate)	Beam can be steered ± 10°	degrees
Pointing requirements (knowledge)	0.1	degrees
Pointing requirements (control)	Within 0.5° of local B-Field line	degrees
Pointing requirements (stability)	0.5	deg/sec
Thermal Operational	Accelerator: 25 ± 5 Electronics: 20 ± 20	C
Thermal Survival	-20 to 50	C

A.5.2. Plasma Contactor (PCS)

Table A-4: PCS Data Summary Table

Item	Value	Units
Type of instrument	Electric Propulsion	
Size/dimensions (for each instrument)	0.51 x 0.3 x 0.25	m x m x m
Mass	23 CBE (26.45 MEV, 15% cont.)	Kg
Average payload power **without** contingency	Transient peak: 660 Engagement avg: 248	W
Average payload power contingency	10	%
Average payload power **with** contingency	Transient peak: 726 Engagement avg: 273	W
Engineering Data rate **without** contingency (no science data)	0.168 orbital average 5.1 nominal peak rate	kbps
Fields of View (if appropriate)	Hemispherical Keep-Out for plasma plume	degrees
Pointing requirements	N/A	

A.5.3. Electron Drift Instrument (EDI)

Table A-5: EDI Data Summary Table

Item	Value	Units
Type of instrument	Electron emitter/detector	
Number of channels	32	
Size/dimensions (for each instrument)	0.415 x 0.221 x 0.219	m x m x m
Mass **without** contingency (CBE*)	GDU: 11.9 Elect: 2.35	Kg
Mass contingency	15	%
Mass **with** contingency (CBE+Reserve)	GDU: 12.55 Elect: 2.35	Kg
Average payload power **without** contingency	GDU: 8.5 Elect: 3.12	W
Average payload power contingency	15	%
Average payload power **with** contingency	GDU: 9.8 Elect: 3.6	W
Average science data rate **without** contingency	1.572	kbps
Fields of View (if appropriate)	100	degrees
Pointing requirements (knowledge)	Detector to Optics: 0.6 GDE to S/C: 0.1 Gun to FGM: 0.5	degrees
Pointing requirements (control)	1	degrees
Pointing requirements (stability)	1	deg/sec

A.5.4. Flux-Gate Magnetometer (FGM)

Table A-6: FGM Data Summary Table

Item	Value	Units
Type of instrument	Magnetometer	
Number of channels	3	
Size/dimensions (for each instrument)	0.14 x 0.076 x 0.137	m x m x m
Mass **without** contingency (CBE*)	3 (incl. boom)	Kg
Mass contingency	15	%
Mass **with** contingency (CBE+Reserve)	3.45 (incl. boom)	Kg
Average payload power **without** contingency	2.5	W
Average payload power contingency	15	%
Average payload power **with** contingency	2.9	W
Average science data rate **without** contingency	Average: 0.928 Burst: 6.304	kbps
Pointing requirements (knowledge)	0.1 FGM to EDI Gun 0.5	degrees
Pointing requirements (control)	1	degrees
Pointing requirements (stability)	1	deg/sec

A.5.5. Electric Field Waves (EFW)

Table A-7: EFW Data Summary Table

Item	Value	Units
Type of instrument	Electron density and temperature	
Number of channels	111 (per axis)	
Size/dimensions (for each instrument)	2, 7m stacers	m x m x m
Mass **without** contingency (CBE*)	3.58	Kg
Mass contingency	15	%
Mass **with** contingency (CBE+Reserve)	4.12	Kg
Average payload power **without** contingency	2.70	W
Average payload power contingency	15	%
Average payload power **with** contingency	3.11	W
Average science data rate **without** contingency	Average: 7.5 Burst: 2.4 Mb per accelerator firing Max: 16.5	kbps
Pointing requirements (knowledge)	1	degrees
Pointing requirements (control)	1	degrees
Pointing requirements (stability)	1	deg/sec

A.5.6. Magnetometer (Daughter)

Table A-8: Daughter Magnetometer Data Summary Table

Item	Value	Units
Type of instrument	Mag.	
Number of channels	3	
Size/dimensions (for each instrument)	3.5 x 6.1 x 3.6	cm x cm x cm
Mass	1.13 CBE (1.31 MEV, 15% cont.)	Kg
Average payload power	2.9 CBE (3.34 MEV, 15% cont.)	W
Average science data rate **without** contingency	0.105 (1.2 kb per spin, 12s per spin)	kbps
Pointing requirements (knowledge)	Spin axis known to 5°	degrees

A.5.7. Electrostatic Analyzer (ESA)

Table A-9: ESA Data Summary Table

Item	Value	Units
Type of instrument	Electrostatic Analyzer	
Number of channels	32	
Size/dimensions (for each instrument)	18.4 x 19.3 x 15.4	cm x cm x cm
Mass	3 CBE (3.45 MEV, 15% cont.)	Kg
Average payload power	2 CBE (2.3 MEV, 15% cont.)	W
Average science data rate **without** contingency	1.877 (22.5 kb per spin, 12s per spin)	kbps
Pointing requirements (knowledge)	Spin axis known to 5°	degrees

A.6. Flight System Summary Tables

A.6.1. Mothership

Table A-10: Mothership Summary Table

Flight System Element Parameters	Value/ Summary, units
General	
Design Life, months	24
Structure	
Structures material	Machined aluminum cylinder and 1" thick aluminum honeycomb.
Number of articulated structures	0
Number of deployed structures	1 Solar Array, 2 stacers, 1 Boom, 4 Daughter Spacecraft
Thermal Control	
Type of thermal control used	Passive with radiators and thermostat controlled heaters. Heat pipes in accelerator.
Propulsion	
Estimated delta-V budget, m/s	1334 (includes 15% margin)
Propulsion type(s) and associated propellant(s)/oxidizer(s)	Pressurized monoprop system with hydrazine
Number of thrusters and tanks	12 - 4.4 N thrusters, 4 - 22 N thrusters, 1 - propellant tank (ATK 80507-3), 1 - pressurant tank
Specific impulse of each propulsion mode, seconds	220 s
Attitude Control	
Control method	3-Axis
Control reference (solar, inertial, Earth-nadir, Earth-limb, etc.)	Local B-field and solar. Data Collection: Arrays pointed directly to the sun with bus rotated so that the B-field is normal to the EDI electron beams. Accelerator operations: Accelerator aligned with local B-field with bus rotated to maximize sun on array.
Attitude control capability, degrees	< 0.5 deg
Attitude knowledge limit, degrees	< 0.1 deg
Agility requirements	< 0.5 deg/s (driven by slew duration for maneuver)
Articulation/#–axes	No articulation
Sensor and actuator information (precision/errors, torque, momentum storage capabilities, etc.)	Sensors: 1 Star Tracker, 1 MIMU, Sun Sensors (1 SSE, 6 DSSH), 1 GPS Actuators: 4 Reaction Wheels (2 Nms), 8 ACS thrusters (5 N).
Command & Data Handling	
Flight Element housekeeping rate, kbps	1
Data storage capacity, Mbits	32,000
Maximum storage record rate, kbps	1,530 (30.6 Avg.)
Maximum storage playback rate, kbps	5,000
Power	
Type of array structure (rigid, flexible, body mounted, deployed, articulated)	Deployed array with four, rigid panels, fixed orientation. Full grout / dissipative design similar to Van Allen Probes
Array size, meters x meters	4, 1.22 x 1.27 m panels (only 2 panels deployed for insertion)
Solar cell type	Triple Junction GaAs, 6 mil CMG coverglass with ITO
Expected power generation, watts	705 (Insertion), 1,410 (BOL), 1,184 (EOL)
On-orbit average power consumption, watts	659 OAP (CBE), 859 (CBE avg. during accelerator ops)
Battery type	Li-ion
Battery storage capacity, amp-hours	147 (201 A peak discharge rate)

A.6.1.1. Mothership Space Vehicle Operating Modes

The team defined a notional set of operating modes for the MIO mission along with a state machine that provide some insight into how the different pulsing operations and daughtership coordination can be achieved with a fairly straightforward architecture.

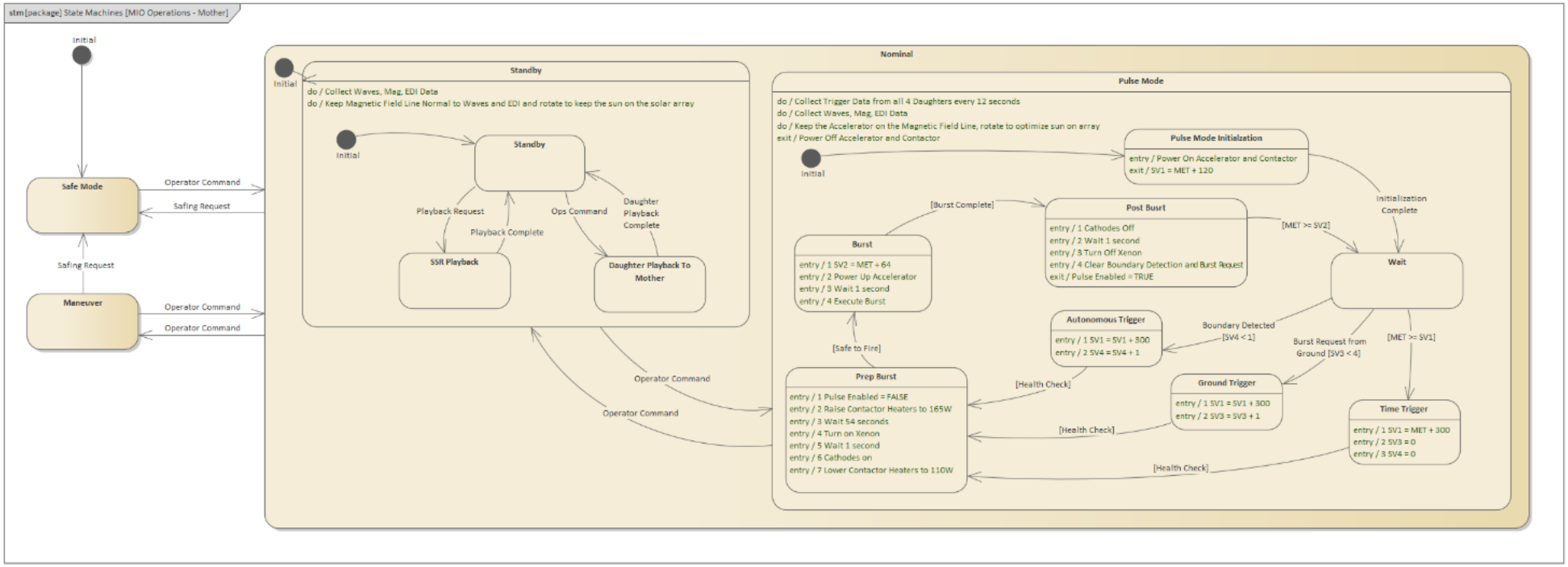

Figure A-12: Mothership Space Vehicle Operating Modes

A.6.1.2. Mothership Space Vehicle Block Diagram

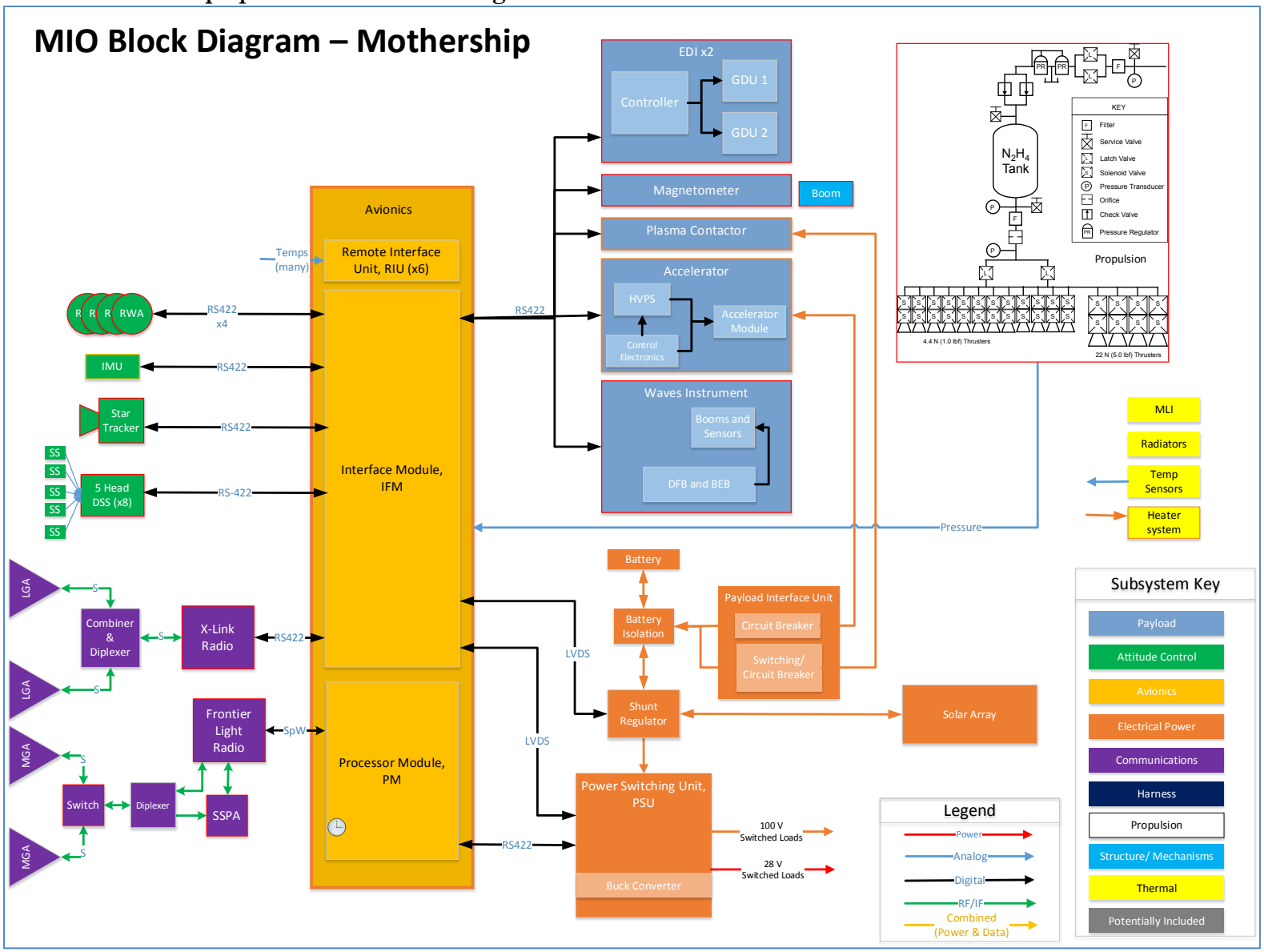

Figure A-13: Mothership Space Vehicle Block Diagram

A.6.1.3. Mass & Power Resources

Table A-11: Mothership Mass and Power Resources

Mothership Mass Summary			
Stage/Subsystem	**CBE (kg)**	**Cont. (%)**	**MEV (**
Flight System Dry Mass	849.30	13%	963.0
Instruments	181.13	15%	208.3
Mechanical	241.00	15%	277.1
Propulsion	94.68	2%	96.8
Avionics	21.96	15%	25.2
Power	187.00	15%	215.0
GNC	27.00	15%	31.0
Thermal	22.64	15%	26.0
RF	7.35	8%	7.94
Harness	66.53	13%	75.4
TOTAL DRY MASS	**849.30**	**13%**	**963.0**
DRY MASS WITH MARGIN	**-**	**30%**	**1104.**
Flight System Consumable Mass	881.76	-	881.7
TOTAL WET MASS	**1731.06**	**-**	**1844.**
Fuel Fraction		**48%**	
Allocated Mass Margin		**13%**	

Mothership Power Summary						
Stage/Subsystem	**Pulsing CBE (W)**	**Cont. (%)**	**Pulsing MEV (W)**	**Not Pulsing CBE (W)**	**Cont. (%)**	**Not Pulsing MEV (W**
Flight System Total	**876.8**	**12%**	**983.9**	**448.8**	**15%**	**515.4**
Instruments	488.4	10%	537.2	15.4	10%	16.9
Mechanical	0.0	0%	0.0	0.0	0%	0.0
Propulsion	16.2	15%	18.6	16.2	15%	18.6
Avionics	23.5	15%	27.0	23.5	15%	27.0
Power	46.0	15%	52.9	46.0	15%	52.9
GNC	160.4	15%	184.5	160.4	15%	184.5
Thermal	75.0	15%	86.3	120.0	15%	138.0
RF	53.6	15%	61.6	53.6	15%	61.6
Harness	13.7	15%	15.8	13.7	15%	15.8

A.6.2. **Daughtership**

Table A-12: Daughtership Summary Table

Flight System Element Parameters	Value/ Summary, units
General	
Design Life, months	24
Structure	
Structures material	0.5-1" thick aluminum honeycomb.
Number of articulated structures	0
Number of deployed structures	2 Booms (mag and antenna)
Thermal Control	
Type of thermal control used	Passive with radiators and thermostat controlled heaters.
Propulsion	
Estimated delta-V budget, m/s	366 (includes 15% margin)
Propulsion type(s) and associated propellant(s)/oxidizer(s)	Blowdown monoprop with hydrazine
Number of thrusters and tanks	12 – 4.4 N thrusters, 2 - propellant tanks (ATK 80444)
Specific impulse of each propulsion mode, seconds	220 s
Attitude Control	
Control method	Spinner (5 RPM, spin-axis normal to orbit plane)
Control reference (solar, inertial, Earth-nadir, Earth-limb, etc.)	Solar
Attitude control capability, degrees	Spin-axis controlled to 5 deg.
Attitude knowledge limit, degrees	Spin-axis knowledge to 1 deg.
Sensor and actuator information (precision/errors, torque, momentum storage capabilities, etc.)	Sensors: Sun Sensors (1 SSE, 2 heads), 1 GPS Actuators: 2 passive nutation dampers, 12 ACS thrusters (8 radial, 4 axial).
Command & Data Handling	
Flight Element housekeeping rate, kbps	0.33
Data storage capacity, Mbits	32,000
Maximum storage record rate, kbps	2.3
Maximum storage playback rate, kbps	100
Power	
Type of array structure (rigid, flexible, body mounted, deployed, articulated)	Body-mounted panels on 7 of 8 side faces. Full grout / dissipative design similar to Van Allen Probes
Array size, meters x meters	7, 0.37 x 0.38 m panels
Solar cell type	Triple Junction GaAs, 6 mil CMG coverglass with ITO
Expected power generation, watts	72 (BOL), 61 (EOL)
On-orbit average power consumption, watts	46.4 (CBE)
Battery type	Li-ion
Battery storage capacity, amp-hours	12

A.6.2.1. Daughtership Space Vehicle Block Diagram

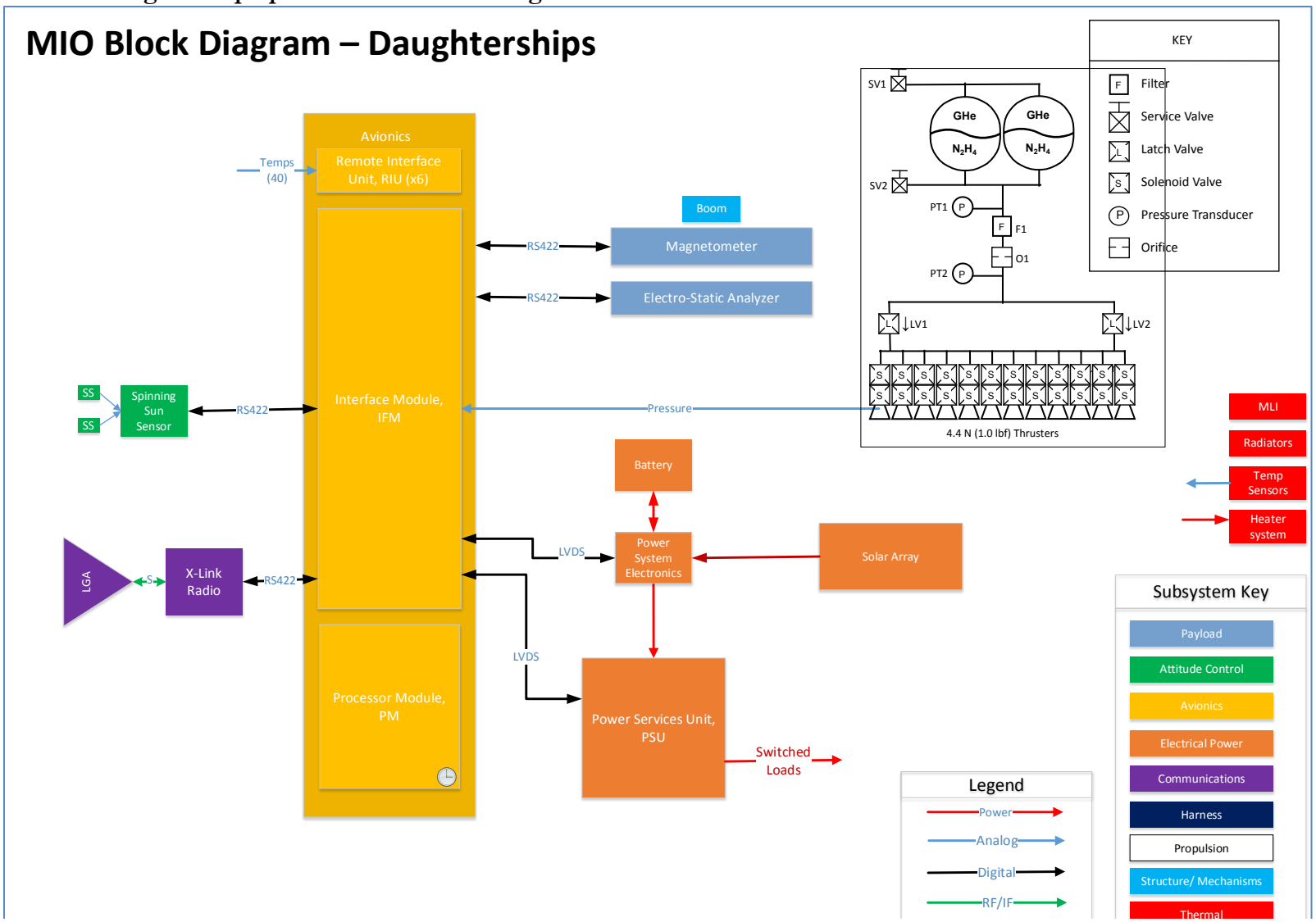

A.6.2.2. Mass & Power Resources

Table A-13: Daughtership Mass and Power Resources

Daughtership Mass Summary				Orbit Average Power [		
Stage/Subsystem	**CBE (kg)**	**Cont. (%)**	**MEV (kg)**	**CBE (W)**	**Cont. (%)**	**M**
Flight System Total	**68.78**	**13%**	**77.39**	**46**	**15%**	
Instruments	5.27	15%	6.06	6.5	15%	
Mechanical	14.00	15%	16.10	0	15%	
Propulsion	12.27	2%	12.47	13.9	15%	
Avionics	18.40	15%	21.16	13.9	15%	
Power	4.99	15%	5.74	1.4	15%	
GNC	7.06	15%	8.12	3.3	15%	
Thermal	0.66	15%	0.76	2	15%	
RF	3.48	15%	4.00	3.7	15%	
Harness	2.65	13%	2.98	1.3	15%	
TOTAL DRY MASS	**68.78**	**13%**	**77.39**			
DRY MASS WITH MARGIN	**-**	**30%**	**89.41**			
Flight System Consumable Mass	17.19	-	17.19			
TOTAL WET MASS	**85.97**	**-**	**94.58**			
Fuel Fraction	**18%**					
Allocated Mass Margin	**13%**					

A.6.3. Launch Mass

Table A-14: Launch Mass Roll-Up

Mothership	1	Qty
Mass **with** contingency (includes instruments)	963	kg
Propellant Mass **without** contingency	767	kg
Propellant contingency	15	%
Propellant Mass **with** contingency	882	kg
Daughtership	4	Qty
Mass **with** contingency (includes instruments)	77	kg
Propellant Mass **without** contingency	15	kg
Propellant contingency	15	%
Propellant Mass **with** contingency	17	kg
Launch		
Launch Adapter Mass **with** contingency	50	kg
Total Launch Mass	2,749	kg
Launch Vehicle	2	Type
Launch Vehicle Lift Capability	3,300	kg
Launch Vehicle Mass Margin	551	kg
Launch Vehicle Mass Margin (%)	16.6	%

A.7. Integration and Test

The reference design has the mother following a traditional I&T flow with vibration and TVAC/TBAL. The daughters will be integrated in phases with the first daughter being integrated early followed by proto-flight testing for design and verification (thermal balance, mechanical design, EMI/EMC). The other three daughters will be acceptance tested to appropriate level of workmanship verification demonstrating the SC was mechanically and electrically integrated successfully (thermal balance not performed, vibration limited to single axis vibe or acoustics, no EMI, spin balance at launch site). The goal is to complete I&T of the first daughter by the time I&T begins for the mother. This approach provides an opportunity to identify and mitigate common mode issues in the daughters before most of them are integrated. It also provides an avenue for mitigating any interface issues between the mother and daughters before the mother is integrated. There is an open trade whether or not to perform mothership vibration testing with the flight daughters or test masses. At the end of I&T, a set of RF compatibility tests needs to be performed to check NEN connectivity as well as crosslink operations.

Further work needs to be done to evaluate the extent to which accelerator operations can be tested on the ground. Performing a full system self-compatibility test with the accelerator may require a large environmental chamber and/or extensive GSE to capture and remove the electrons/plasma before they can bounce off the chamber walls and damage the spacecraft. A set of standalone tests with and EM accelerator (or complete EM spacecraft) may be needed.

We are planning for the mother to have a full set of EGSE and MGSE (UGSE, I&T Test Bed, SAS, BTS, GNC, RF GSE) while the daughters share EGSE and MGSE where appropriate. For example, we assume each daughter will have their own dolly, but only one lift fixture to share between them.

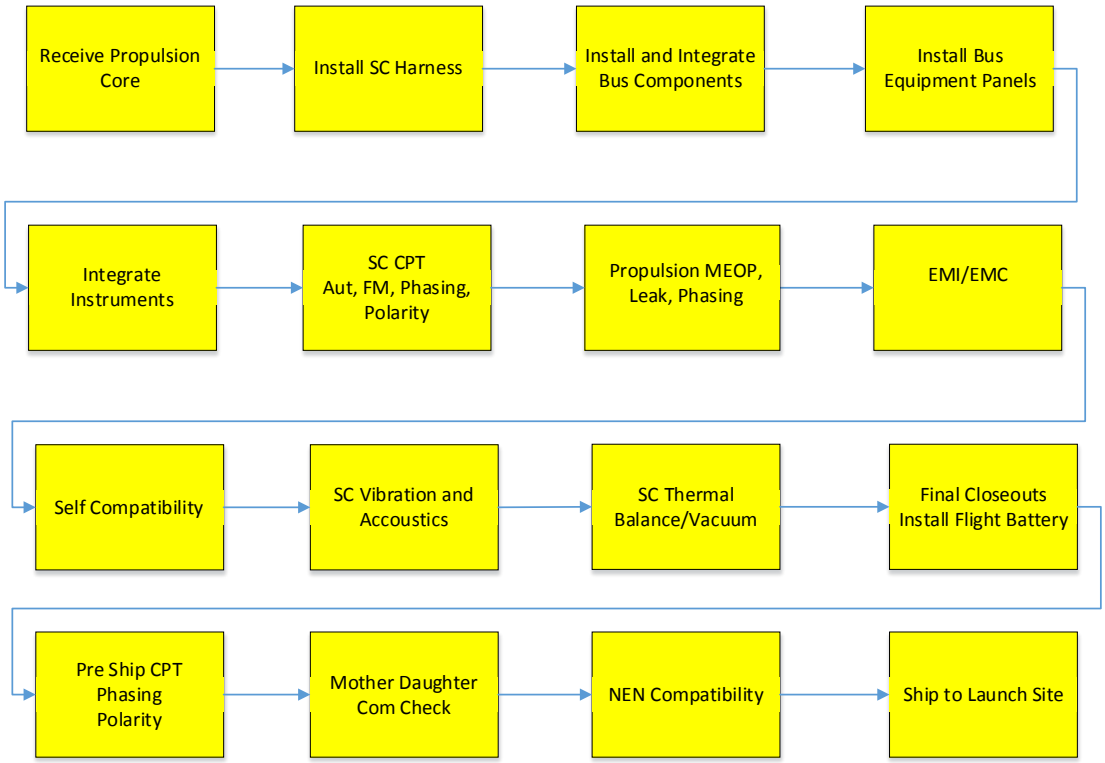

Figure A-15: General flow for mothership I&T.

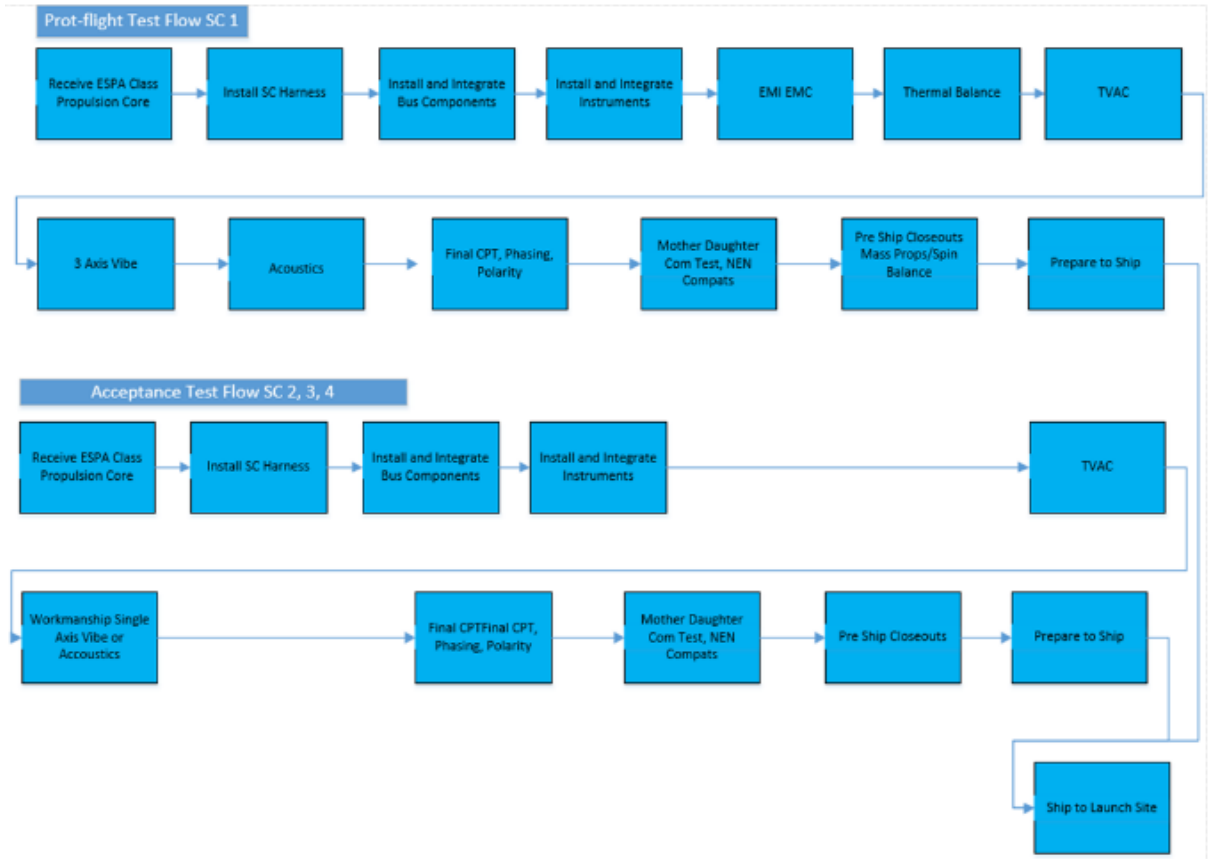

Figure A-16: General flow for daughtership I&T with protoflight testing of the first unit followed by I&T and Acceptance testing of all other units.

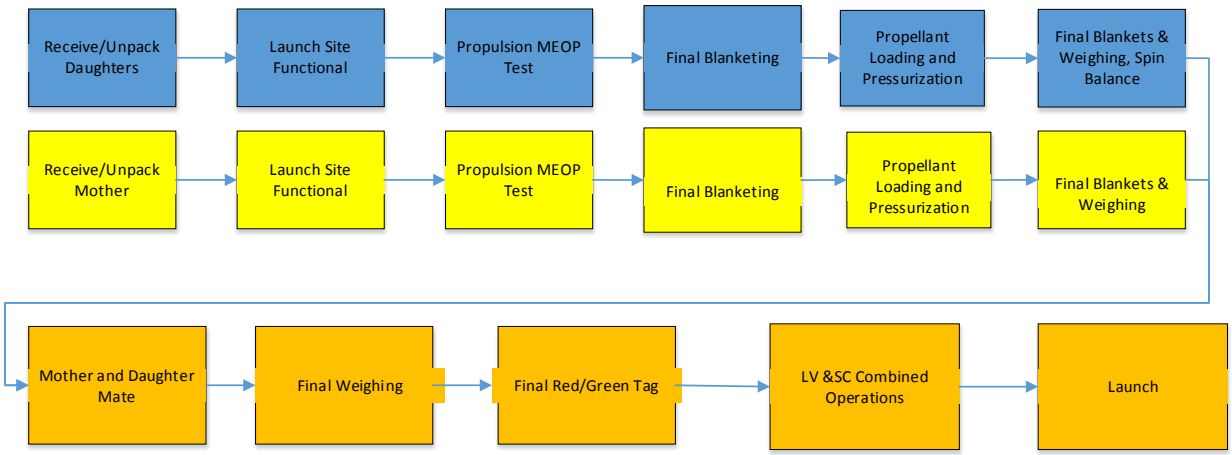

Figure A-17: General flow of launch-site operations.

A.8. Mission Operations Summary Table

Table A-15: Mission operations summary table.

	Mother		Daughter	
Down link Information	**NSN**	**Dedicated**	**NSN**	**Dedicated**
Number of Contacts per Week	3-7	7 (when pulsing)	< 1	Emergency Only
Number of Weeks for Mission Phase, weeks	104			
Downlink Frequency Band, GHz	2.15	2.15	2.15	2.15
Telemetry Data Rate(s), kbps	1,000-5,000	0.2	< 5	0.05
Transmitting Antenna Type(s) and Gain(s), DBi	+10 dBi Patch Array	+10 dBi Patch Array	+4 dBi Garden Wiesel	+4 dBi Garden Wiesel
Transmitter peak power, Watts	20	20	20	20
Downlink Receiving Antenna Gain, DBi	49.5	20	49.5	20
Transmitting Power Amplifier Output, Watts	4	4	4	4
Total Daily Data Volume, (Mb/day)	3,100	Real-Time TLM only	Real-Time TLM only	Real-Time TLM only
Uplink Information				
Number of Uplinks per Day	< 1	1 (when pulsing)	<< 1	Emergency Only
Uplink Frequency Band, GHz	2.07	2.07	2.07	2.07
Telecommand Data Rate, kbps	< 1,000	1	1	0.1
Rx Antenna Type(s) and Gain(s), DBi	+10 dBi Patch Array	+10 dBi Patch Array	+4 dBi Garden Wiesel	+4 dBi Garden Wiesel

B. Acronym List

ACS	Attitude Control Systems
ADCS	Attitude Determiation and Control System
AOS	Advanced Orbiting Systems
ATK	Northrop Grumman
Beam-PIE	Beam Plasma Interaction Experiment
BOL	Beginning of Life
B-SPICE	Beam-Spacecraft Plasma Interaction and Charging Experiment
C3	Characteristic Energy
CAD	Canadian Dollar
CBE	Current Best Estimate
CCSDS	Consultative Committee for Space Data Systems
CER	Cost Estimating Relationship
CFE	Core Flight Executive
CMG	Manufacturer trade name for borosilicate glass
CML	Concept Maturity Level
COTS	Commercial Off The Shelf
DART	Dual Asteroid Redirection Test
DC	Direct Current
DET	Direct Energy Transfer
DSSH	Digital Sun Sensor Head
EDI	Electron Drift Instrument
EEE	Electrical, Electronic, Electro-mechanical
EFW	Electric Field Waves
EMC	Electromagnetic Compatibility
EMI	Electromagnetic Interference
EMIC	Electromagnetic Ion-Cyclotron Waves
EOL	End of Life
EP	Electric Propulsion
ESA	Electrostatic Analyzer
ESD	Electrostatic Discharge
ESPA	Evolved Expendable Launch Vehicle Secondary Payload Adapter
EVMS	Earned Value Management System
FCI	First Circuit Interface
FGM	Fluxgate Magnetometer
FPGA	Field-Programmable Gate Array
FSW	Flight Software
GaN	Gallium Nitride
GC	Guidance and Control
GDS	Ground Data System
GDU	Gun-Detector Unit

GEO	Geosynchronus Orbit
GOES	Geostationary Operational Environmental Satellite
GPS	Global Positioning System
GSE	Ground Support Equipment
GSFC	Goddard Space Flight Center
GTOSat	Geostationary Transfer Orbit Satellite
HAARP	High-frequency Active Auroral Research Program
HEMT	High-Electron Mobility Transistor
HMCS	Heliophysics Mission Concept Study
HVPS	High-Voltage Power Supply
I&T	Integration and Test
IGRF	International Geomagnetic Reference Field
IMAP	Interstellar Mapping and Acceleration Probe
ISR	Incoherent Scatter Radar
ITO	Indium Tin Oxide
JHU/APL	Johns Hopkins University Applied Physics Laboratory
LANL	Los Alamos National Laboratory
LCAS	Low Cost Access to Space
LEO	Low Earth Orbit
LIDAR	Light Detection and Ranging
LINAC	Linear Accelerator
LPW	Langmuir Probe and Waves
LV	Launch Vehicle
LVDS	Low-Voltage Differential Signaling
MA	Mission Assurance
Mag	Magnetometer
MagCon	Magnetospheric Constellation
MAVEN	Mars Atmosphere and Volatile Evolution
MESSENGER	Mercury Surface, Space Environment, Geochemistry and Ranging
MEV	Maximum Expected Value
M-I	Magnetosphere-Ionosphere
MIMU	Miniature Inertial Measurement Unit
MIO	Magnetosphere-Ionosphere Observatory concept with main spacecraft and four daughter
MIOcore	Magnetosphere-Ionosphere Observatory concept with main spacecraft only
MLI	Multi-Layer Insulation
MMS	Magnetospheric Multiscale Mission
MOC	Mission Operations Center
MODTRAN	MODerate resolution atmospheric TRANsmission (computer program)
MSE	Mission Systems Engineer
NASA	National Aeronautics and Space Administration
NEN	Near-Earth Network
NH	New Horizons
NICM	NASA Instrument Cost Model

NPR	NASA Procedural Requirements
OSIRIS-REx	Origins, Spectral Interpretation, Resource Identification, Security-Regolith Explorer
PCS	Plasma Contactor System
PDR	Preliminary Design Review
PFISR	Poker Flat Incoherent Scatter Radar
PFRR	Poker Flat Research Range
PI	Principal Investigator
PM	Project Management
POC	Point of Contact
PS	Project Scientist
PSP	Parker Solar Probe
Re	Earth Radii
RF	Radio Frequency
ROM	Rough Order of Magnitude
RPM	Rotations Per Minute
SAID	Subauroral Ion Drift
SAPS	Subauroral Polarization Stream
SBC	Single-Board Computer
SC	Spacecraft
SE	Systems Engineering
SLAC	Stanford Linear Accelerator Center
SMA	Semi-Major Axis
SOC	Science Operations Center
SOS	Save Our Souls
SRI	SRI, formerly Stanford Research Institute
SSA	Sun Sensor Assembly
SSE	Sun Sensor Electronics
SSI	Space Sciences Institute
SSPA	Solid State Power Amplifier
SSR	Solid State Recorder
STEREO	Solar Terrestrial Relations Observatory
STEVE	Strong Thermal Emission Velocity Enhancement
STP	Space Test Program
SuperDARN	Super Dual Auroral Radar Network
TAC	Thruster/Actuator Card
TBAL	Thermal Balance
TBD	To Be Determined
TBR	To Be Revised
THEMIS	Time History of Events and Macroscale Interactions during Substorms
TID	Total Ionizing Dose
TNID	Total Non-Ionizing Dose
TREx	Transition Region Explorer (optical-imager network)
TRL	Technology Readiness Level

TT&C	Telemetry, Tracking, and Command
TVAC	Thermal Vacuum
UART	Universal Asynchronous Receiver/Transmitter
ULF	Ultra-Low Frequency
UNH	University of New Hampshire
US	United States
USD	United States Dollar
UT	Universal Time
VAP	Van Allen Probes
VLF	Very-Low Frequency
WBS	Work Breakdown Structure

C. References

Anderson, B. J., Acuna, M. H., Lohr, D. A., Scheifele, J., Raval, A., Korth, H., Slavin, J. A. (2007). The magnetometer instrument on MESSENGER. Space Sci. Rev. 131:417.

Bogdankevich, L. S., and Rukhadze, A "Stability Of Relativistic Electron Beams In A Plasma And The Problem Of Critical Currents." Soviet Physics Uspekhi 14, 163–79 (1971) https://doi.org/10.1070/PU1971v014n02ABEH004456.

Borovsky, J. E. (1993). Auroral arc thicknesses as predicted by various theories. J. Geophys. Res. 98:6101.

Borovsky, J. E., (2002). The Magnetosphere-Ionosphere Observatory (MIO). Los Alamos National Laboratory https://www.lanl.gov/csse/MIOwriteup.pdf

Borovsky, J. E., Valdivia, J. A. (2018). The Earth's magnetosphere: A systems science overview and assessment. Surveys Geophys. 39:817.

Borovsky, J. E., Birn, J., Echim, M. M., Fujita, S., Lysak, R. L., Knudsen, D. J., Marghitu, O., Otto, A., Watanabe, T.-H., Tanaka, T. (2020d). Quiescent discrete auroral arcs: A review of magnetospheric generator mechanisms, Space Sci. Rev. 216:1.

Borovsky, J. E., Delzanno, G. L., Dors, E. E., Thomsen, M. F., Sanchez, E. R., Henderson, M. G., Marshall, R. A., Gilchrist, B. E., Miars, G., Carlsten, B. E., Storms, S. A., Holloway, M. A., Nguyen, D. (2020a). Solving the Auroral-Arc-Generator Question by Using an Electron Beam to Unambiguously Connect Critical Magnetospheric Measurements to Auroral Images,. J. Atmos. Solar-Terr. Phys. 206:105310, doi.org/10.1016/j.jastp.2020.105310.

Borovsky, J. E., Delzanno, G. L., Henderson, M. G. (2020b). A mission concept to determine the magnetospheric causes of aurora. Front. Astron. Space Sci. 7:595292.

Borovsky, J. E., Delzanno, G. L., Yakymenkno, K. N. (2022a). Pitch-angle diffusion in the Earth's magnetosphere organized by the Mozer-transformed coordinate system. Front. Astron. Space Sci. 9:810792.

Borovsky, J. E., Yakymenko, K. N., Delzanno, G. L. (2022b). Modification of the loss cone for energetic particles in the Earth's inner magnetosphere. J. Geophys. Res. 2021JA030106, in press.

Bowers, K J, B J Albright, L Yin, B Bergen, and T J T Kwan. "Ultrahigh Performance Three-Dimensional Electromagnetic Relativistic Kinetic Plasma Simulation." Physics of Plasmas 15, 055703 (2008) https://doi.org/10.1063/1.2840133.

Bryant, D. E., Courtier, G. M., Skovli, G., Lindalen, H. R., Aarsnes, K., Maseide, K. (1970). Electron density and electron flux in a glow aurora. J. Atmos Terr. Phys. 32:1695.

Chernick, M., D'Amico, S. "Closed-Form Optimal Impulsive Control of Spacecraft Formations Using Reachable Set Theory," Journal of Guidance, Control, and Dynamics, Vol. 44, No. 1, pp. 25-44 (2021).

Comfort, R. H., Moore, T. E., Craven, P. D., Pollock, C. J., Mozer, F. S., Williamson, W. S. (1998). Spacecraft potential control by the Plasma Source Instrument on the Polar satellite. J. Spacecraft Rockets 35:845.

Davis, T. N., Hess, W. N., Trichel, M. C., Wescott, E. M., Hallinan, T. J., Stenbaek-Nielsen, H. C., Maier, E. J. R. (1980). Artificial aurora conjugate to a rocket-borne electron accelerator. J. Geophys. Res. 85:1722.

Delzanno, G. L., Borovsky, J. E., Thomsen, M. F., Moulton, J. D. (2015a). Beam experiments in the magnetosphere with plasma contactors: the electron collection and ion emission routes, J Geophys. Res. 120:3588.

Delzanno, G. L., Borovsky, J. E., Thomsen, M. F., Moulton, J. D., MacDonald, E. A. (2015b). Beam experiments in the magnetosphere: how do we get the charge off the spacecraft? J Geophys. Res. 120:3647.

Delzanno, G. L., Borovsky, J. E., Thomsen, M. F., Gilchrist, B. E., Sanchez, E. (2016). Can an electron gun solve the outstanding problem of magnetosphere-ionosphere connectivity? J Geophys. Res. 121:6769.

Frieman, E. A., M. L. Goldberger, K. M. Watson, S. Weinberg, and M. N. Rosenbluth. "Two-Stream Instability in Finite Beams." Physics of Fluids 5, 196 (1962). https://doi.org/10.1063/1.1706596.

Galvez, M., Borovsky, J. E. (1988). The electrostatic two-stream instability driven by slab-shaped and cylindrical beams injected into plasmas. Phys. Fluids 31:857.

Gilchrist, B. E., Banks, P. M., Neubert, T., Williamson, P. R., Myers, N. B., Raitt, W. J. Sasaki, S., 1990. Electron collection enhancement arising from neutral gas jets on a charged vehicle in the ionosphere. J. Geophys. Res. 95, 2469.

Guffanti, T., D'Amico, S. "Multi-Agent Passively Safe Optimal Control using Integration Constants as State Variables," AIAA Scitech 2021 Forum, Virtual Event, January 11-15 & 19-21 (2021).

Guffanti, T., D'Amico, S, Lavagna, M.. "Long-Term Analytical Propagation of Satellite Relative Motion in Perturbed Orbits," 27th AAS/ AIAA Space Flight Mechanics Meeting, San Antonia, Texas, February 5-9, 2017.

Hallinan, T. J., Winkler, J., Malcolm, P., Stanbaek-Nielsen, H. C., Baldridge, J. (1990). Conjugate echoes of artificially injected electron beams detected optically by means of new image processing. J. Geophys. Res. 95:6519.

Hedin, A. E. (1987). MSIS-86 thermospheric model, J. Geophys. Res. 92:4649.

Horne, R. B., Thorne, R. M., Meredith, N. P., Anderson, R. R. (2003). Diffuse auroral electron scattering by electron cyclotron harmonic and whistler mode waves during an isolated substorm. J. Geophys. Res. 108:1290.

Horne, R. B., Kersten, T., Glauert, S. A., Meredith, N. P., Boscher, D., Sicard-Piet, A., Thorne, R. M., Li, W. (2013). A new diffusion matrix for whistler mode chorus waves, J. Geophys. Res. 118:6302.

Il'in, V. D., Kuznetsov, S. N., Yushkov, B. Y., Il'in, I. V. (1992). Quasiadiabatic model of charged-particle motion in a dipole magnetic confinement system under conditions of dynamic chaos. JETP Lett. 55, 645-649.

Il'ina, a. N., Il'in, V. D., Kuznetsov, S. N., Ysushkov, B. Y., Amirkhanov, I. V., Il'in, I. V. (1993). Model of nonadiablatic charged particle mostion in the field of a magnetic dipols. JETP 77, 246-252.

ITT (International Telephone and Telegraph Corporation) (1977). Reference Data for Radio Engineers. Sect. 28, Fig. 32, Howard Sams and Co., Indianapolis, Ind.

Jones, A. W. (1974). Aurora. D. Reidel Publishing, Dordrecht.

Kang, S.-B., Min. K.-W., Fok, M.-C., Hwang, J., Choi, C.-R. (2015). Estimation of pitch angle diffusion rates and precipitation time scales of electrons due to EMIC waves n a realistic field model. J. Geophys. Res. 120:8529-8546.

Katz, I., Barfield, J. N., Burch, J. L., Marshall, J. A., Gibson, W. C., Neubert, T., 1994. Interactions between the space experiments with particle plasma contactor and the ionosphere. J. Spacecraft Rockets 31, 1079.

Kepko, L. (2018). Magnetospheric Constellation: Leveraging Space 2.0 for Big Science. IGARSS 2018 - 2018 IEEE International Geoscience and Remote Sensing Symposium, pp. 285-288, doi: 10.1109/IGARSS.2018.8519475.

Koenig, A. W., Guffanti, T, D'Amico, S, "New state Transition Matrices for Spacecraft Relative Motion in Perturbed Orbits," Journal of Guidance, Control, and Dynamics, Vol. 40, No. 7, pp. 1749-1768 (2017).

Lei, M., Xie, L., Li, J., Pu, Z., Fu, S., Ni. B., Hua, M., Chen, L., Li, W. (2017). The radiation belt electron scattering by magnetosonic wave: Dependence on key parameters. J. Geophys. Res. 122:12338-12352.

Lewellen, J. W., Buechler, C. B., Carlsten, B. F., Dale, G. E., Holloway, M. A., Patrick, D., Storms, S. A., Nguyen, D. C. (2019). Space borne electron accelerator design. Front. Astron. Space Sci. 6:35.

Lippe, C., D'Amico, S. "Safe, Delta-v-Efficient Spacecraft Swarm Reconfiguration Using Lyapunov Stability and Artificial Potentials," Journal of Guidance, Control, and Dynamics, Vol. 45, No. 2, pp. 213-231 (2022).

Lucco Castello, F., Delzanno, G. L., Borovsky, J. E., Miars, G., Leon, O., Gilchrist, B. E. (2018). Spacecraft-charging mitigation of a high-power electron beam emitted by a magnetospheric spacecraft: Simple theoretical model for the transient of the spacecraft potential. J. Geophys. Res. 123:6424.

Ma, Q., Li, W, Thorne, R. M., Kletzing, C. A., Kurth, W. S., Hospodarsky, G. B., Reeves, G. D., Henderson, M. G., Spence, H. E., Baker, D. N., Blake, J. B., Fennell, J. F., Claudepierre, S. G., Angelopoulos, V. (2015). Modeling inward diffusion and slow decay of energetic electrons in the Earth's outer radiation belt. Geophys. Res. Lett. 42:987-995.

Marshall, R. A., Nicolls, M., Sanchez, E., Lehtinen, N. G., Neilson J. (2014). Diagnostics of an artificial relativistic electron beam interacting with the atmosphere. J. Geophys. Res. 119:8560.

Marshall, R. A, Xu, W., Kero, A, Kabirzadeh, R, Sanchez, E. (2019). Atmospheric effects of a relativistic electron beam injected from above: chemistry, electrodynamics, and radio scattering. Front. Astron. Space Sci. 6:6.

McFadden, J. P., Carlson, C. W., Larson, D., Ludlam, M., Abiad, R., Elliott, B., Turin, P., Marckwordt, M., Angelopoulos, V. (2008). The THEMIS ESA plasma instrument and in-flight calibration. Space Sci. Rev. 141:277.

McNutt, R. L., Rieder, R. J., Keneshea, T. J., LePage, A. J., Rappaport, S. A., Pualsen, D. E. (1995). Energy deposition in the upper atmosphere in the EXCEDE III experiment. Adv. Space Res. 15(12):13.

Melrose D B, "Instabilities in Space and Laboratory Plasmas", New York: Cambridge University Press, 1986.

Meredith, N. P., Horne, R. B., Kersten, T., Fraser, B. J., Grew, R. S., (2014). Global morphology and spectral properties of EMIC waves derived from CRRES observations. J. Geophys. Res. 119:5328-5342.

Miars, G. (2020). Spacecraft Charge Neutralization During Active Electron Emission: Doctoral dissertation, University of Michigan.

Miars, G., Leon, O., Gilchrist, B. E., Delzanno, G. L., Borovsky, J. E., 2016. Electrically Isolated System Response to Rapid Charging Events Using Hollow Cathode Neutralization, 14th Spacecraft Charging Technology Conference, Noordwijk, Netherlands, April 4-8.

Miars, G, Leon, O, Gilchrist, B. E, Delzanno, G. L, Lucco Castello, F, Borovsky, J. E., 2017. Ion Emission Experiments Enabling Electron Beam Emission in Tenuous Plasmas, Active Experiments in Space, Santa Fe, NM, September 11-15.

Miars, G., Leon, O., Gilchrist, B. E., Delzanno, G. L., Lucco Castello, F., 2018a. Parametric Experiments in Mitigating Spacecraft Charging via Plasma Contactor, American Geophysical Union Fall Meeting, Washington D.C., USA, December 10-14.

Miars, G., Delzanno, G. L., Lucco Castello, F., Leon, O., Gilchrist, B. E., 2018b. Enabling Electron Beam Use in Tenuous Space Plasmas using Plasma Contactors: the Ion Emission Model, 15th Spacecraft Charging Technology Conference, Kobe, Japan, June 25-29..

Miars, G., Gilchrist, B. E., Delzanno, G. L., Leon, O. (2019). B-SPICE: The Beam-Spacecraft Plasma Interaction and Charging Experiment. 2019 Fall AGU abstract SA33C-3163M.

Miars G, Delzanno GL, Gilchrist BE, Leon O, Lucco Castello F. (2020a). Ion Emission from a Positively Biased Hollow Cathode Plasma, IEEE Trans. Plasma Sci. 48:2693.

Miars, G., Delzanno, G. L., Gilchrist, B. E., Leon, O. (2020b). New electron beam experiments in space and active spacecraft potential control. 2020 Fall AGU abstract SM016-08.

Min, K., Lee, J., Keika, K., Li, W. (2012). Global distribution of EMIC waves derived from THEMIS observations. J. Geophys. Res. 117:A05219.

Mott-Smith, H., Langmuir I., 1926. The theory of collectors in gaseous discharges, Phys. Rev. 28, 727.

Mourenas, D., Artemyev, A. V., Agapitov, O. V., Krasnoselskikh, V. (2013). analytical estimates of electron quasi-linear diffusion by fast magnetosonic waves. J. Geophys. Res. 118:1-17.

Mozer, F. S. (1966). Proton trajectories in the radiation belt. J. Geophys. Res. 71:2701.

NASA (2014). Science Plan 2014. pg. 27. https://science.nasa.gov/science-pink/s3fs-public/atoms/files/2014_Science_Plan_PDF_Update_508_TAGGED_1.pdf

National Research Council, 2013. Magnetosphere-to-ionosphere field-line tracing technology, in Solar and Space Physics: A Science for a Technological Society, pp. 333-334, Library of Congress 2013940083, National Academies Press, Washington, D. C.

Ni, B., Thorne, R. M., Horne, R. B., Meredith, N. P., Shprits, Y. Y., Chen, L., Li, W. (2011). Resonant scattering of plasma sheet electrons leading to diffuse auroral precipitation: 1. Evaluation for electrostatic electron cyclotron harmonic waves. J. Geophys. Res. 116:A04218.

Olsen, R. C., 1985. Experiments in charge control at geosynchronous orbit—ATS-5 and ATS-6. J. Spacecraft Rockets 22, 254.

Omholt ,A. (1971). The Optical Aurora. Sect. 2.2, Springer-Verlag, New York.

O'Neil, R. R., Shepherd, O., Reidy, W. P., Carpenter, J. W., Davis, T. N., Newell, D., Ulwick, J. C., Stair, A. T. (1978). Excede 2 test, an artificial auroral experiment: Ground-based optical measurements. J. Geophys. Res. 83:3281.

Penndorf, R. (1957). Tables of the refractive index for standard air and the Rayleigh scattering coefficient for the spectral region between 0.2 and 20.0 and their application to atmospheric optics. J. Optical Soc. Amer. 47:176.

Porazik, P., Johnson, J. R., Kaganovich, I., Sanchez, E. (2014). Modification of the loss cone for energetic particles. Geophys. Res. Lett. 41:8107.

Powis, A. T., Porazik, P., Greklek-Mckeon, M., Amin, K., Shaw, D., Kaganovich, I. D., Johnson, J., Sanchez, E. R. (2019). Evolution of a relativistic electron beam for tracing magnetospheric field lines. Front. Astron. Space Phys. 6:69.

Prech, L., Nemecek, Z., Safrankova, J., Simunek, J., Truhlik, V., Shutte, N. M. (1995). Response of the electron energy distribution to an artificially emitted electron beam: APEX experiment. Adv. Space Res. 15(12):33.

Prech, L., Nemecek, Z., Safrankova, J., Omar, A. (2002). Actively produced high-energy electron bursts within the magnetosphere: the APEX project. Ann. Geophys. 20:1529.

Prech, L., Ruzhin, Y. Y., Dokukin, V. S., Nemecek, Z., Safrankova, J. (2018). Overview of APEX Project results. Front. Astron. Space Sci. 5:46.

Qin, M., Hudson, M., Millan, R., Woodger, L., Shekhar, S. (2018). Statistical investigation of the efficiency of EMIC waves in precipitating relativistic electrons. Journal of Geophysical Research: Space Physics, 123:6223-6230. https://doi.org/10.1029/2018JA025419.

Rappaport, S. A., Rieder, R. J., Reidy, W. P., McNutt, R. L., Atkinson, J. J., Paulsen, D. E., 1993. Remote x-ray measurements of the electron-beam from the EXCEDE-III experiment. J. Geophys. Res. 98:19093.

Reeves, G. D., Delzanno, G. L., Fernandes, P. A., Yakymenko, K., Carlsten, B. E., Lewellen, J. W., Holloway, M. A., Nguyen, D. C., Pfaff, R. F., Farrell, W. M., Rowland, D. E., Samara, M., Sanchez, E. R., Spanswick, E., Donovan, E. F., Roytershteyn, V. (2020). The Beam Plasma Interactions Experiment: An active experiment using pulsed electron beams. Front. Astron. Space Sci. 7:23.

Roederer, J. G., Zhang, H. (2014). Dynamics of Magnetically Trapped Particles. Springer-Verlag, Berlin.

Ross, J. P. J., Glauert, S. A., Horne, R. B., Watt, C. E., Meredith, N. P., Woodfield, E. E. (2020). A new approach to constructing models of electron diffusion by EMIC waves in the radiation belts. Geophys. Res. Lett. 47:e2020GL088976.

Sanchez, E. R., Powis, A. T., Kagonovich, I. D., Marshall, R., Porazik, P., Johnson, J., Grekiek-Mckeon, M., Amin, K. S., Shaw, D. Nicolls, M. (2019). Relativistic particle beams as a resource to solve outstanding problems in space physics. Front. Astron. Space Sci. 6:71.

Shprits, Y. Y., Runov, A., Ni, B. (2013). Gyro-resonant scattering of radiation belt electrons during the solar minimum by fast magnetosonic waves. J. Geophys. Res. 118:648-652.

Spanswick, E., Donovan, E., Liang, J., Weatherwax, A. T., Skone, S., Hampton, D. L., Gillies, M., Yang, B., Chaddock, D., Vollmerhaus, L., Kujawski, J. T. (2018). First-Light Observations from the Transition Region Explorer (TREx) Ground-Based Network. American Geophysical Union, Fall Meeting, abstract SM23B-04,2018AGUFMSM23B..04S

Torbert, R. B., Vaith, H., Granoff, M., Widholm, M., Gaidos, J. A., Briggs, B. H., Dors, I. G., Chutter M. W., Macri, J., Argall, M., Bodet, D., Needell, J., Steller, M. B., Baumjohann, W., Nakamura, R., Plaschke, F., Ottacher, H., Hasiba, J., Hofmann, K., Kletzing, C. A., Bounds, SR, Dvorsky, RT, Sigsbee, K, Kooi, V. (2016). The electron drift instrument for MMS. Space Sci. Rev. 199:283.

Torkar, K., Riedler, W., Escoubet, C. P., Fehringer, M., Schmidt, R., Grard, R. J. L., et al. (2001). Active spacecraft potential control for Cluster -- Implementation and first results. Ann. Geophys. 19:1289.

Torkar, K., Nakamura, R., Tajmar, M., Scharlemann, C., Jeszenszky, H., Laky, G., Fremuth, G., Escoubet, C. P., Svenes, K. (2016). Active spacecraft potential control investigation. Space Sci. Rev. 199:515.

Tsyganenko, N. A. (1995). Modeling the Earth's magnospheric magnetic field confined within a realistic magnetopause. J. Geophys. Res. 100:5599.

Tsyganenko, N. A., Stern, D. P. (1996). Modeling the global magnetic field of large-scale Birkeland current systems. J. Geophys. Res. 101:27187.

Usanova, M. E., Mann, I. R., Bortnik, J., Shao, L., Angelopoulos, V. (2012). THEMIS observations of electromagnetic ion cyclotron wave occurrence: Depedence on AE, SYMH, and solar wind dynamic pressure. J. Geophys. Res. 117:A10218.

Vette, J. I. (1991). The AE-8 trapped electron model environment. NSSDC/WDC-A-R&S 91-24, https://ccmc.gsfc.nasa.gov/publications/users_publication_files/Vette_1991_Ae8Ap8-ref1.pdf.

Whitley, S., M. Hahn, and N. Powers. "The Incremental Cost of One or More Copies – Quantifying Efficiencies from Building Spacecraft and Instrument Constellations." AIAA/Utah State University Small Satellite Conference, 2013.

Winckler, J. R., Arnoldy, R. L., Hendrickson, R. A. (1975). Echo-2: Study of electron beams injected into the high latitude ionosphere from a large sounding rocket. J. Geophys. Res. 80:2083.

Yang, C., Zhang, L., He., Y., Liu, S., Zhou, Q. (2014). Radiation belt electron acceleration induced by gyroresonant interaction with magnetosonic waves. Astrophys. Space Sci. 353:389-394.
Zilavy, P., Prech, L., Nemecek, Z., Safrankova, J. (2003). Spacecraft potential during an active experiment: a comparison of experimental results with a simple model. Ann. Geophys. 21:915.